DEVELOPMENT OF EFFICIENT ENERGY STORAGE AND POWER MANAGEMENT FOR AUTONOMOUS AIRCRAFT STRUCTURAL HEALTH MONITORING SYSTEMS

PhD Thesis

November 2017

Karthik Thangaraj

School of Engineering

Cardiff University

Cardiff

UK

Prifysgol Caredydd **Summary of thesis** **Cardiff University**

Candidate's Surname: Thangaraj

Candidate's First name: Karthik

Candidate for degree of: PhD

Institute at which study pursued: Cardiff University

The full title of thesis: Development of Efficient Energy Storage and Power Management for Autonomous Aircraft Structural Health Monitoring Systems.

Summary:

This thesis investigates the development of an efficient energy storage and power management system for aircraft structural health monitoring (ASHM) applications, powered by specific thermoelectric energy harvesting. For efficient power management, commercially available DC-DC converters are critically analysed.

A novel switched-energy storage system is proposed that can be used to extend the run-time of a typical wireless ASHM sensor. Experimental characterisation of a range of different batteries and supercapacitors has been performed, followed by a critical performance analysis of a simple parallel combination of a battery and supercapacitor for run-time extension of a wireless sensor node (WSN). The problems associated with such a simple parallel hybrid system are identified, and a new switched architecture is presented that overcomes these disadvantages.

Acknowledgments

I would like to take this opportunity to express an enormous debt of gratitude to my academic supervisors Prof. Carol Featherston, Dr Jonathan Lees and Dr Rhys Pullin for their guidance and immense support and patience through my work. I would also like to thank Dr Mark Eaton and Dr Matthew Pearson for their advice and help. My thanks also to the technical staff in the School of Engineering especially Mr Denley Slade and Mr Richard Rogers.

I am also grateful to Prof. Thomas Becker of Airbus, my industrial supervisor for his technical feedback and advice. Also, the Airbus TCC'4 technical team in Munich.

I would also like to thank Prof. Manuel Gasulla Forner, Universitat Politècnica de Catalunya for his technical advice.

Finally, thanks to my family members and friends.

Nomenclature

C_{lp}	[J.kg^{-1}. K^{-1}]	Heat capacity of PCM in liquid phase
C_{sp}	[J.kg^{-1}. K^{-1}]	Heat capacity of PCM in solid phase
D	[-]	Duty cycle
$D_{MPP,\ boost}$	[-]	Duty cycle at maximum power point for a boost converter
$D_{MPP,\ buck}$	[-]	Duty cycle at maximum power point for a buck converter
$D_{MPP,\ buck\text{-}}$	[-]	Duty cycle at maximum power point for a buck-boost
$D_{MPP,}$	[-]	Duty cycle at maximum power point for a flyback
f_s	[Hz]	Switching
I_{in}	[A] or [mA]	Input current
I_{out}	[A] or [mA]	Output current
k	[-]	Constant
m	[kg]	Mass
M_I	[-]	Current transfer function
M_U	[-]	Voltage transfer function
$M_{U,\ boost}$	[-]	Voltage transfer function of a boost converter
$M_{U,\ buck}$	[-]	Voltage transfer function of a buck converter
$M_{U,\ buck\text{-}boost}$	[-]	Voltage transfer function of a buck-boost converter
$M_{U,\ flyback}$	[-]	Voltage transfer function of a flyback converter
N	[-]	Turn ratio
t_{on}	[s]	On-time
t_{off}	[s]	Off-time
T	[s]	Switching period
T_h	[°C] or [K]	Hot-side temperature
T_c	[°C] or [K]	Cold-side temperature
T_{JECU}	[°C] or [K]	Temperature of JECU
T_{pch}	[°C] or [K]	Phase-change temperature
ΔT	[°C] or [K]	Temperature difference along the module
ΔT_{peak}	[°C] or [K]	Peak temperature difference
P_{el}	[mW]	Electric power
$P_{el,\ peak}$	[mW]	Peak electric power
$P_{el,\ avg}$	[mW]	Average electric power
P_{MPP}	[mW]	Output electric power on maximum power point
Q_a	[J]	Available heat
Q_c	[W]	Heat flow through cold side of thermoelectric module
Q_h	[W]	Heat flow through hot side of thermoelectric module
Q_{Ph}	[W]	Peltier cooling on a hot side of TEM
Q_{Pc}	[W]	Peltier cooling on a cold side of TEM

Q_J	[W]	Joule heating
Rheatsink	[$W.K^{-1}$]	Thermal resistance of heat sink
R_{out}	[Ω]	Output resistance
R_{load}	[Ω]	Load resistance
R_{in}	[Ω]	input resistance
R_{TEM}	[Ω]	Thermoelectric module internal resistance
RtTEM	[$W.K^{-1}$]	Thermal resistance of TEM
U_{in}	[V] or [mV]	Input voltage
U_{load}	[V] or [mV]	Voltage on load
U_{oc}	[V] or [mV]	Open-circuit voltage
U_{out}	[V] or [mV]	Output voltage
η	[-] or [%]	Efficiency
$\alpha_{heatsink}$	[$W.m^{-2}.K^{-1}$]	Convective heat transfer coefficient to ambient air net
$\alpha\sum$	[$V.K^{-1}$]	Seebeck coefficient
AC	[-]	Alternating current
APU	[-]	Auxiliary power unit
ASN	[-]	Autonomous sensor node
ASHM	[-]	Aircraft structural health monitoring system
AASHM	[-]	Autonomous Aircraft structural health monitoring system
CCM	[-]	Continuous conduction mode
COTS	[-]	Commercial-of-the-shelf
DC	[-]	Direct current
DCM	[-]	Discontinuous conduction mode
ESR	[-]	Equivalent series resistance
HUMS	[-]	Health and usage monitoring system
IC	[-]	Integrated circuit
LDO	[-]	Low dropout regulator

MEMS	[-]	Micro electro-mechanical system
MPPT	[-]	Maximum power point tracking
NDT	[-]	Non-destructive testing
P&O	[-]	Perturb and observe
PCM	[-]	Phase change material
PFM	[-]	Pulse-frequency modulation
PWM	[-]	Pulse-width modulation
RF	[-]	Radio frequency
RFID	[-]	Radio frequency identification
SHM	[-]	Structure health monitoring
SMPS	[-]	Switching-mode power supply
TEG	[-]	Thermoelectric generator
TEM	[-]	Thermoelectric module
ULP	[-]	Ultra-low power
WSN	[-]	Wireless sensor node

TABLE OF CONTENTS

Table of Figures

List of Tables

ABSTRACT

In aircraft structural health monitoring (ASHM) techniques, the sensors deployed are typically connected using coaxial wires, contributing to the complexity and adding to the weight of the structure. The Airbus A380, for instance, has over 300 miles of cables consisting of approximately 98,000 individual wires and 40,000 connectors. However, the introduction of autonomous wireless sensor nodes (WSN) offers the opportunity to reduce installation and maintenance costs (Galea and Baker 2001) by reducing the level of wiring necessary.

For WSNs to be truly autonomous, they must derive their power from locally harvested energy, which must be collected and converted into usable electric power. However, as the energy availability and power demand are not constant over time, effective energy management and storage becomes a core system function. For an ASHM system, the energy storage system should have good cycle-life, less leakage current, operational temperature range of -40^{o}C to +40^{o}C and without adding significantly more weight to the ASHM system. In this thesis, thin-film solid state and Li-ion batteries, along with supercapacitors have been considered as energy storage options. The thin-film solid-state batteries initially considered were unfortunately discontinued during the period of this research, so it was necessary to use a standard Li-ion coin cell (LIR 2450) as a replacement.

The disadvantages in powering WSNs using batteries and supercapacitor have been identified with experimental results. Both Li-ion batteries suffered from voltage drops under pulsed-load conditions compared with supercapacitors. Supercapacitors have their own disadvantages, however, such as high leakage current and low energy density compared with Li-ion batteries. It is shown how 44 J in a hybrid energy storage unit can extend WSN run time from 11 hours to 21 hours in comparison with the single supercapacitor with 41 J of energy. The combined disadvantages of the high leakage current associated with a supercapacitor and the lower cycle-life of the battery become a limiting factor in such a simple hybrid energy storage system

In this Thesis, a novel switched-energy storage architecture is proposed, where the charge and discharge behaviour of each storage element is individually monitored. In this system, most of the harvested energy will be stored in the thin-film battery with low-leakage current 0.006 mA and will be used to charge the supercapacitor only when needed. The supercapacitor services the high dynamic current demand of the WSN and high cycle-life of the supercapacitor is exploited. Compared with an existing supercapacitor based storage unit of Airbus ASHM system, approximately 53 % of weight per sensor node can be saved by adopting to the switched-energy storage unit.

1 Introduction

This thesis presents the technologies and approaches used in the development of an efficient energy storage and power management system for an autonomous aircraft structural health monitoring (AASHM) application. The work focuses on a broad range of research studies that are essential in the realisation of such a system. These include characterisation and experimental analysis of potential storage devices including batteries, supercapacitors, a simple parallel combination of supercapacitor and battery, as well as a more complex switched combination of battery and supercapacitor with an associated switched- algorithm. It is shown how the proposed novel energy storage system can extend the run-time of a WSN used for ASHM.

1.1 AASHM

Advanced composite structures are becoming increasingly popular in aircraft applications. The advantages of high strength, stiffness and corrosion resistance make them ideal for aircraft structures (Staszewski, Mahzan et al. 2009). These composite structures can be manufactured in large complex shapes for aircraft, which reduces cost but the damage caused by aircraft during operational service may lead to severe degradation of structural integrity. As a result, such structures are typically over-engineered to cater for such damage and are subject to costly inspection and maintenance regimes.

Significant research has been carried out in a range of SHM technologies in recent years. However, the application of SHM onboard an aircraft is still a challenge, with specific requirements on the SHM system design and operation. The challenges include installation of sensors, power cables, robust damage detection and decision-making capabilities. Further, minimization of weight and dimensions, system reliability

anddurability also need to be addressed. Due to these challenging requirements, SHM has yet to be widely implemented in the aerospace industry.

Wireless sensor nodes (WSNs) represent one potential technology that can help advance the field of structural engineering's ability to realise SHM economically (Flynn and Todd 2010). Interest in WSN was initially motivated by their low-cost attributes. AASHM has an advantage of low-cost installation as it does not require power and signalling cables. These low costs promise wireless monitoring systems defined by greater nodal densities as compared to traditional tethered monitoring systems. Thousands of wireless sensors can be installed in an aircraft structure, and they can be used to monitor the behaviour of critical structural components, thereby implementing local-based damage detection.

For full advantage of these sensor systems to be realised. However, they need to be truly wireless, and hence self-powered by locally harvested energy. When energy harvesting is used in aerospace applications, thermoelectric devices are the preferred option (Samson, Kluge et al. 2010) due to the relatively high levels of energy available in comparison to other types of harvesting, such as vibration. Energy can be harvested in various parts of the aircraft from the temperature gradients between the internal parts of the aircraft, such as cabin, engine compartment, fuel tanks, and the fuselage. The 'raw' energy available from a thermoelectric energy generator (TEG) depends completely upon the degree and polarity of the temperature gradients available. In order to supply the required power throughout the aircraft's flight cycle, the power management system employed needs to be able to condition and manage the harvested energy efficiently.

Energy storage is a critical element in aerospace applications as energy harvesting is not possible throughout the entire flight cycle. Whereas batteries are usually the preferred choice for energy storage element, it is also possible to use supercapacitors. Although supercapacitors have a lower energy density and higher leakage than batteries and therefore cannot provide sufficient long-term energy, they have the advantage of

higherpower density and can provide for example the high instantaneous current required to initialize or *wake* the WSN. For an ASHM system, the energy storage elements used should have longer cycle-life and less leakage current. Another significant consideration is operational temperature; for example, depending upon the aircraft location and altitude, this can be expected to vary typically over a range of -40^{o}C to +40^{o}C. In this thesis, the operational behaviour of both battery and supercapacitor energy storage elements are characterised by charging and discharging over an 80-minute cycle, in the temperature range of -40^{o}C to +40^{o}C. It is recognised that for short-haul flights, typically 80 minutes in duration, the temperature variation will be relatively dynamic, whereas, for long-haul flights, assumed here to be a maximum of 13 hours and 40 minutes, significant temperature differences may only be apparent over an hour or so.

Solid-state thin-film batteries are preferred for ASHM as they have longer cycle-life, less leakage current and do not suffer from dendrites as is the case for a standard Li-ion battery technology. The thin-film solid-state batteries initially considered were unfortunately discontinued during the period of this research, so it was necessary to use a standard Li-ion coin cell (LIR 2450) as a replacement to demonstrate the novel aspects of switched-energy storage. It is important to stress that the LIR 2450 battery is not a preferred choice for real-time ASHM application due to its low cycle-life, with an operational temperature range -20^{o}C to +45^{o}C and according to the industrial sponsor who have funding this work may well be affected by the build-up of problematic dendrites.

Combining both battery and supercapacitor elements into a hybrid energy storage solution can provide both energy and power density to the wireless sensor node simultaneously and is, therefore, an excellent potential solution for a low power WSN (Thangaraj, Elefsiniots et al. 2013, Thangaraj, Elefsiniots et al. 2014). There are disadvantages, however: Firstly, the relatively high leakage current associated with the supercapacitor provides a discharge path for the parallel connected battery. Secondly, a battery typically has a much shorter useful life cycle than the supercapacitor. In a hybrid

system, as the battery reaches the end of its useful life, it will reduce the efficiency of the system and will need to be replaced.

By individually monitoring the charge and discharge behaviour of each storage element, an intelligent storage controller can switch between the units to minimise the number of battery charge and discharge cycles. To evaluate the advantage of the switched-energy storage unit, a scenario of monitoring of aircraft structure around the cargo door using a wireless strain sensor powered by thermoelectric energy harvesting is assumed. A thermoelectric energy harvesting profile (Pearson 2013, Nikolov 2017) has been developed using a single Marlow industries TEG (TG 12-6-01L) measured over temperature gradients between -20^{o}C to +20^{o}C between the inner cargo skin and the primary insulation of aircraft structure near the cargo door. For the experimental purposes of this thesis, this TEG energy source is modelled using a Keysight N6705B DC power analyser and a representative series resistance and was used to charge the batteries and supercapacitors over durations representing both short and long-haul flight cycles. To represent the strain WSN (Becker, Kluge et al. 2009), a pulsed-load scenario was established, again using the Keysight N6705B instrument, over a period of 80 minutes, by generating a pulse profile with a *node-idle* duration (t_o) of 4.95 s and a current demand of 0.07 mA, followed by a *transmission* state with duration (t_1) of 50 ms and a current demand of 14.95 mA, with a total time pulse cycle time (t) of 5s.

This thesis investigates the development of an efficient energy storage and power management system to meet the requirement of an AASM system based on the assumed scenario as detailed above.

1.2 Aims and Objectives

This thesis discusses the need for energy storage in an AASHM powered by thermoelectric energy harvesting. An efficient energy storage system is then developed based on consideration of:

- Autonomous Aircraft SHM
    - Wireless SHM
    - Energy Harvesting
        - Thermoelectric energy harvesting
- Power Management
- Energy Storage
    - Batteries
    - Supercapacitors
    - Simple hybrid energy storage
    - Switched-energy storage

The primary objectives of this thesis are:

- To study different aircraft SHM techniques and the advantages of ASHM over aircraft nondestructive testing (NDT) methods.
- To study the need for autonomous aircraft SHM system and thermoelectric energy harvesting in aircraft structure.
- To carry out the Characterisation of commercially available DC-DC converters for use in an optimised energy storage system.
- To carry out experimental investigations on potentially suitable energy storage options for AASHM.
- To develop an efficient energy storage system for AASHM

1.3 Main Contributions of this Work

1.3.1 Novel Contribution

The novelty claimed in this work is summarised as follows:

- Experimental analysis of the charging and discharging of batteries, supercapacitors and hybrid energy storage elements over a -40^{o}C to +40^{o}C temperature range.
- Experimental analysis of the discharge response of batteries, supercapacitors and hybrid energy charging and discharging to a representative pulsed-load representing strain WSN over a -40^{o}C to +40^{o}C temperature range.
- Demonstration through experimental analysis that run-time extension of WSN compared with standalone battery or supercapacitor is possible using a hybrid energy storage unit.
- Identification of the disadvantages of simple hybrid energy storage.
- Proposal of a novel switched-energy storage along with a switched-storage algorithm

1.3.2 Publications

Journal Publication

Thangaraj, K., Elefsiniots, A., Becker, T., Schmid, U., Lees, J., Featherston, C. A. & Pullin, R. (2014). 'Energy storage options for wireless sensors powered by aircraft specific thermoelectric energy harvester' M*icrosystem Technologies-Micro-and Nanosystems-Information Storage and Processing Systems,* issue 20, pages 701-707.

Conference publication

Thangaraj, K., Elefsiniots, A., Aslam, S., Becker, T., Schmid, U., Lees, J., Featherston, C. A. & Pullin, R. (2013). Hybrid energy storage system for wireless sensor node powered by aircraft specific thermoelectric energy harvesting. *Smart Sensors, Actuators, and Mems VI,* 8763

1.4 Thesis Overview

Chapter 1 contains an introduction to the thesis including the aims and objectives, and the novelty contained within the research.

Chapter 2 discusses the needs, technological challenges and advantages of an autonomous aircraft structural health monitoring system.

Chapter 3 discusses the efficient conversion of the energy from thermoelectric energy harvesters by a rectifier controlled DC-DC converter or two transformer based DC-DC boosters.

Chapter 4 briefly discusses the possible energy storage options for an AASHM system and describes Characterisations carried out on potential batteries and supercapacitors being considered for an AASHM application

Chapter 5 discusses the need for hybrid energy storage for AASHM and explains how a parallel combination of battery and supercapacitor can increase the run time of a wireless sensor node.

Chapter 6 discusses the disadvantages of hybrid energy storage and proposes an efficient energy storage system for AASHM in which an intelligent storage controller switches between units to minimize the number of battery charge and discharge cycles. By individually monitoring the charge and discharge behaviour of each storage element, this system retains the benefits of a hybrid system; combining long-term storage capability with short-term high-power delivery for WSN.

Chapter 7 draws conclusions and makes recommendations for future work

2 Autonomous Aircraft Structural Health Monitoring

AASHM is an emerging technology leading to systems capable of continuously monitoring structures for damage (Farrar, Czarnecki et al. 2002, Farrar and Worden 2007). Aerospace structures have one of the highest payoffs for SHM systems because damage can lead to catastrophic and expensive failures.(Boller 2000) Describes a technology-based SHM as the effort to attach sensors to aircraft structures to monitor signals relating to a physical parameter (e.g. strain, vibration modes, acoustic waves, temperature, electrical resistance, etc.). The existence and/or extent of structural damage is then determined through signal analysis. With the rapid development of sensor and advanced low-power consumption, wireless technology creates an advantage in saving maintenance cost (Chang 2005). In addition, AASHM has the potential to enable robust real-time condition monitoring without adding much weight to aircraft.

AASHM for damage detection could revolutionise the aircraft industry for the following reasons (Derriso and Chang 2006):
(1) Increased safety due to continuous or on-demand monitoring,
(2) Reduced maintenance costs.
(3) Increased accessibility for areas too difficult to inspect, by using embedded sensors, and
(4) Reduces the cost of reinforcing critical areas, as it could be monitored with AASHM sensors.

The aircraft industry faces many challenges to reduce both operational (fuel) and maintenance cost as shown in Figure 2.1. The weight of an aircraft is directly proportional to the operational (fuel) cost (Ramohalli 1992).

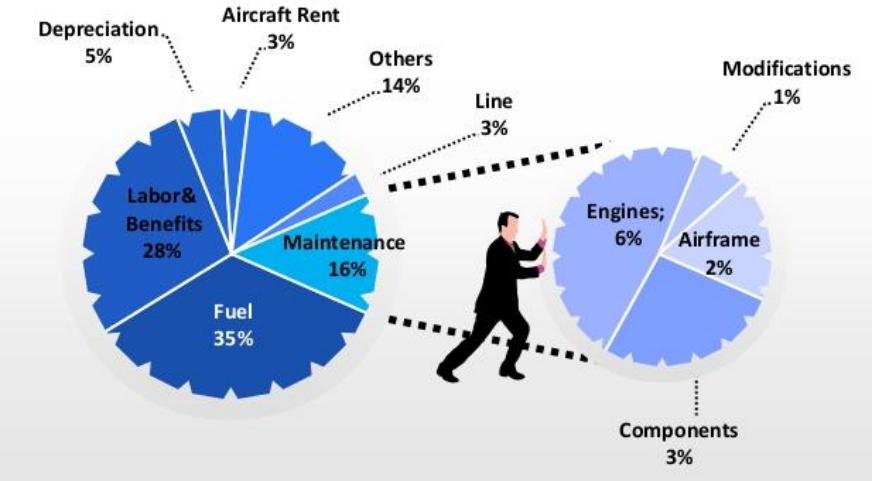

Figure 2.1 Airline operating cost structure (ID Tech Market research 2014)

Many innovations have taken place in the aircraft industry contributing towards weight reduction (Burchell 1999). The percentage of the composite, hybrid materials and advanced aluminium alloys (Noor, Venneri et al. 2000) (Verijenko and Verijenko 2005) in airframes has increased substantially over the years, realising significant weight benefits as shown in Figure 2.2.

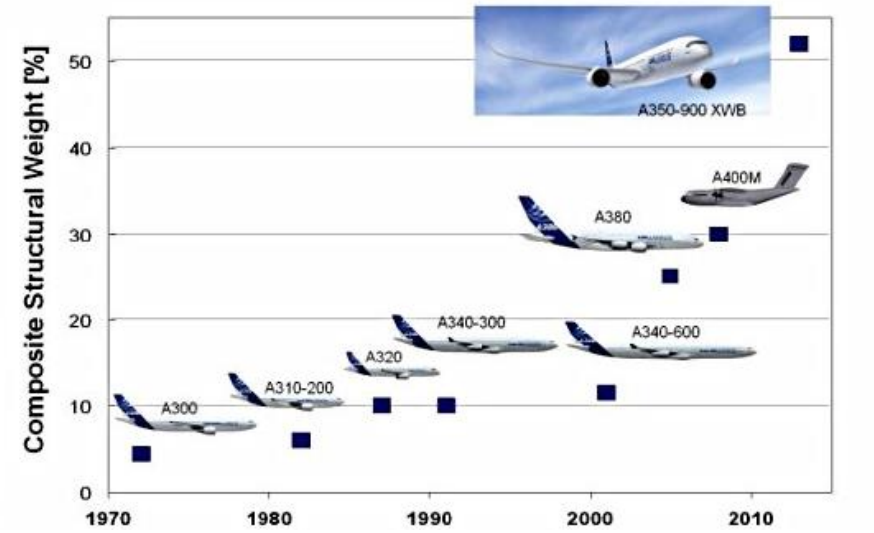

Figure 2.2 Composite structural weight development (AIRBUS CFO Conference 2007)

Both Boeing and Airbus are increasing the percentage of composite material in their new aircraft as shown in Figure 2.3 a and b.

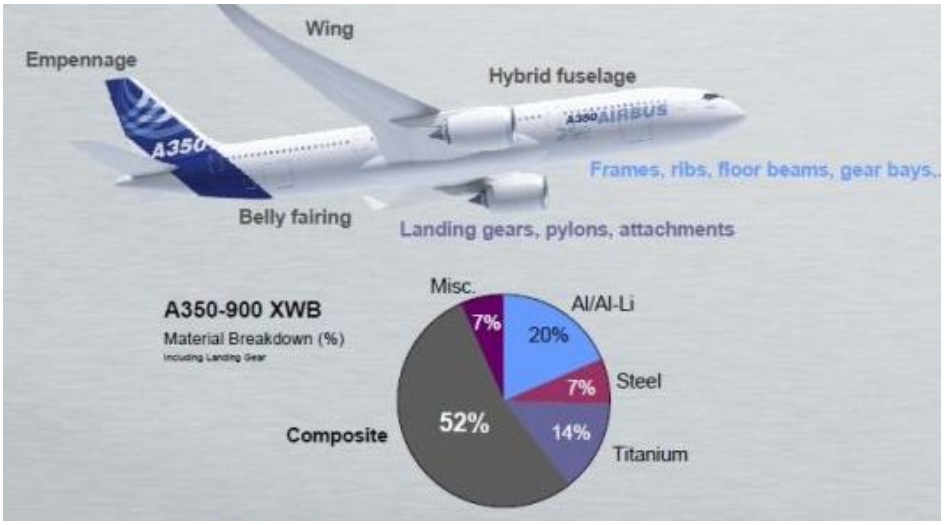

(a)

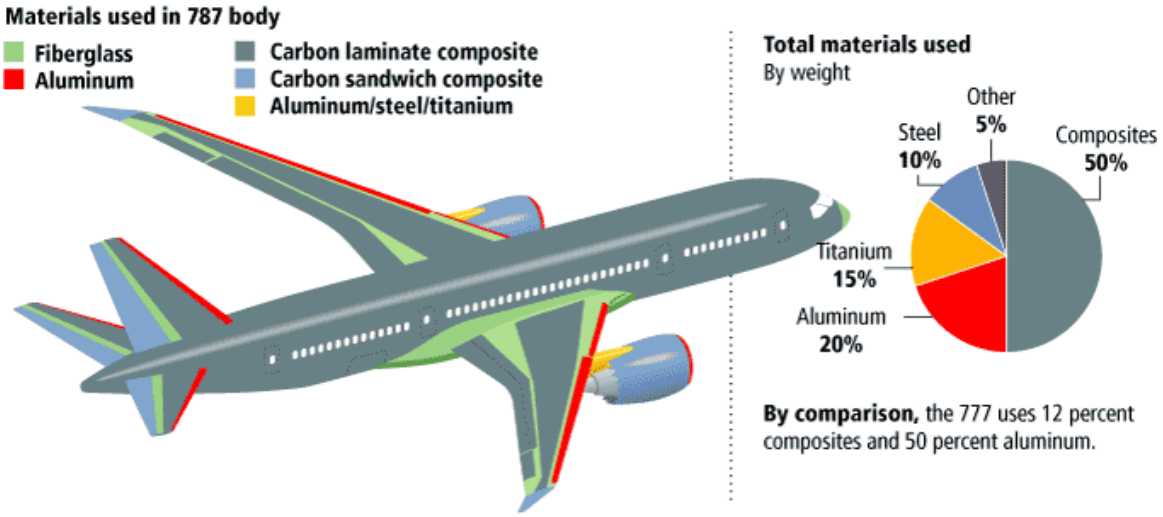

(b)

Figure 2.3 Percentage of composite materials in Airbus A350 and Boeing 787 (Launch events of A350 XWB and Boeing 787)

The second significant cost incurred by the aircraft industry is aircraft maintenance, repair and overhaul (MRO). The MRO industry was worth about $45B in 2007 and is expected to reach $61B of business by 2017 (Chang 2005). MRO is not only about reducing costs but also about increasing the safety of the aircraft. Below are the few examples of passenger aircraft accidents, which have occurred due to structural failure as mentioned in Table 2.1.

Table 2.1 Damage caused due to maintenance failure

Flight	Reason
Japan Airlines, Boeing 747- 1985	The rear pressure bulkhead failed in flight due to a fatigue fracture
Eastern Airlines, L-1011, 1983	On all three engines, magnetic chip detectors had been installed without O-rings, allowing oil to leak from the engines in flight
Aloha Airlines Boeing 737, 1988	The presence of significant disbonding and fatigue damage ultimately led to the failure of a lap joint and the separation of part of the fuselage
Air Midwest, Beech 1900D, 2003	The aircraft was overloaded and had a centre of gravity that exceeded its limits

Aircraft undergo various stress reversals during ground-air-ground cycles, which can cause fatigue cracks to develop as shown in Figure 2.4(Boller, Biemans et al. 1999). These may grow to critical sizes over a period and may lead to catastrophic failure. Efficient aircraft structural health monitoring is therefore required (Boller 2000).

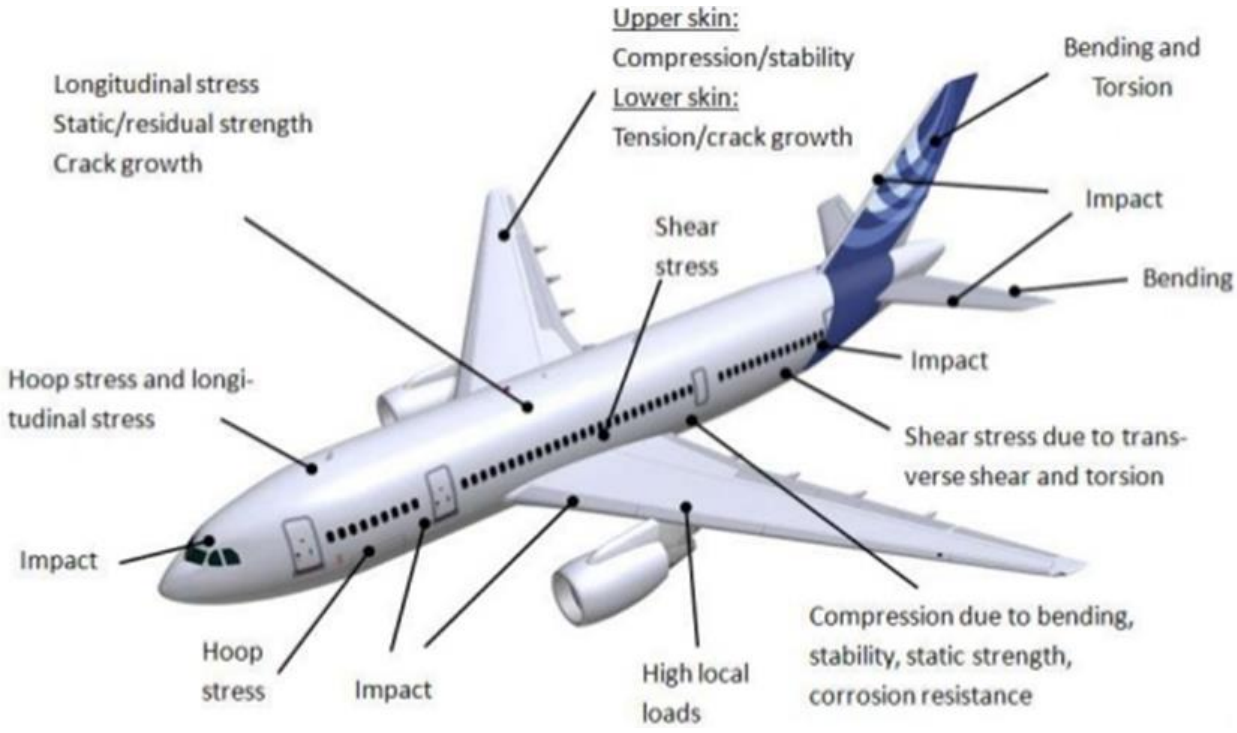

Figure 2. 4 Identified critical locations in an aircraft (Boller 1999)

SHM is defined as the sensors embedded into a structure for continuous and real-time monitoring with a minimum of manual intervention, to monitor the structural integrity of the aircraft (Galea and Baker 2001).

SHM may also include the use of many devices, techniques and systems that are traditionally designated as Non-Destructive Testing (NDT). (Farrar, Czarnecki et al. 2002). Traditional nondestructive testing methods like Dye Penetrant Testing (DPT), Visual Inspection (VI), Magnetic testing (MT), Radiographic Testing (RT) and classical ultrasonic testing (UT) inspection have their own limitations: they are often relatively expensive and inconclusive, cannot be fully automated and integrated into a system, and do not provide prompt information about the initiation and development of damage (PREVOROVSKY, KROFTA et al.). NDT serves to detect discontinuities in solids, at the surface or internally, that are identified as damage. SHM detects local changes in the structure, either in the material properties or connectivity, which are identified by comparing the response of the structure to some stimuli with the response of the pristine structure (Giurgiutiu 2013).

The reliability of NDT can be significantly influenced by human factors (Aldrin, Medina et al. 2006). Humans, as shown in Figure 2.5, examine the output from most NDT techniques, and hence human error brings into question their reliability. Data from a major airline shows 122 maintenance errors over a period of three years to be attributed to omissions (56%), incorrect installations (30%), wrong parts (8%) and others (6%) (Graeber and Marx, 1993)

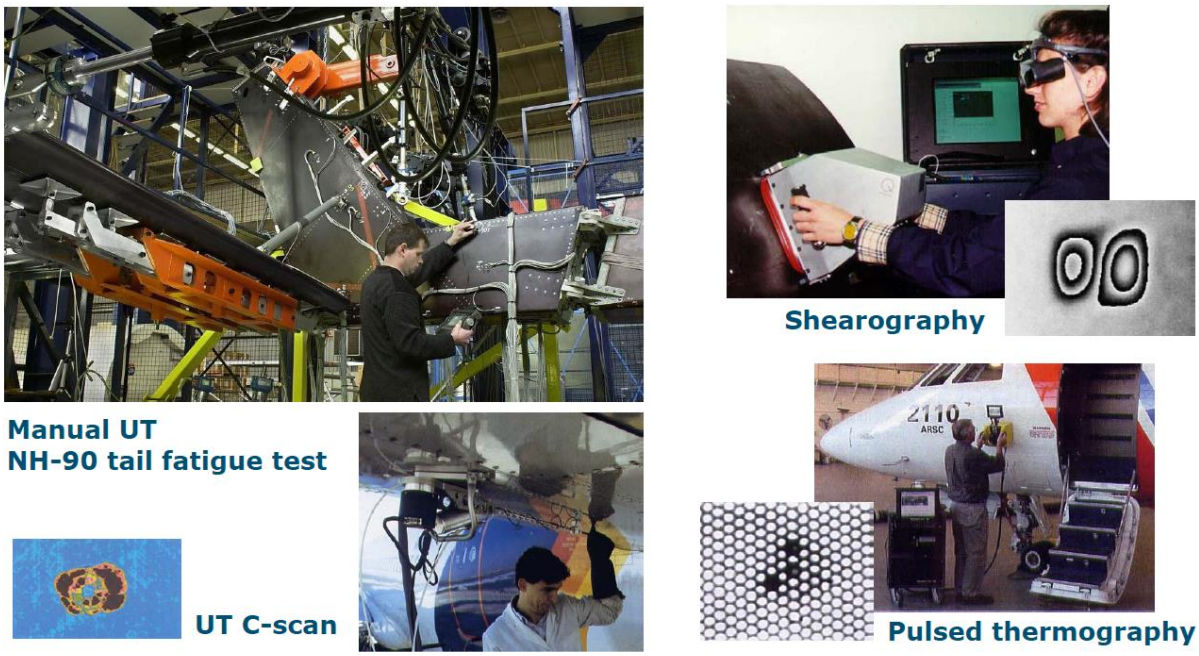

Figure 2. 5 Various aircraft NDT techniques (Graeber and Marx, 1993)

The comparisons between NDT and SHM are mentioned in Table 2.2(Achenbach 2009). It generally involves on-going or repeated assessment of this response. Structures with embedded sensors or smart layer sensor systems needed for complete real-time condition monitoring performance (Staszewski, Boller et al. 2004).

Table 2.2 Comparison of NDT and SHM

NDT	SHM
Inspection is provided by external probes and equipment	Sensors are permanently attached at fixed locations in the structure
Off-line monitoring, parts need to be disassembled for inspection	Online monitoring for aircraft inspection may be done in flight or during overnight stops
Time-based maintenance, checks must be regularly spaced	Condition-based maintenance. Disassemble only when required for repair
Labour-intensive	Evaluation is done without human intervention
Mature technologies are available	Still under development for real aircraft structures

SHM is commonly considered as the acquisition of data from a structure relating to its response to external and internal excitations (Kullaa 2011) . More importantly, SHM includes the data processing to identify the variance in the surface of the structure and thence prognosis to enable prediction of aspects such as capacity and remaining service life. Research on SHM initiated in the late '80s, with the availability of portable computers, which were apparently essential to processing large amounts of data from multiple sensors (Bocca, Cosar et al. 2009). The concept of monitoring prescribes that it is an ongoing, preferably autonomous process rather than one that is used at pre-set intervals of time through human intervention. Thus SHM is necessarily the basis for condition-based, rather than time-based, monitoring providing systems to collect real-time data on ageing and degradation to enable assessment of structural integrity and reliability (Featherston, Holford et al. 2013)

In addition to the demand for a real-time condition for better management of existing aircraft the following factors also contribute to the recent rapid development and advancement of SHM technologies (Hui and Jinping 2011).

- The technological advancements in low- power wireless sensing and electronic circuits, along with the development of highly efficient signal validation and processing methods (e.g. fibre optic sensors (FOSs) and smart materials) (Fu, Liu et al. 2009) ;

- On-going developments in communication technologies and the wide use of the internet and wireless technologies;

- Developments of powerful data transmission and collection systems, and data archiving and retrieval systems;

- Advances in data processing, including damage detection models and artificial intelligence algorithms (Kiremidjian, Kiremidjian et al. 2011).

Although SHM for damage detection and NDT techniques are using the same physical principles, there are notable differences between the two(Chang 1998). NDT detects and assesses the damage based on calibration or reference measurements, while SHM has no reference or calibration specimens. Instead, there are reference or baseline sensor signals (Blackshire and Cooney 2006).

2.1 Types of SHM

Damage assessment involves periodic inspections; therefore, the transition from NDT to SHM is a transition from the traditional "time-based" to the emerging "condition-based" maintenance (Farrar and Worden 2007).

Periodic Monitoring

Structural health monitoring of structures can be either periodic or continuous. Periodic monitoring investigates the structural response and identifies any detrimental change that might have occurred at specified intervals (e.g. weeks, months, or years apart). Analysis of the monitoring data may indicate damage or deterioration. For example, monitoring through static field-testing or moving traffic, monitoring crack growth, monitoring before and after a repair, is done periodically.

Continuous Monitoring

Continuous monitoring, as the name implies, refers to monitoring a structure for an extended period (weeks, months, or years) without interruption. In continuous monitoring, data acquired from the structure is either collected or stored on site (logged) for transfer, analysis, and interpretation later or continuously communicated to an offsite (remote) location. In the most sophisticated of these types of SHM applications, data will be transmitted to a remote location for data processing. This data may also undergo further processing to help with diagnostics and prognostics.

2.2 Types of SHM technology

A number of SHM sensing technologies are currently under development or in use. These can be achieved using sensors that are either surface mounted or incorporated into components during the manufacturing process. Different types of materials are susceptible to different types of damage. For example, the structural anisotropy of composites and the fact that they contain different phases of material (fibre and matrix) leads to various types of potential

damage each of which has different propagation characteristics (Flynn and Todd 2010). Selection of the most appropriate type of sensor is dependent on which of these need to be detected. The most common technologies currently being explored are the following (Majumder, Gangopadhyay et al. 2008).

Fiber Bragg diffraction grating sensor – structures are embedded with optical fibre cables, and the optical interference is laser marked. Variance in the sensor light caused by the stress in the structure can be identified using an interference pattern (Fu, Liu et al. 2009)

Acoustic emission – Acoustic signals occurs during the crack generation are monitored using the transducers, which can be used to locate and characterise damage (Finlayson, Friesel et al. 2001)

Acoustic-ultrasonic - A diagnostic signal is sent through a structure embedded with transducers. Damage causes a change in the signal received, which can be quantified to assess the level of damage.

Smart or sensitive coating – To detect strain coatings with piezo and Ferroelectric elements or carbon nanotubes can be embedded in the structure and spectroscopy will be required to detect the changes.

Microwave sensors – The moisture ingress created between the composite sandwich structures can be identified using small microwave sensors embedded into the structure

Imaging ultrasonic – The flaws or damages in the structure are identified by the signal that generated by a small ultrasonic wave transducer.

Comparative Vacuum Monitoring - The sensors are embedded into the structure and connected to the vacuum source through an accurate flow monitor. The change in flow monitor detects the crack.

Persisting questions about the durability, capability, and reliability of SHM sensors in an operational environment for prolonged overall component life continues to challenge the SHM community. For instance, piezoelectric wafers were analysed during accelerated vibration, temperature, and moisture cycling (Thakur, Nalawade et al. 2011).

2.3 Challenges of ASHM

In both commercial and military aircraft, there are a number of safety critical and non-safety critical systems. These systems are based on wired connections and, are complex and challenging to the route. The Airbus A380, for instance, has over 300 miles of cables consisting of approximately 98.000 wires and 40.000 connectors (Yedavalli and Belapurkar 2011). Traditionally, the sensors deployed in a structure are connected through coaxial wires contributing to this complexity and adding to the weight of the structure.

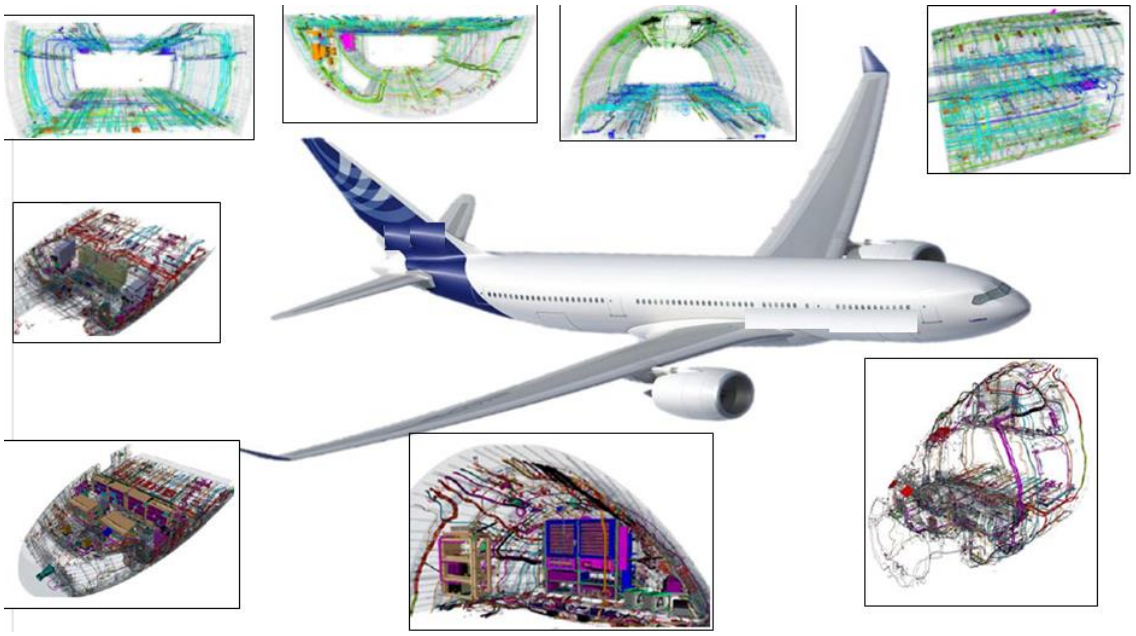

Figure 2. 6 Complex wiring systems in an Aircraft (A380 launch event)

However, the introduction of WSNs offers the opportunity to reduce installation and maintenance costs (Loutas, Panopoulou et al. 2012) by reducing the level of wiring for sensor power and signalling typical wiring for a commercial aircraft can be seen in as shown in Figure 2.6. Furthermore, the compact size and low cost of a single wireless sensor node enable the deployment of a large number of units on the monitored structure, especially in those locations difficult to reach using wires, increasing the screening resolution of the system and introducing the redundancy needed to achieve a robust system. The aircraft manufacturers are therefore working towards an integrated sensor system controlled by the central processor that can build a diagnosis and decide what kind of actions have to be taken as shown in Figure 2.7.

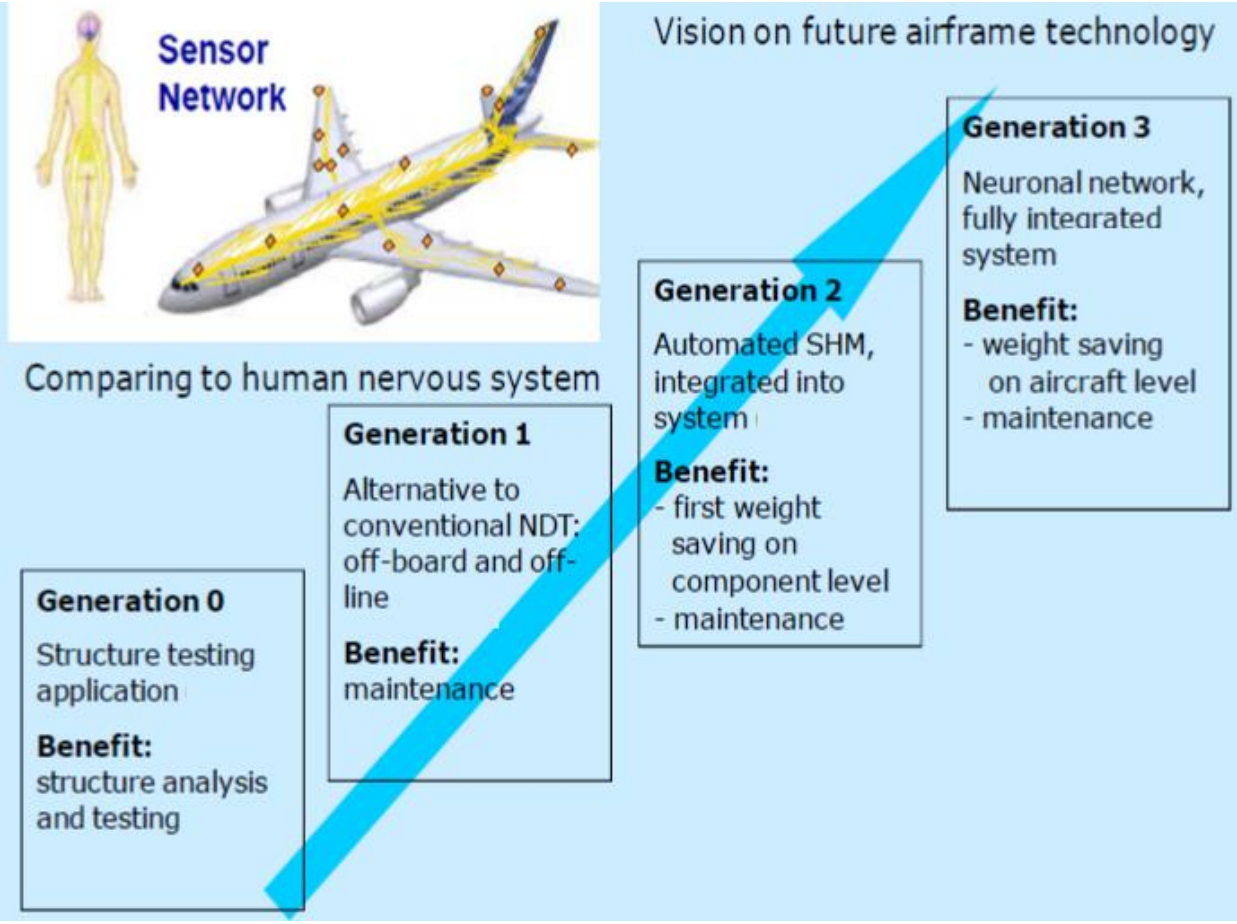

Figure 2. 7 Autonomous aircraft SHM vision of future airframe technology (Airbus SHM event)

Despite the numerous advantages, there are numerous challenges associated with implementing ASHM

- Cost and weight should not exceed the benefits gained (Laveuve, Lehmann et al. 2009).
- Reliability - probably the most significant impediment in the way of ASHM is the unacceptability high instance of false positives. ASHM should not add to uncertainties and complexities, and should not result in unscheduled maintenance due to erroneous interpretation and false calls(Mickens, Schulz et al. 2003)
- The temperature variations that affect both the monitored part and the sensing system. For example, the Lamb waves used in ultrasonic techniques have propagation characteristics which are significantly altered by temperature variations, in addition

to the test piece volume and density changes with temperature (Mandache, Genest et al.).

- Detailed experimental study to be conducted on the aircraft for robust interaction between the sensors and the structure supported by the robust analytical model (Beard, Kumar et al. 2005).
- Sensors are selected based on the aircraft material, such as plain composite or sandwich composite structure. Depending on whether these sensors are surface mounted or embedded sensor locations have the potential to become sources of delamination (Verijenko and Verijenko 2005).
- The robustness and reliability of installed sensors - there may be a need for the sensors to monitor themselves if there is any chance of failure (Blackshire and Cooney 2006).
- Power requirements. Contribute to considerations related to the durability of the SHM sensors. If batteries are needed, then these will have to be low-weight and rechargeable (Dilhac, Montheard et al. 2014). The work contained in this thesis contributes to mitigation of this challenge.

2.4 Energy Harvesting

Critical to the functionality of an AASHM is its ability to be self-powered, and this can potentially be achieved through the use of energy harvesting (Samson, Otterpohl et al. 2010). Energy harvesting is a technique of harvesting energy from ambient sources within the environment. This harvested energy is converted to usable electric power (Priya and Inman 2009). A low-power wireless sensor can be powered using locally harvested energy (Great Britain. Department of Trade and Industry. and Environmental Resources Management (Firm) 2000, Penella-López and Gasulla-Forner 2011). The energy harvesting approach is particularly advantageous in the places where is difficult to trace wiring or where battery replacement is challenging due to access difficulties.

There are various suitable sources of energy, which could be explored, not all of which would be suitable for an aircraft environment. These include:

Thermal energy

- Temperature gradients (thermoelectric effect)
- Heat (pyroelectric effect)
- Solar thermoelectric with focused light (thermoelectric effect)
- Optical energy (photovoltaic effect)
- Radiofrequency (RF) energy
- Radioactive energy

Mechanical energy

- Liquid or gas flow
- Vibrations (piezoelectric effect, electromagnetic, electrostatic)
- Pressure variations (acoustic noise, atmospheric pressure variations)

Electromagnetic energy

- Direct electromagnetic energy conversion

Biochemical energy

- Biochemical fuel cells

An illustrative example of different energy harvesters' potential power densities is given in Table 2.3 (Pearson, Eaton et al. 2012). The stated values describe the overall harvester power density. For instance, the thermoelectric generator power density comprises the heatsink weight, and the vibration generator power density comprises the moving mass (Montalvao, Maia et al. 2006)

Table 2.3 Energy densities of different energy harvesters

Harvester type and operating conditions	*Power density* [mW/kg]
Flexible silicon solar cell inside room or cabin (illuminance: 1000 lx)	9
Flexible silicon solar cell on daylight (illuminance: 10 000 lx)	338
Vibration generator VEH 360 (a = 0.24 m/s^2, 60 Hz)	3
Vibration generator VEH 360 (a = 0.98 m/s^2, 60 Hz)	42
Thermoelectric generator Eureca TEG1-9.1-9.9-0.8/200 (ΔT = 10K)	10
Thermoelectric generator Eureca TEG1-9.1-9.9-0.8/200 (ΔT = 40K)	34

(Kim, Tadesse et al. 2009) identified two primary energy harvesting sources in an aircraft environment - vibration and thermal gradients. For this thesis, work will be focused on thermoelectric energy harvesting, as it is widely available within the structure as shown in Figure 2.8 which illustrates potential sources of thermal energy arising from temperature gradients.

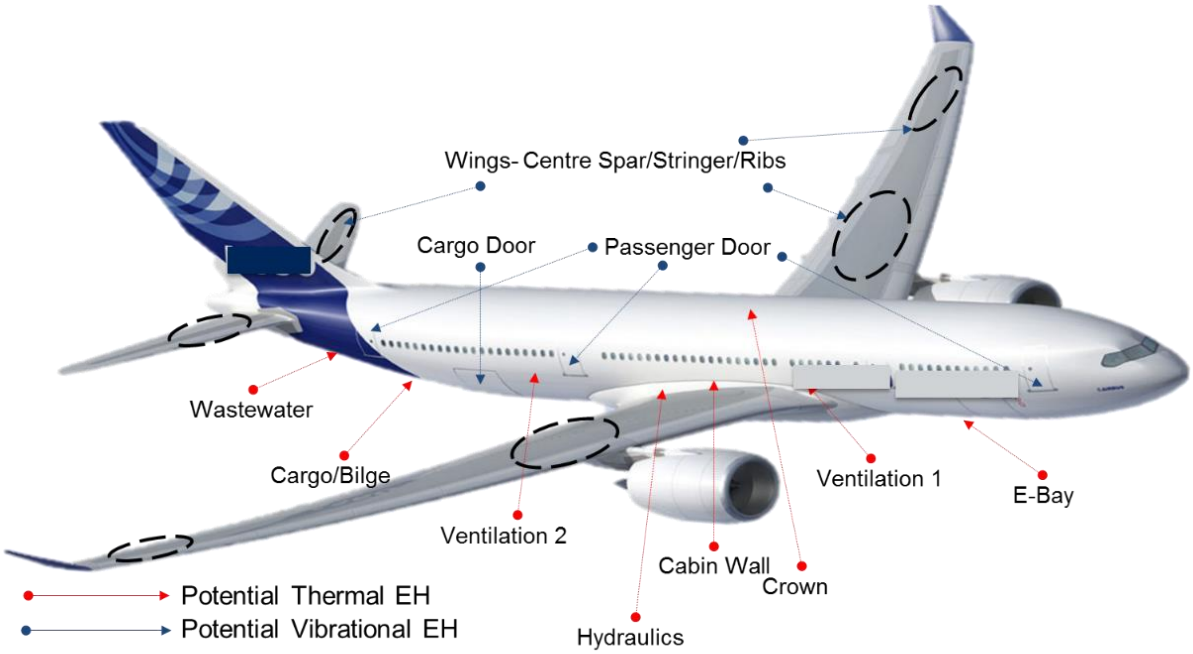

Figure 2. 8 Possible location of energy harvesting sources (Flight image taken from Airbus website a320family/a318/)

2.4.1 Thermoelectric Energy Harvesting

Thermo-electric generators (TEGs) convert heat difference directly into electric energy and can be used in low-power wireless systems. TEGs comprise thermoelectric modules made up of a number of series-connected P-N junctions, sandwiched between two parallel ceramic plates as shown in Figure 2.9. TEGs generate DC output voltage using the Seebeck effect, when the two sides of the TEG are at different temperatures. The magnitude of the output voltage is proportional to the magnitude of the temperature between the plates (Rowe 2012).

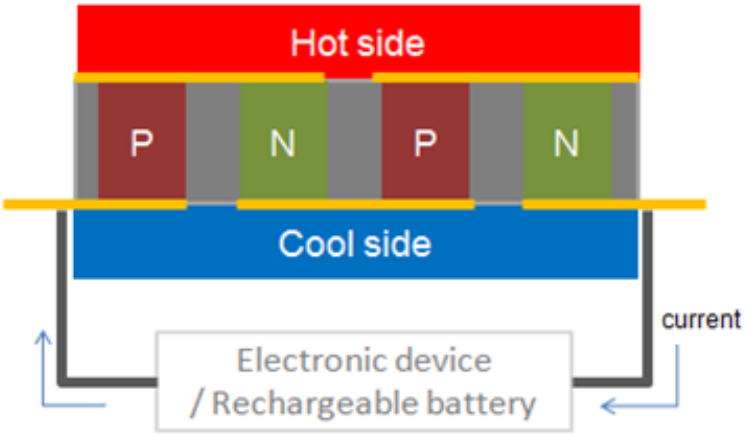

Figure 2. 9 Overview of TEG (Janák, 2014).

A sandwich implementing an array of n- and p-type semiconductor legs, as shown in Figure 2.10, creates the typical TEG module. The legs are typically pellets of either bismuth telluride or antimony telluride. The legs are strapped together to create a series electrical connection and a parallel thermal connection. The top and bottom of the module is most often aluminium oxide ceramic to provide electrical insulation and excellent thermal conductivity

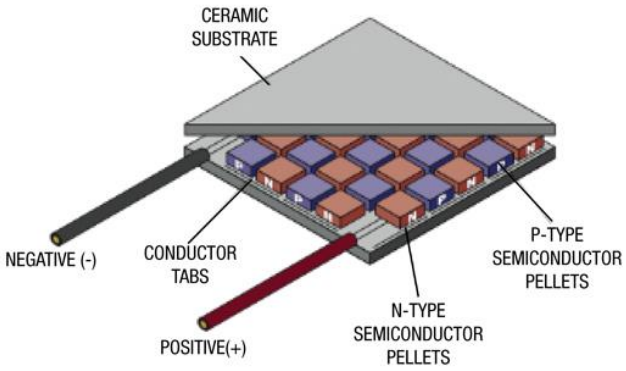

Figure 2. 10 Internal crosses sectional view of TEG (Janák 2014)

Table 2.4 lists some of the locations with respect to Figure 2.8, which shows the most potential for energy harvesting along with temperature differences and peak/average generated electric power (Featherston, Holford et al. 2009). The stated values are based on a computer simulation. The thermoelectric module under consideration is the Micro pelt TGP-751.

Table. 2.4 Opportune locations for placement of TEGs on an aircraft – temperature differences and output powers (Pearson, 2013)

Spot (cold and hot side)	ΔT_{peak} [°C]	$P_{el,peak}$	$P_{el,Avg}$
cargo skin / cargo primary insulation	40	34.15	22.58
hydraulic pipeline 1 / hydraulic pipeline 2	20	7.97	3.07
waste water tank / waste water ambient	15	5.46	2.99
engine bay fuselage skin / engine bay primary insulation	35	18.72	6.42
cabin wall fuselage skin / cabin wall primary insulation	30	13.36	3.97
cabin wall fuselage skin / cabin wall secondary insulation	40	30.06	11.70

A dynamic thermoelectric energy-harvesting device advantageously uses the temperature changes within the aircraft operating envelope such as those which occur after take-off. The dynamic thermoelectric generator concept is shown in Figure 2.11 (Elefsiniotis, Becker et al. 2014). The temperature difference is created using a phase-change material (PCM) attached to one side of the thermoelectric generator which maintains a temperature differential with the ambient temperature on the other side. The PCM acts as a heat store. It holds the higher ground temperature according to its heat capacity while the outside ambient temperature decreases. When the heat transmission is over, and the temperature of the PCM reaches the phase-change temperature, additional heat is produced due to the phase-change of the material. The landing scenario works in the opposite way. The PCM is cold while the ambient air is hotter. The phase-change occurs in the opposite direction.

The heat available during the dynamic TEG operation can be described as

$$Q_a = \int_{T_h}^{T_{pch}} mC_{lp}(T)dT + m\Delta H + \int_{T_{pch}}^{T_c} mC_{sp}(T)d \qquad (2.1)$$

Where Q_a is the available heat, m the mass of PCM, T_h is the hot-side temperature, T_{ech} is the phase-change temperature, T_C is the cold-side temperature, C_{lp} is the heat capacity of PCM in Liquid phase, ΔH is the latent heat of phase change, *and* C_{sp} is the heat capacity of PCM in solid phase. The corresponding part of Q_a can be transferred to useful electric power using thermoelectric energy conversion (Elefsiniotis, Kiziroglou et al. 2013).

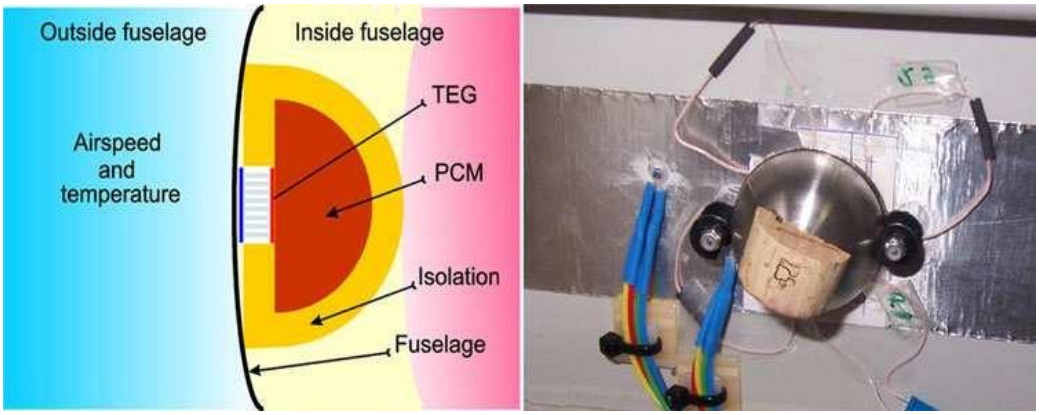

Figure 2. 11 Practical realizations of a dynamic thermoelectric generator and thermoelectric generator with phase change material (Elefsiniotis, Kiziroglou et al. 2013).

Energy harvesting devices can present a more sensible option for energising low-power wireless electronic devices and in many cases, can become the sole energy source. Harvesting energy in an aircraft structure is not a constant function (Pearson, Eaton et al. 2012). There is a period for example when there is a surplus of energy harvesting possible, such as take-off and landing as shown in Figure 2.12 and 2.13. The surplus energy should be stored efficiently and can be used for SHM purposes on the ground. The two main types of energy storage device available are batteries and supercapacitors.

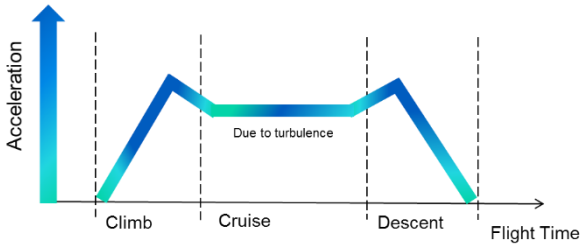

Figure 2.12 Availability of vibration acceleration during a typical flight cycle

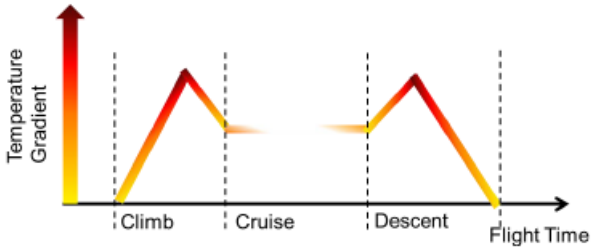

Figure 2.13 Availability of temperature gradient during a flight cycle

2.5 The Adopted Scenario - monitoring of aircraft structure around the cargo door using wireless strain sensor powered by thermoelectric energy harvesting

Wide-ranging research is now being carried out on potential ASHM wireless sensor nodes. Various sensors have been investigated for SHM applications, including amongst others, temperature, humidity, strain, crack-wire, accelerometer, ultrasonic and passive-acoustic. Most of the ASHM wireless sensors operate over a voltage range between 3.3 to 5 Volts as most use commercially available low-power, low voltage microcontrollers.

On a typical commercial flight, the cargo door will be the last section of aircraft to be operated, and a final structural check will typically be performed around the cargo door before take-off. At the start of this work, it, therefore, made sense that, for the experimental purpose of this thesis, the scenario adopted was the need to monitor aircraft structure around the cargo door using a wireless strain sensor at both post-landing and pre-take-off time events.

For a short-haul commercial flight, there will be typically a minimum of 2.5 hours between each 80-minute flight cycle, so this scenario is divided into 60 minutes of post-landing monitoring, 30 minutes servicing time and 60 minutes pre-take off monitoring. In this work, for example, it is shown how a supercapacitor will be charged twice from the battery; during the 30 minutes of servicing time after landing and then again 30 minutes during taxing before take-off. The temperature difference between the fuselage skin around the cargo door *C* and the primary insulation *Iso,C* is assumed to vary between -20^{o}C to +20^{o}C as shown in Figure 2.14 cycle, but it should be noted that the temperature can vary over wider ranges, between -40^{o}C to +40^{o}C at other aircraft locations (Pearson 2013). Around the aircraft hull section, for example, the temperature range can be expected to be -30^{o}c to +30^{o}C (Samson, Kluge et al. 2011).

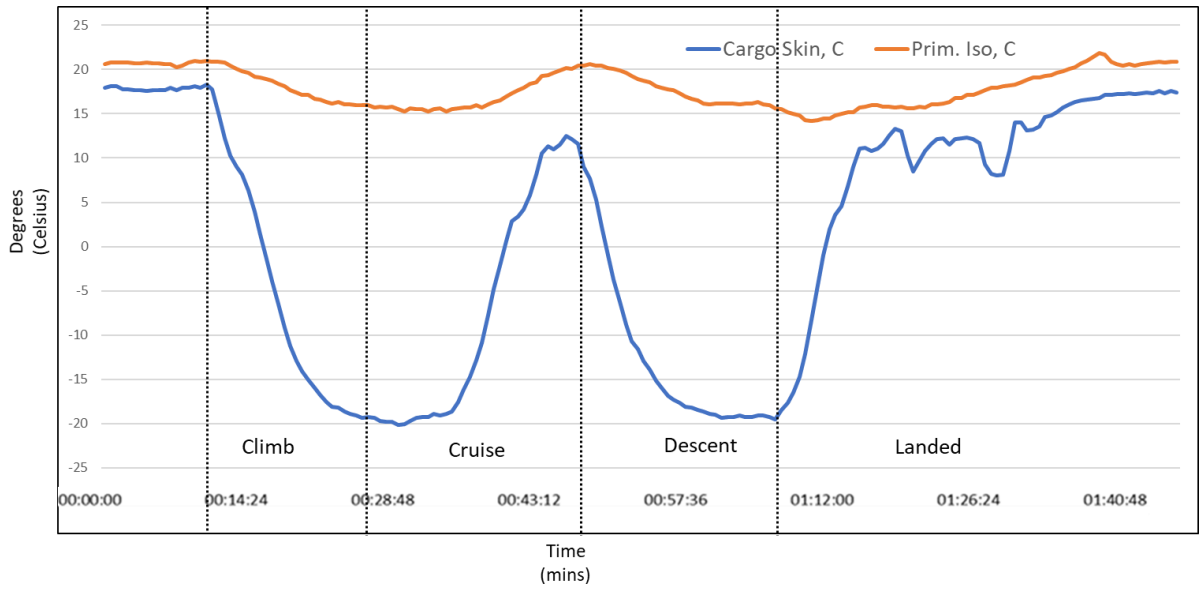

Figure 2.14 Availability of temperature gradient during a typical short-haul flight cycle (Pearson 2013)

Within this scenario, batteries and supercapacitors are the storage element options considered for powering the WSN. The operational behaviour of both battery and supercapacitor have been characterised over worst-case conditions, by charging and discharging these elements over 80 minutes in the extended temperature range of -40°C to +40°C. 80 minutes duration is typical of a short-haul commercial flight time, and it is chosen as the basis for these experiments. In such a short-haul flight, the temperature around the aircraft structure varies over a relatively short period of time, as shown in Figure 2.15. However, in long-haul flight scenarios, here considered to be a maximum of 13 hours and 40 minutes, the temperatures around the aircraft structure can be static for longer periods. Experimentally studying how energy storage elements behave over a temperature range between -40°C and +40°C for sustained durations of 80 minutes will be helpful in understanding the influence of temperature in ASHM sensors in long-haul flight scenarios.

In the scenario where a WSN is powered by an energy harvesting unit and fixed to the aircraft structure (Samson, Kluge et al. 2011), as shown in Figure 2.15, the electronics can be expected to experience the same temperature variation. Even though in this scenario, the cargo door monitoring will typically be performed on the ground where the temperature will be 'normal', it is envisaged that in the future, aircraft real-time condition monitoring will be performed

whilst airborne, so it is necessary to understand the energy storage element discharge behaviour in combination with electronics in this temperature range of -40^{o}C to +40^{o}C.

Figure 2.15 Prototype of ASHM sensor powered by thermal energy harvester attached to the inside of an aircraft hull(Samson, Kluge et al. 2011)

In order to accurately characterise both the battery charge and discharge characteristics, as well as the WSN the dynamic power demand, it is necessary to accurately source and measure the dynamic voltage and current at the terminals of these devices, under different scenarios. The Keysight N6705B is a DC Power Analyser that can be configured to source and measure such DC voltages and currents. The analyser has a four-slot module option and control & analysis software (14585A), through which data visualisation and data management can be achieved. Additional modules such as the N6781A:2-Quadrant Source/Measure Unit for Battery Drain Analysis in channel 1 and N6784: 4-Quadrant General-Purpose Source/Measure Unit in channel 2 will be used for most of the experiments presented in this thesis.

A good wireless ASHM system should be energy-efficient, should not be affected by the electromagnetic interference from other equipment and should be capable of real-time acquisition of structural health status and transmission of data with high precision. A WSN is a central unit, that may form part of an ASHM system, that combines mechanical measurements and communication tasks. It is necessary for every component of the WSN

system to adopt inherent energy-saving properties or techniques to prolong the operational time of each sensor node. Strain sensors are resistive elements that change resistivity with stress and are suitable candidates for ultra-low power (ULP) applications. To achieve ULP consumption, however, strain sensors should be selected carefully (von Allmen, Bailleul et al. 2017) . In addition, WSNs must minimise *passive listening* - time spent listening to an empty channel, *overhearing* - time spent listening to traffic addressed to other nodes and *over emitting* - sending messages when the destination node is saving energy in sleep mode. This can generally be achieved with a medium access control (MAC) protocol layer. Such systems based on MAC protocol have already been proposed for aeronautical applications (Sabater, Kluge et al. 2007).

A ULP wireless strain sensor with a 5KΩ resistance based on WSN MAC protocol is proposed in. The sensor platform is controlled using a low-power (MSP430 series) microcontroller and employs a 2.4GHz IEEE 802.15.4 standard (Chipcon 2420 series) RF transceiver. At an operating voltage of 3.3V, the dynamic power consumption of the complete wireless sensor under typical operating conditions was tabulated below in Table 2.5 (Becker, Kluge et al. 2009).

Table. 2.5 Current and Power Consumption of the wireless strain sensor node.

Sensor Sampling	0.16mA	0.53mW
Sensor Switching	4.77mA	15.7mW
Sensor on	0.75mA	2.5mW
Transmission	14.95mA	49.3mW
Node-idle	0.07mA	0.2mW
Average	0.87mA	2.9mW

To understand the temperature influence on the discharge of the battery and supercapacitor under realistic operational conditions, the lowest power consumption mode (*node-idle*) and highest power consumption mode (*transmission*) as shown in Figure 2.16, were used to approximately model the WSN for experimental purpose. Using the Keysight N6705B, a pulse-load scenario was established over a period of 80 minutes, by generating a pulse profile with a *node-idle* duration (t_o) of 4.95 s and a current demand of 0.07 mA, followed by a

transmission state with duration (t_1) of 50 ms and a current demand of 14.95 mA, with a total time pulse cycle time (t) of 5s as shown in Figure 2.17. The representative pulsed-load timings were specified by the industrial sponsor, Airbus.

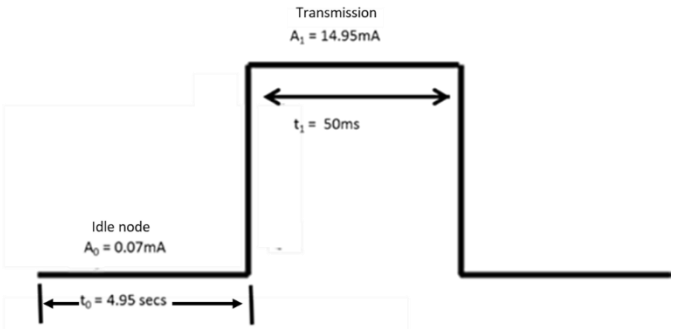

Figure 2. 16 Pulse loads representing a wireless sensor function of *node-idle* and *transmission*

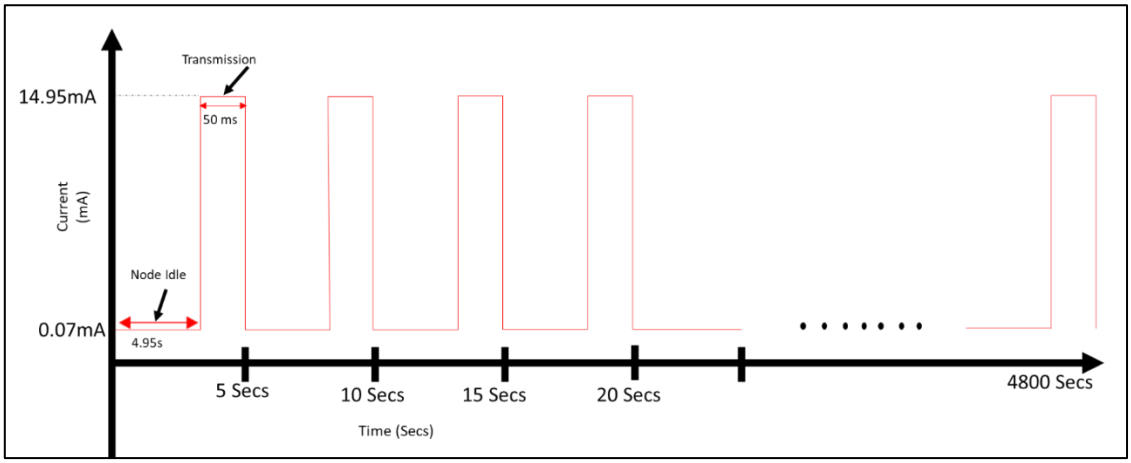

Figure 2. 17 Pulsed-loads representing a *node-idle* and *transmission* state of the wireless strain sensor over 80 minutes

The arbitrary pulsed-load waveform shown in Figure 2.17 was generated using the N6705B DC power analyzer as an electronic load, as shown on screen in Figure 2.18. The waveform represents the *node-idle* and *transmission* states of strain WSN, driving the electronic load to discharge the batteries and supercapacitor, emulating the actual WSN.

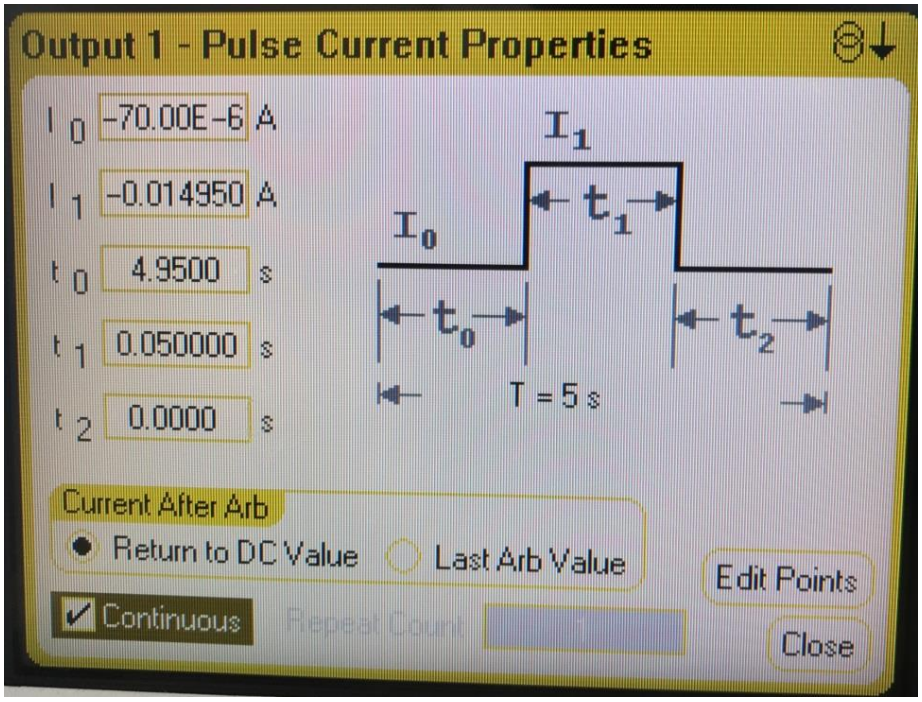

Figure 2.18 A pulse waveform representing a wireless sensor load function was programmed into the Keysight N6705B.

2.5.1 Thermoelectric Energy Harvesting Profile

As is discussed in section 2.3, in order to make a WSN truly autonomous, the sensor should be powered from locally harvested thermoelectric energy, removing the constraint of running power cables across the airframe structure. Thermal energy harvesting relies on the Seebeck effect. This is based on the diffusion of electrons through the interface between two different materials. Heating causes net changes in the materials and allows electrons to move from material where they have lower energy into material where the energy is higher. Because electrical current is a flow of electrons, this effect of passing electrons from one material to another creates an electromotive force (voltage) across the terminals of the thermoelectric module. The open circuit voltage generated is linearly dependent on the temperature difference between the hot and cold sides of a thermoelectric module as described by equation 3.1 (Priya and Inman 2009) .

$$U_{oc=\propto_{\epsilon}\Delta T} \qquad (2.1)$$

Where U_{oc} is the open circuit voltage at the output terminals of the thermoelectric module, α_ε is the net Seebeck coefficient of the thermoelectric module (TEM), and ΔT is the temperature difference along the module (*Th –Tc*).

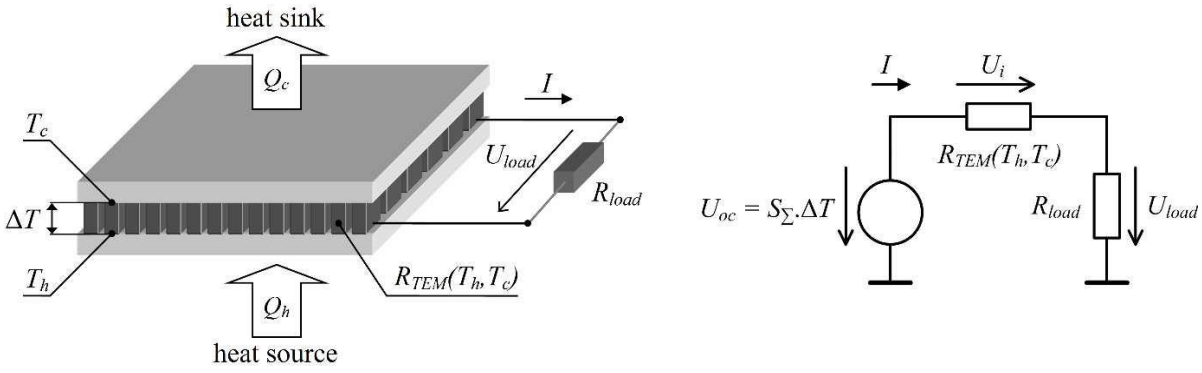

Figure 2.19(a) Thermoelectric module (b) its equivalent circuit (Priya and D. J. Inman 2009)

Figure 21.9 (a) shows a typical TEM and Figure 2.19 (b) explains the equivalent circuit in terms of Thévenin's theorem. This circuit is comprised of an ideal voltage source according to equation 2. 2, the internal resistance R_{TEM} and load resistance *Rload*. The output voltage across the load can be considered as the voltage at the centre of the voltage divider comprising R_{TEM} and R_{load}.

$$U_{load} = \frac{R_{load}}{R_{load}+R_{TEM}} U_{oc} \qquad (2.2)$$

Thus, the power which can be delivered to the load is strictly dependent on the internal resistance of the module and the resistance of the load connected across its terminals. The maximum power P_{MPP} which can be delivered to the load is.

$$P_{MPP} = \frac{(\alpha_\varepsilon \Delta T)^2}{4RTEM} \qquad (2.3)$$

Maximum power transfer can be achieved only under the condition:

$$R_{load} = R_{TEM} \qquad (2.4)$$

This state is called the impedance match. Unfortunately, there are few applications where the internal resistance of the TEG will be matched by the energy harvester. Moreover, the internal resistance R_{TEM} is a function of module temperature (Th, Tc). Differences between R_{TEM} and R_{load} are usually significant. Dynamic impedance matching is of high importance in the design of power management electronics for an energy harvesting device (S. Priya and D. J. Inman 2009). Dynamic impedance matching is usually implemented using a switching converter controlled by a Maximum Power Point Tracking (MPPT) driver (Penella-López 2011).

In (Pearson, 2013), a detailed study was performed to understand the thermoelectric energy harvesting output from different aircraft locations. Based on this study, a TEG output profile was modelled using a single Marlow industries TEG TG 12-6-01L (Nikolov,2017). The internal resistance of TEG TG 12-6-01L was measured to vary between 1 Ω and 2 Ω over temperatures between -20 °C and +20 °C, so for the purposes of simple modelling, a 1.4 Ω resistor was used as R_{TEM} and same value resistor was used as load resistance R_{load} to achieve the maximum output power of 31 mW. The output voltage and power achieved are shown in Figure 2.20 and 2.21 respectively.

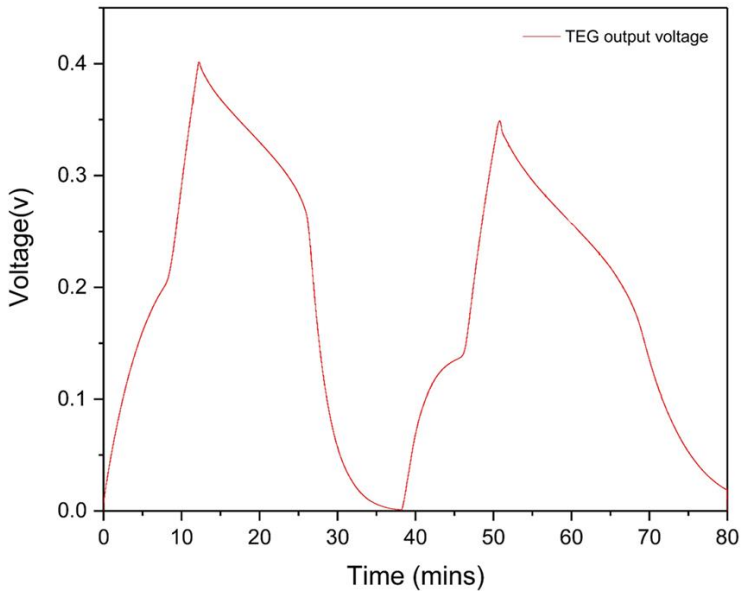

Figure 2.20 Thermoelectric energy harvesting output voltage from single Marlow industries TEG TG 12-6-01L with 1.4 Ω load resistance, near cargo door of commercial flight

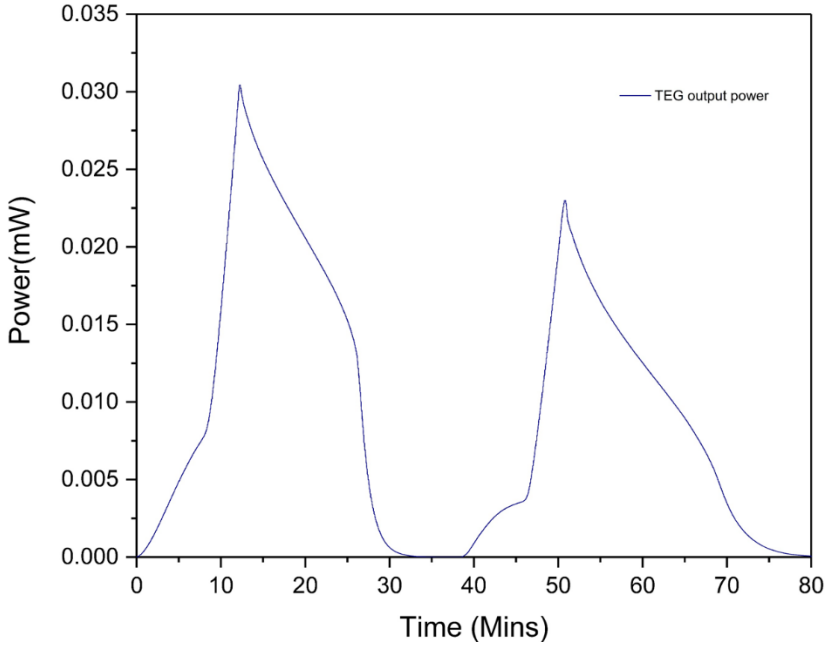

Figure 2.21 Thermoelectric energy harvesting power output from single Marlow industries TEG TG 12-6-01L with 1.4 Ω of load resistance, near cargo door of commercial flight

In an attempt to model the approximate behaviour of the TEG, the output voltage profile of Marlow industries TEG TG 12-6-01L as shown in Figure 2.20 was programmed into a DC source to generate the voltage. The generated output voltage was then provided as an input to a DC-DC converter, LTC 3109 through the modelled series resistance R, as discussed above. With LTC 3109 as load, the value of R was selected as 1.3 Ω, the maximum output power achieved was 27.20 mW as shown in Figure 2.22. 1.3 Ω was the closest value resistance available to the actual 1.4 Ω resistance of Marlow industries TEG TG 12-6-01L.

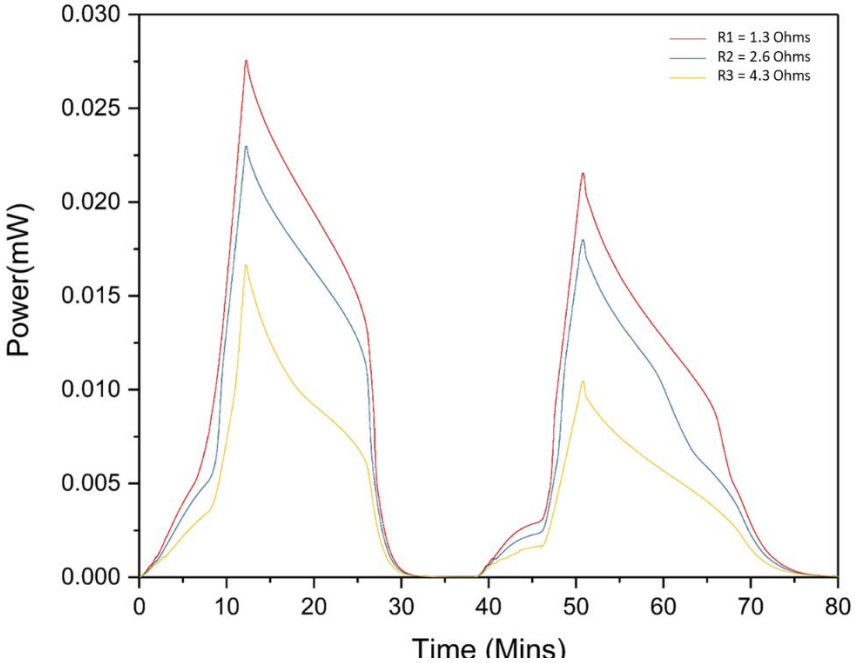

Figure 2.22 Comparison of generated thermoelectric energy harvesting power output with various series resistance, between generated output voltage and the load LTC3109

Two different methods were used to create the TEG power output profile; i) using LabVIEW with a National Instrument data acquisition system (Nidaq USB6211) and ii) using the Keysight N6705B DC power analyser, controlled by Keysight 14585A software. When compared, the latter approach using the Keysight control and analysis software was identified as the most efficient method, with less external hardware components required. The synthesised TEG output voltage profile was then used, together with a 1.3 Ω series resistance, to charge and compare the storage components. An LTC 3109 DC-DC converter from Linear Technologies was used to establish the correct charging voltage and will be discussed more detail in chapter 3.4.1.

2.5.1.1 LabVIEW using Nidaq6211

National Instruments LabVIEW code was written, as shown in Figure 2.24, to read the voltage profile from a text file, and the voltage generated as an output from Nidaq 6211, as shown in Figure 2.23. The disadvantage of this approach is the maximum current output from the Nidaq 6211 is 2mA which is not enough to initiate charging of the energy storage elements.

The code reads the data from TXT file stored on the local computer and uses it to create an array containing voltage and time. The voltage is provided as an output from one of the analogue channels of the Nidaq6211, with the timing interval established from the second column of the array. The voltage generated was delivered as input to the LTC 3109 through 1.3 Ω resistor in series. The voltage generated by the Nidaq 6211 and the output from LTC 3109 were logged at 1 sample per second. This data was then converted to an array and written to an Excel compatible file format.

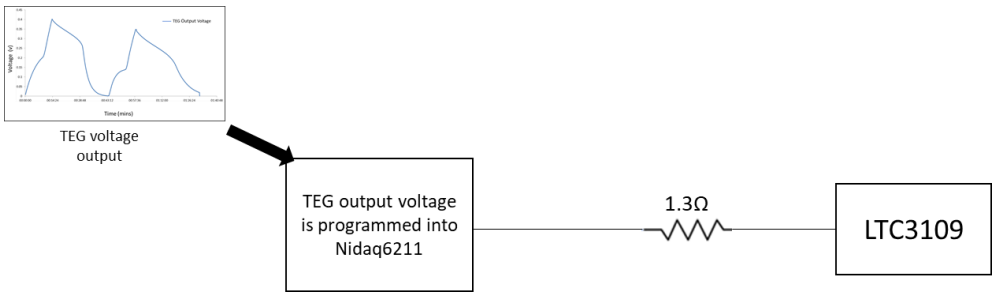

Figure 2.23 Thermoelectric energy harvesting emulation environment comprising a series 1.3 Ω resistance, Nidaq 6211 data acquisition/generation board and LTC3109 DC-DC converter

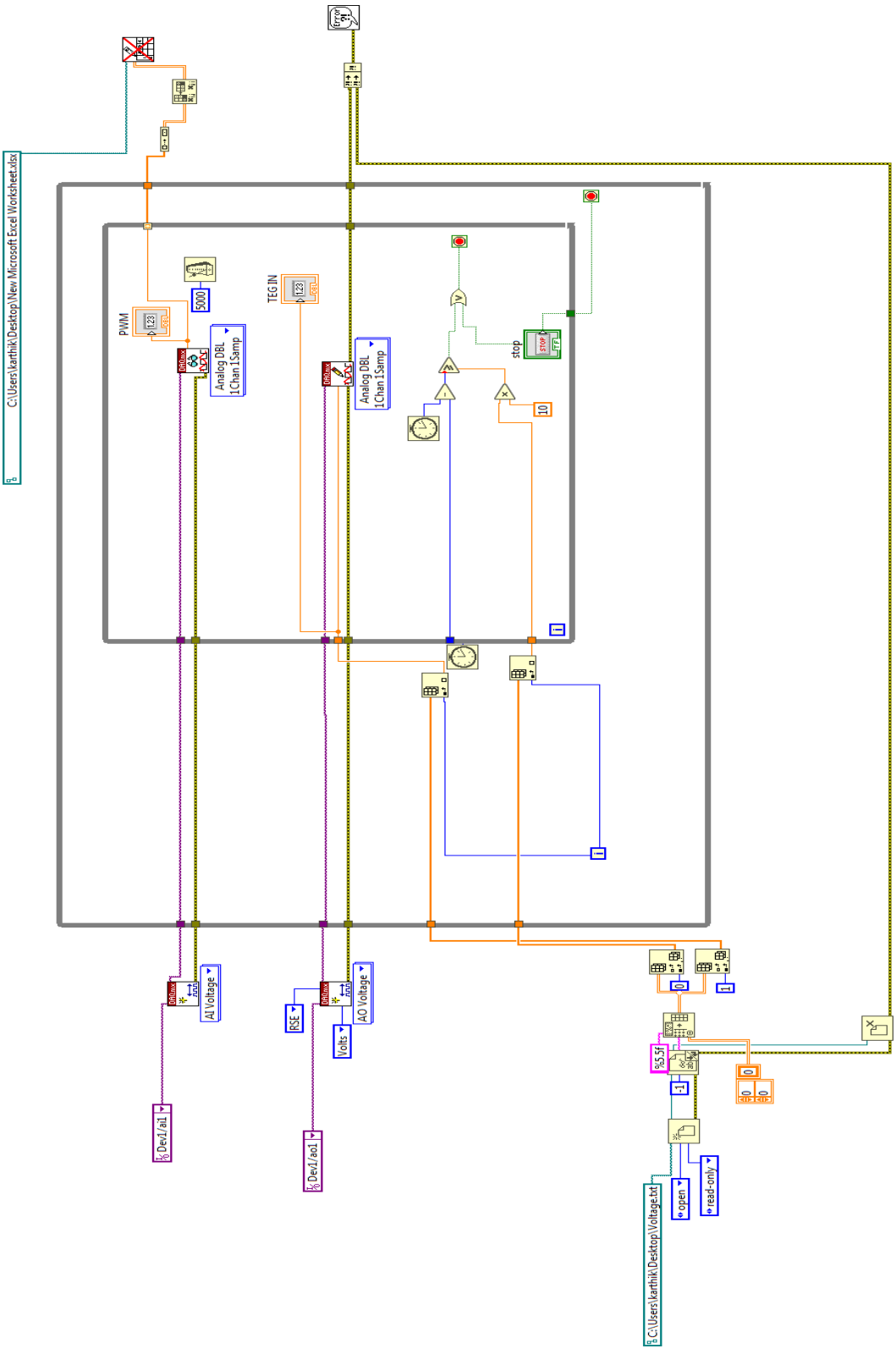

Figure 2. 24 LabVIEW code for thermoelectric energy harvesting power profile

2.5.1.2 Keysight 14585A control and analysis software with the N6705B DC Analyser

Using the 14585A control software, the voltage from channel one of the N6705B DC analyser is selected, and marked as a user-defined waveform. The current from the channel was not limited the maximum output current of N6705B is 3 A. The voltage waveform can be manually entered, or a CSV file format can be imported. The repeat count is set as 1, to create one arbitrary waveform. The generated output voltage from N6705B is given as input to LTC 3109 through a series resistance of 1.3 Ω as shown in Figure 2.4

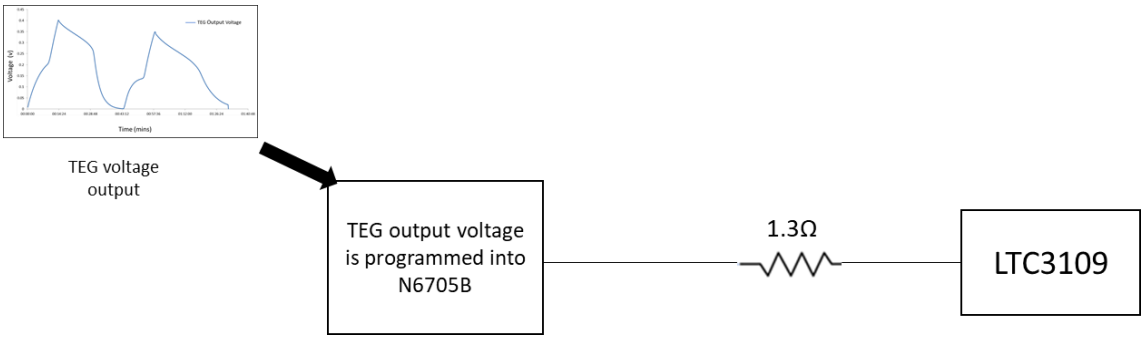

Figure 2.25 Thermoelectric energy harvesting power output profile in series with 1.3 Ω programmed using N6705B

As shown in Figure 2.26, the N6705B will generate the output power profile of a TEG. The maximum output power of 37.51 mW was achieved. The generated output voltage profile is delivered to the input to the LTC 3109 DC-DC converter.

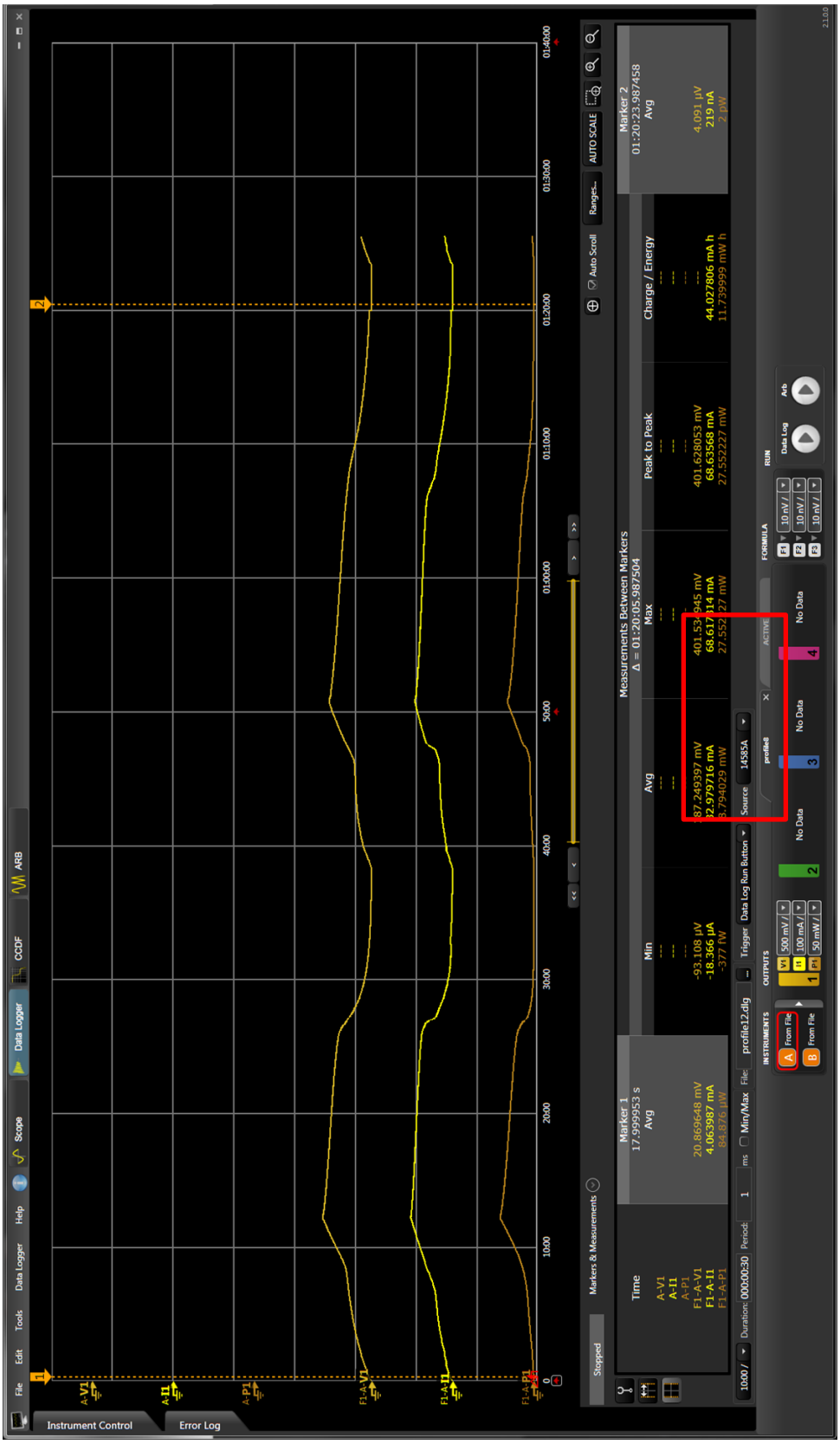

Figure 2.26 - TEG energy output profile created using N6705 B showing voltage, current and measured power. The output profile was displayed in 14585A control and analysis software

2.6 Summary of AASHM

Structural health monitoring systems can be designed to be autonomous if a suitable source of energy can be harvested from the ambient environment. Energy harvesting systems generally consist of energy harvesting elements, energy storage elements and interface power electronics. The harvested power must be converted to electricity and transformed into an appropriate form for charging the energy storage element and supplying the final application (Becker, Kluge et al. 2009). This application can take a number of forms. Some of the aircraft wireless applications that can be powered using thermoelectric energy harvesting are shown in Figure 2.27.

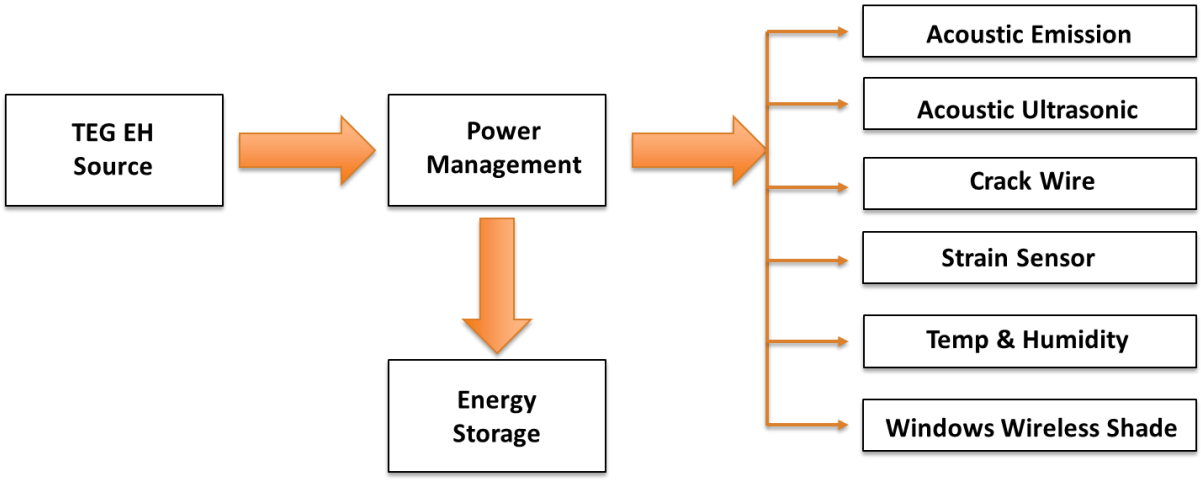

Figure 2. 27 Overview of aircraft structural health monitoring system powered by thermoelectric energy harvesting

AASHM has been the focus of significant collaborative research work in both industry and academia enabling it to reach a level of maturity that enables it to be tested on experimental flights (Farrar and Worden 2007). The research and development of AASHM are as shown in Figure 2. 28. This thesis describes work carried out to improve the efficiency and mainly cycle-life of an appropriate energy management and storage system.

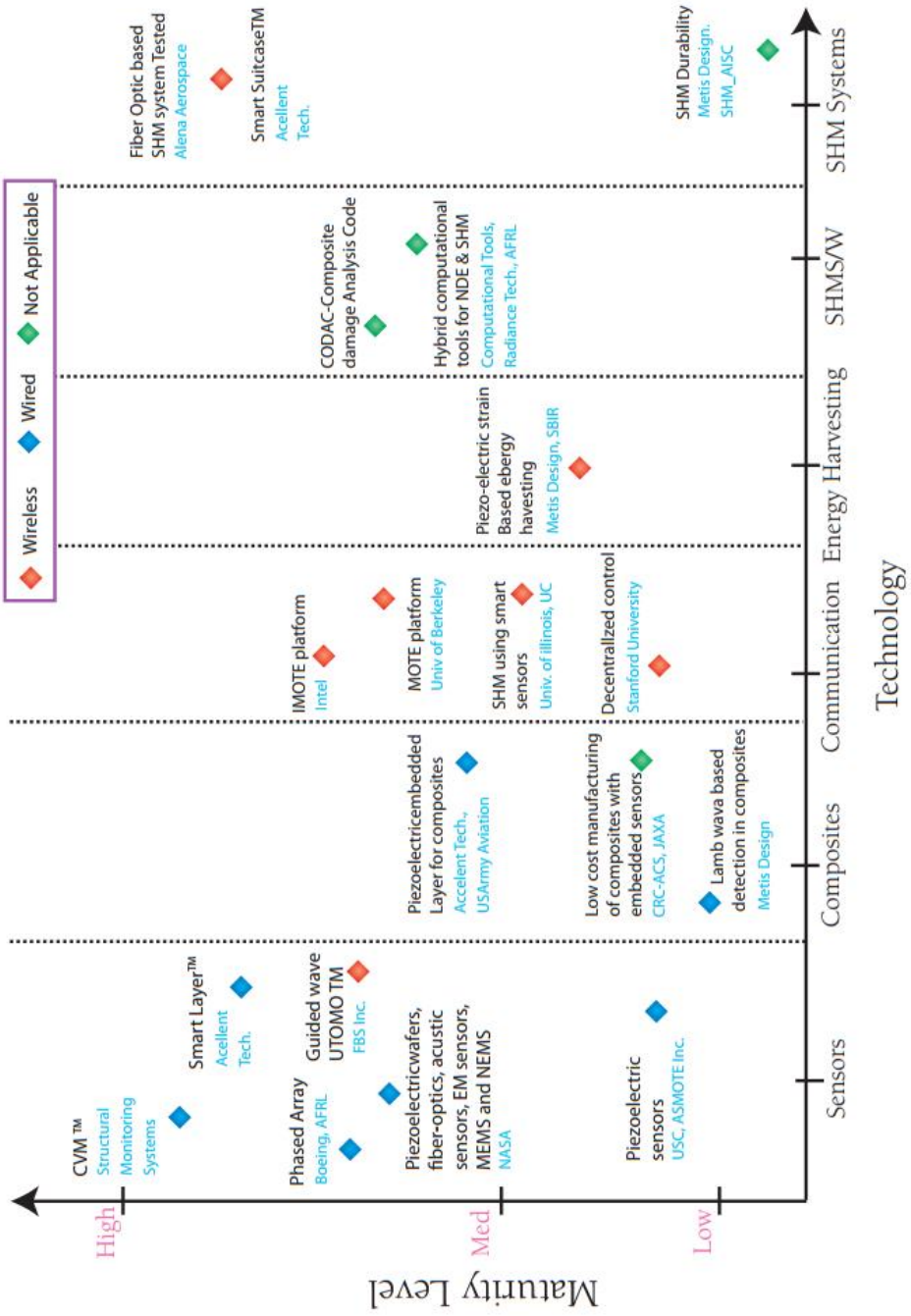

Figure 2. 28 Summary of various technologies of SHM systems (Aircraft SHM, Infosys 2012)

2.7 Chapter Conclusion

AASHM is one of the enabling technologies needed to revolutionise the future of aircraft design, development and maintenance. In this chapter, Energy storage was identified as an important aspect of the AASHM application, as energy harvesting is not possible throughout the flight cycle. During normal, cruising flight, the delta T between the fuselage and the primary insulation of the aircraft structure is reduced, So, any harvested energy during the takeoff and landing period must be stored efficiently.

A scenario is defined in this chapter, to support the fact that energy storage is a crucial part of AASHM application for a short-haul flight cycle of 80 minutes. In this scenario, the aircraft structure near the cargo door will be monitored using a wireless strain sensor powered by thermoelectric energy harvesting, located near the same location on the aircraft. The area around the cargo door will be monitored after the landing for 60 minutes and 60 minutes before the takeoff.

The temperature difference between the fuselage area around the cargo door, and the primary insulation is assumed to vary between -20^{o}C to +20^{o}C, but it should be noted that the temperature can vary over wider ranges, between -40^{o}C to +40^{o}C at other aircraft locations. So, the electronics on power management board and energy storage elements must operate within this temperature range.

A thermoelectric generator (TEG) output profile based on the output profile of a single Marlow industries TG 12-6-01L, was emulated using the N6705B DC power analyser. From a previous study based on a temperature difference of -20^{o}C to +20^{o}C, Marlow industries TEG TG 12-6-01L -D571 was able to deliver 31mW maximum output power into a 1.4 Ω fixed load resistance.

To achieve a similar scenario and a maximum output power for 1.3 Ω resistor was added in series to the generated output voltage. A pulsed-load was generated to represent the lowest power consumption mode *node-idle* (t_o) of 4.95 s and a current demand of 0.07 mA and highest power consumption mode, *transmission*, with a duration (t_1) of 50 ms and a current demand of 14.95 mA.

LTC 3109 was used as a DC-DC converter for the power management element. The batteries and supercapacitor will be charged using LTC 3109 over a temperature range of -40^{o}C to +40^{o}C. The charged batteries and supercapacitor will be discharged using the pulse load representing the *node-idle* and *transmission* states in the same temperature range. As stated, the temperature between the primary insulation and inner skin of the aircraft structure can be expected to change rapidly over the short-haul flight duration of 80 minutes. To show some representation of a longer period of operation associated with long-haul flights, over 13 hours, the discharging experiments were also conducted over 80 minutes cycles.

3. Power Management

Autonomous devices that are self-powered over their lifetime, extracting energy from the environment, are crucial for many applications. In such devices and applications, as the energy availability and power dissipation are not constant over time, effective energy management becomes a vital function and determines their information processing potential (Belleville and Condemine 2012). Moreover, average power and energy consumption of the power management system is required to be low. These challenging constraints have to be taken into account when developing an autonomous system. There are several duties the power management is responsible for in the context of energy harvesting power supplies. As shown in Figure 3.1 the first task is matching the energy transducer's voltage level with those of the electronic circuit or system which is being supplied. The next function is the regulation of the supply voltage, which must remain constant and independent of source or load variations. Then the harvested energy must be stored efficiently in a rechargeable battery or supercapacitor. The final task is the management of the energy stored in the supercapacitors or rechargeable batteries.

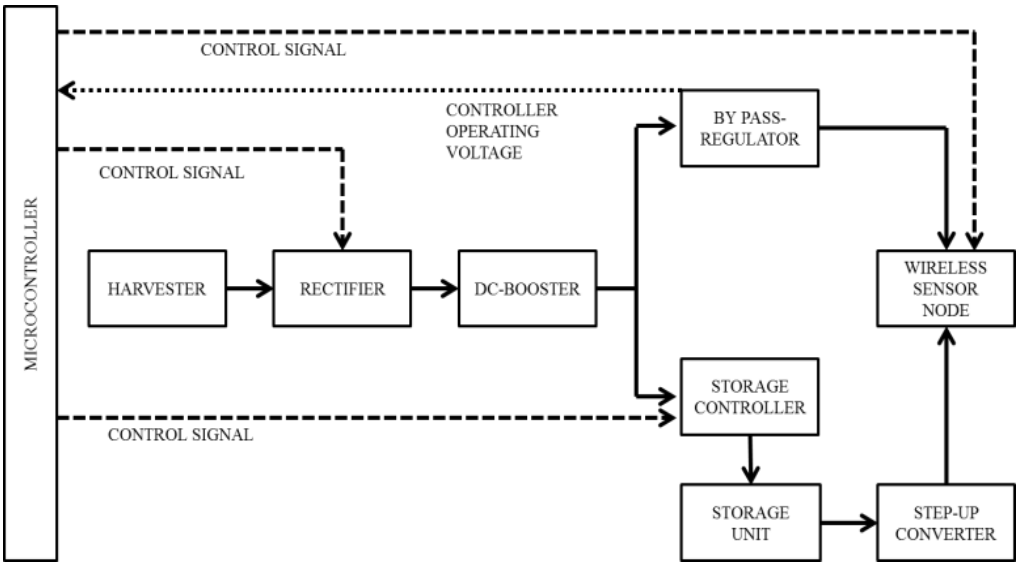

Figure 3. 1 Typical power management system - block diagram

A power management system for energy harvesting must efficiently extract and store power from the harvester and transfer this to the load. These three functions are carried out by the components listed below:

- A DC-DC Converter
- A storage controller (explained in chapter 4)
- A microcontroller
- An Output Step converter

This chapter discusses the requirements of an efficient power management system for thermoelectric energy harvesting. Thermoelectric energy harvesting in aircraft is explained in Chapter 2. To understand the theory of DC-DC conversion four types of DC-DC converters are explained in terms of their working principles and Characterisation of an LTC3109 commercially available DC booster suitable for thermoelectric energy harvesting is discussed.

3.1 Overview of DC-DC converters

The most frequently used topologies for DC/DC switching converters are

- Boost converter – output voltage is always greater than input voltage;
- Buck converter – output voltage is lower than input voltage;
- Buck-boost converter – output voltage can be either higher or lower than input voltage;
- Flyback converter – isolated buck-boost converter with a transformer at the input;

These converters operate in two modes; a continuous mode where the current through the inductor never falls to zero during the cycle, and a discontinuous mode where the current through the inductor falls to zero during the cycle.

A brief overview of four converters is explained below(Rashid 2010).

3.1.1 Boost Converter

A typical boost converter is shown in Figure 3.2. It is the most important converter topology in energy harvesting as the harvested voltage levels are usually quite low.

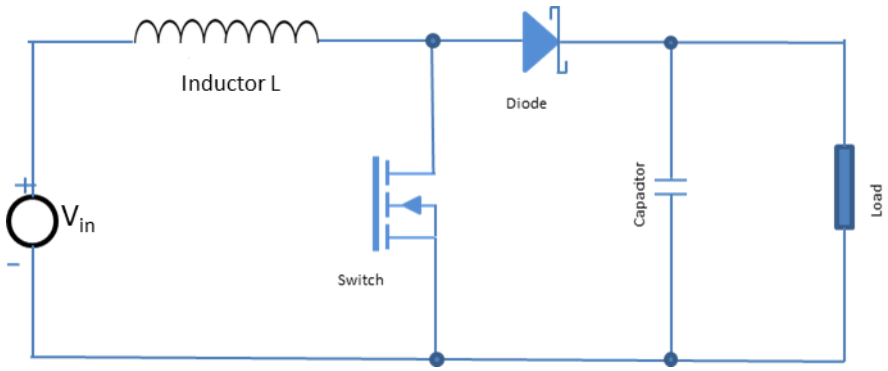

Figure 3. 2 Boost converter(Rashid 2010)

The source voltage V_{in} is presented across the inductor when the transistor switch conducts, and the inductor current increases at a rate equal to V_{in}/L. When the switch opens, the instantaneous change in current causes the magnetic field to collapse and a back-EMF to develop across the inductor which appears in series with the source voltage, forward biasing the diode and charging the capacitor. Because of this action, the voltage developed across the load will always be larger than the supply voltage.

3.1.2 Buck Converter

A typical example of a simple buck converter is shown in Figure 3.3. The output voltage of a buck converter is always lower than the input.

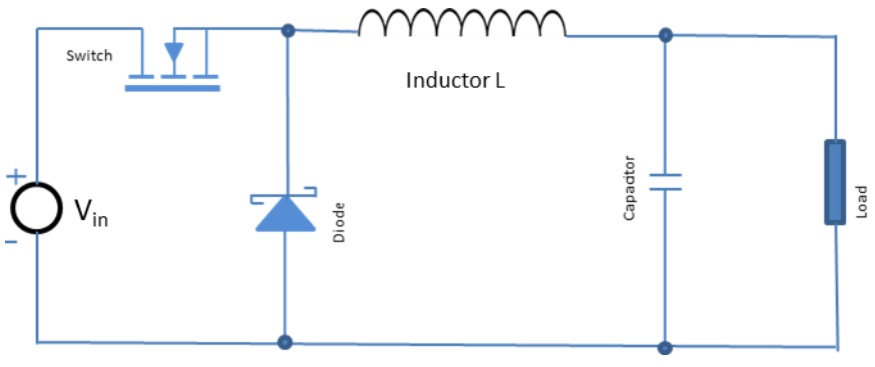

Figure 3. 3 Buck converter(Rashid 2010)

When the transistor switches on, the inductor current increases at a rate equal to $(V_{in} - V_{out})/L$. During this condition, the diode D in the buck converter will be reverse biased and will not conduct, and current will flow from the supply into the load and will charge the capacitor. At some time later, when the transistor switches off, the back EMF developed across the inductor causes the diode to conduct, allowing current to be released from the inductor into the load, decreasing at a rate of $-V_{out}/L$. The overall effect is a reduced output voltage that is related to the input switching voltage by the duty cycle of the switching waveform.

3.1.3 Buck-Boost converter

Buck-boost converters offer good flexibility and as a result, are widely used and implemented in many commercial integrated circuits for energy harvesting. A typical example is given in Figure 3.4.

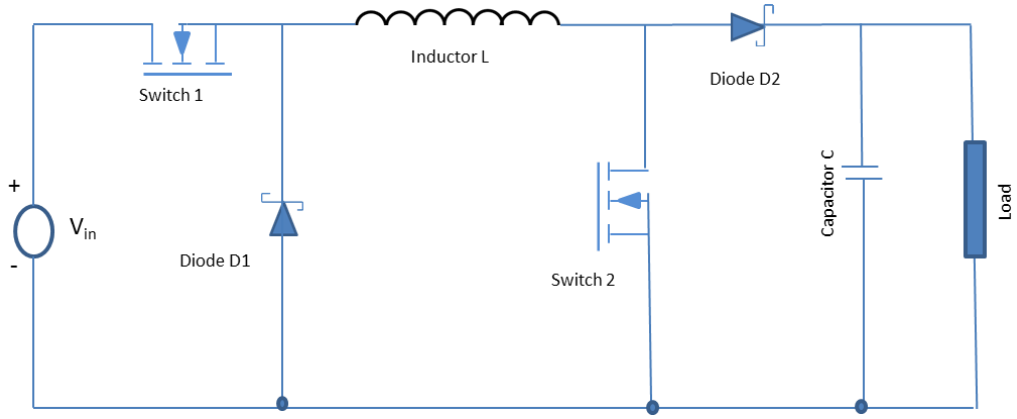

Figure 3. 4 Buck-Boost converter(Rashid 2010)

Operation in boost mode - switch 1 is turned off, and switch 2 is switched on and off by a high-frequency square wave. When switch-1 conducts, current flows through the inductor and the diode, charging C and supplying voltage to the load. In this state, diode D1 is in reverse bias. When switch 1 turns off, current initially flows from the inductor L. The back EMF established turns on D1, and current then flows through D2 and the load. As the stored inductive current decreases, the charge accumulated in C now also adds to the current flowing through the load, keeping VOUT reasonably constant.

Operation in buck mode - switch 1 is continually on, and a switching waveform is applied to switch 2. During the on periods when switch 2 is conducting, the input current flows through the inductor and via switch 2, directly back to the supply negative terminal charging up the

inductor, while D2 is reverse biased. During this phase, the load is being supplied entirely by the charge on the capacitor.

3.1.4 Flyback Converter

A flyback converter can provide output voltages which are much higher than the supplied input voltages. Typical applications lie for example in power management for thermoelectric generators operating with very low-temperature differences. The control electronics of commercially available flyback converters are usually supplied separately using charge pumps which allow these very low start-up voltages.

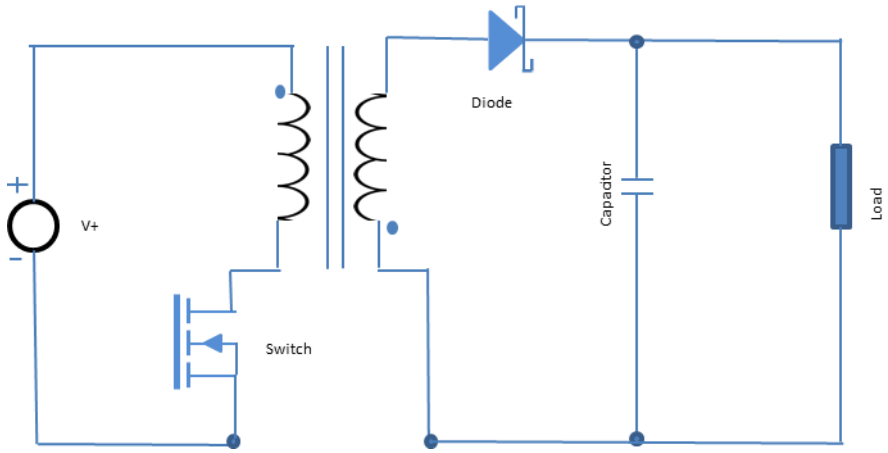

Figure 3. 5 Flyback converter(Rashid 2010)

A typical operating scheme is shown in Figure 3.5.

Switch in ON State - The primary coil of the transformer is connected to the input supply, with the dotted end connected to the positive terminal of the input supply and the diode D is arranged in reverse bias state. No energy is transferred to the load, and the energy is stored in the primary coil

Switch in OFF state - The voltage polarity across the coils is reversed causing the diode D to become forward biased. The energy stored in the primary coil is transferred to the load.

3.2 DC-DC Converter for energy harvesting

The three standard working principle of switching regulators are

- Step-up (increase)
- Step-down (decrease)
- Step up or step down (increase or decrease)

A convention ratio (M)is defined as the ratio of output voltage V_{out} to the input voltage V_{in} and depends on the switching waveform duty cycle (D). Pulse width modulation or pulse frequency modulation (PFM) is usually used to control the duty cycle.

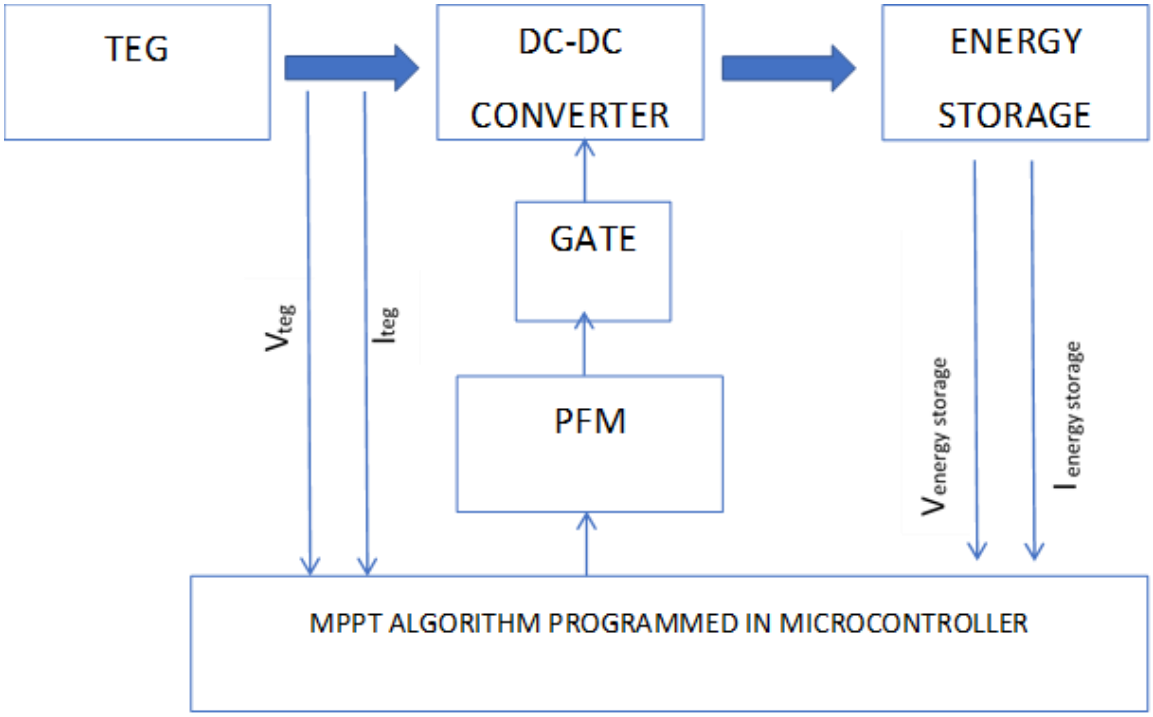

Figure 3. 6 Overview of dc-dc converter with MPPT for energy harvesting

Boost converter and Buck-Boost converter are commonly used topologies, and PFM is preferred as the power consumption is low and more suitable for low power load applications (Kazimierczuk 2015) . As shown in Figure 3.6 a microcontroller typically produces the PFM signal (Elfisiniotis 2013) with maximum power point tracking algorithm (MPPT) ensuring efficient operation.

3.3 Maximum Power Point Tracking (MPPT)

The critical problem for load matching is the lack of direct measurement of internal resistance R_{TEM} during operation. To maintain maximum power transfer, therefore, various tracking methods can be employed. MPPT for thermoelectric applications is based on established photovoltaic solutions (De Brito, Galotto et al. 2013). The most common methods used in conjunction with TEGs are Perturb and Observe (P&O) and Fractional Open-Circuit Voltage (FOCV). The FOCV method involves periodically disconnecting the TEM from the converter. Consequently, an open-circuit voltage on the terminals of the TEM is measured. FOCV is based on the observation that MPP voltage can be obtained as a fraction of open circuit voltage:

$$U_{Mpp}(U_{oc}) = kU_{oc} \quad (3.1)$$

Where U_{Mpp} is the output voltage at maximum output power and U_{oc} is the open circuit voltage at the output terminal Typically, k = 0.5 is used for most of TEG applications. The duty cycle is then set to maintain the input voltage which ensures maximum power transfer.

The first step in applying any MPPT is to measure the values of input current and voltage which are entered into any algorithm. The next step is to compute the exact power on the input terminals of the DC/DC converter. The P&O method requires the duty cycle to be changed based on the measurement of voltage and current on the input terminals of a switching converter (Vadstrup, Schaltz et al. 2013)A flowchart of the algorithm is provided in Figure 3.7 in the first step it calculates the power by measuring the voltage and current. On the second step, up it compares the present power value with previous value. Then the algorithm increases or decreases the voltage value V_{ref} to obtain the maximum power. This process repeated until the maximum power is achieved and the operating point around the maximum power point. The most significant disadvantage of this method is the oscillations around the MPP, and the system is not unconditionally stable(Park and Kim 2012).

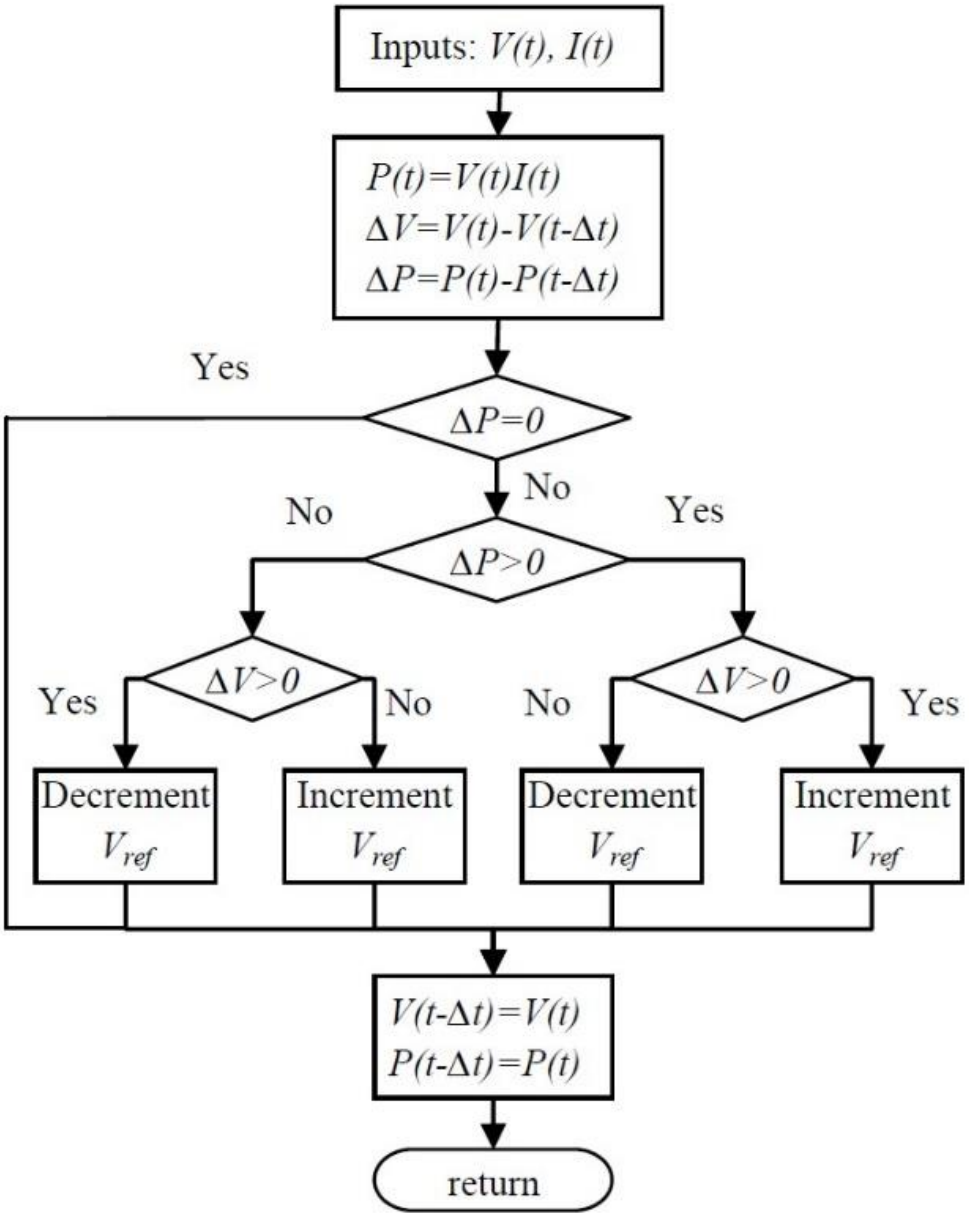

Figure 3.7 Flowchart of P&O algorithm (Vadstrup 2013)

3.4 Commercially available DC-DC boosters

A few the commercially available DC-DC boosters suitable for thermoelectric energy harvesting and these are briefly explained below. Their advantages and disadvantages are discussed along with measurement of their open circuit start-up voltage and the influence temperature of the open circuit output voltage.

3.4.1 Linear Technology 3109

A thermoelectric Peltier Cell is connected to Linear Technology's LTC3109 step-up converter as shown in Figure 3.8. The LTC3019 "is designed to manage the charging and regulation of multiple outputs in a system in which the average power draw is 'shallow', but where periodic pulses of higher load current may be required"(2010). This is typical of wireless sensor node (WSN) behaviour, where the quiescent power consumption is typically very low for the majority of the time, but periodically becomes high during transmission.

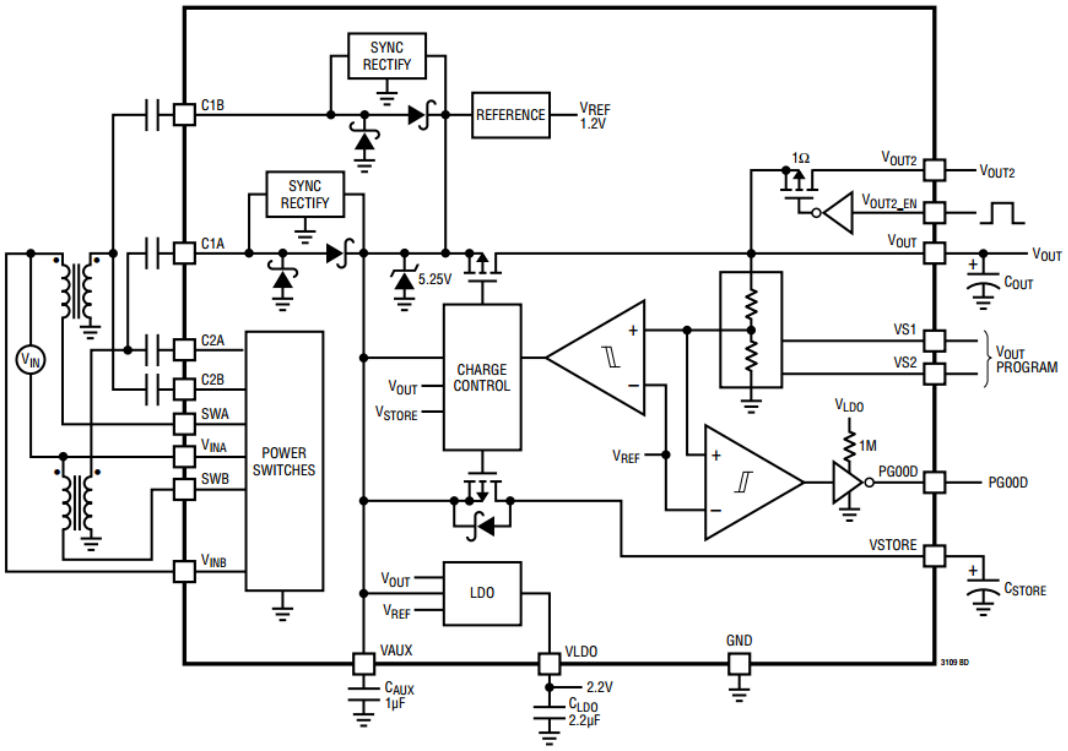

Figure 3. 8 LTC3109 Internal Schematic (LTC3109, Datasheet)

The LTC3019 can operate from voltages as low as 30 mV, due to the resonant step-up oscillator formed by the internal MOSFET switches and external step-up transformers, and with an oscillating frequency determined by the inductance of the secondary winding of the transformer. The AC voltage produced by the secondary winding of the transformer is boosted by external charge pump capacitors and rectified internally to the LTC3109.

All active circuits within the LTC3109 are powered from the V_{AUX} pin; V_{OUT} charges when the voltage across V_{AUX} is greater than 2.5V. The maximum voltage on V_{AUX} is limited to 5.25 V by an internal shunt linear dropout (LDO) regulator, which shunts any excess current in V_{AUX} to

ground when there is no load on the converter. Once V_{AUX} exceeds 2V, synchronous rectifiers in parallel with the internal rectifier diodes rectify the input voltage at the C1A and C1B pins.

The output voltage V_{OUT} is programmable by configuring the VS1 and VS2 pins in a particular order and may be set to be 2.35V, 3.3V, 4.1V, and 5V. The internal resistor divider, controlled by VS1 and VS2, eliminates the need for very high-value external resistors, which are susceptible to noise pickup and leakage as shown in Figure 3.9

V_{STORE} can be used to charge a supercapacitor or rechargeable battery. Since the output current is limited to 15mA, V_{STORE} can be used to trickle charge NiCd or NiMH batteries. However, V_{STORE} is not intended to supply high pulse load currents to V_{OUT}. Instead, this must be handled by a large reservoir capacitor at V_{OUT}.

The LTC3109 contains a P_{GOOD} signal which can be used to wake a sleeping microcontroller.

The capacitors at the inputs of pins C1A and C2A facilitate the use of the internal charge pump rectifier in the LTC3109 and store charge to be later boosted, allowing the device to operate from a very low voltage (30 mV). With a 1:100 turns ratio on the input transformers, allowing an input voltage of 25 mV, a low-value pump capacitor (1 nF) allows for this ultra-low input voltage and low source resistance

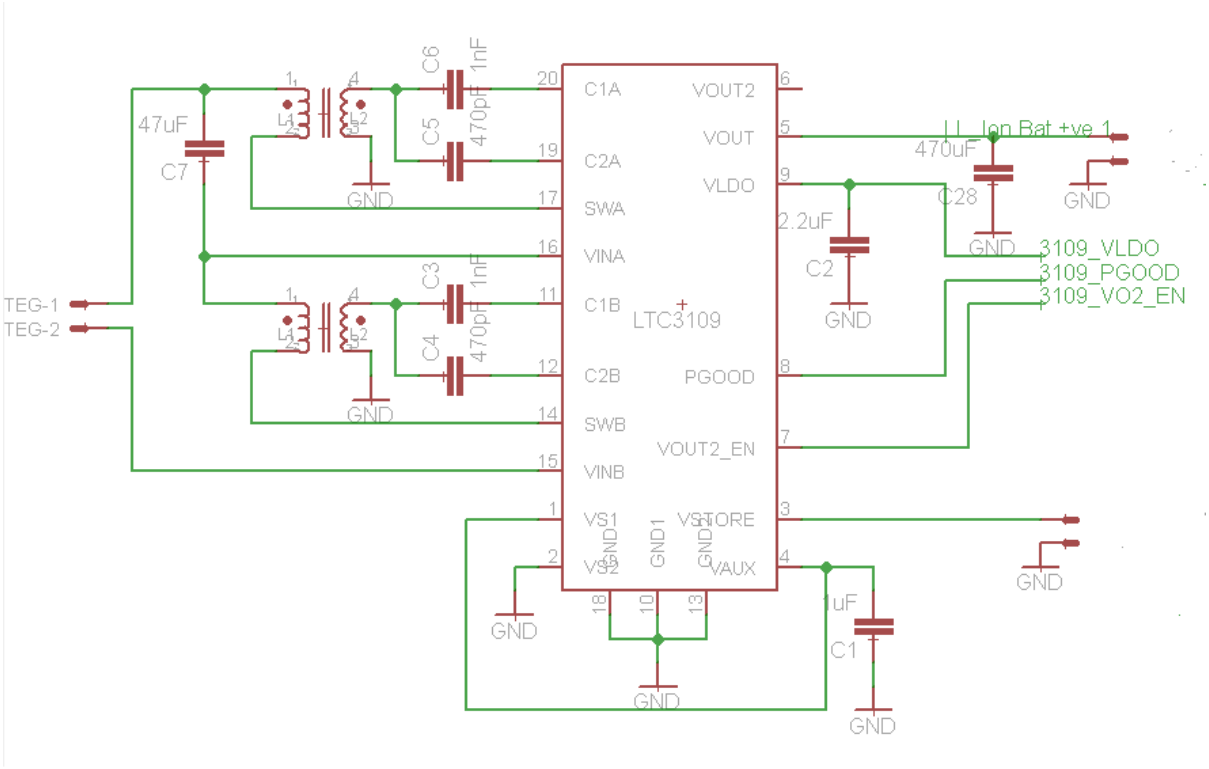

Figure 3. 9 TEG DC/DC Converter Circuit

.

The capacitors on the C2A and C2B pins connect the LTC3109 to the secondary windings of the step-up transformers. A very low capacitance value of 470 pF allows for a low start-up voltage and high efficiency. A lower capacitance value has the effect of allowing the start-up voltage, and a higher capacitance value has the effect of reducing efficiency.

The capacitor at the output of the LTC3109 is sized to provide the necessary current when the load is pulsed on. This capacitor's value is dictated by the load current (i_{load}), the duration of the load pulse (t_{pulse}), and the amount of voltage drop in the output (ΔV_{out}) according to:

$$C_{out(\mu F)} = \frac{i_{load(mA)} \cdot t_{pulse(ms)}}{\Delta V_{out(V)}} \qquad (3.2)$$

3.5 Characterisation of commercially available DC-DC converters (energy harvesting)

Several possible DC/DC converters for the thermoelectric energy harvesting is identified and characterised according to the datasheets, in order to understand their applicability to the design; the Linear Technology devices LTC3109, LTC3108, LTC3558, LTC3459, and LTC3105, and the Texas Instruments BQ25504. Some of the key figures of merit for these devices were the start-up times of the devices, i.e. the time taken to reach a steady-state value in response to a step input, the minimum startup voltage, the maximum operating voltage, and the device efficiency.

3.5.1 Start-up Voltage

The start-up voltages of the DC/DC converters quantify the minimum input voltage required for a voltage to occur at the output. The start-up voltages are given in the device data sheets but were confirmed through measurement. The results are displayed in Table 3.1.

Table 3.1 Device Start-Up Times Expected and Measured Values

Device	Expected Start-Up Voltage (V)	Measured Start-Up Voltage (V)
LTC3109	±0.03	±0.03
LTC3108	0.02	0.05
TI BQ25504	0.25	0..38
LTC3558	3.1	4.28
LTC3459	1.5	0.9
LTC3105	0.225	0..425

3.5.2 Maximum Input Voltage

The maximum input voltage allows for the quantification of the input voltage range when the start-up voltage is known. It is a prominent figure of merit, as it allows the designer to understand the appropriateness of a converter for a given source. The maximum input voltages taken from the respective datasheets of the devices are given in Table 3.2

Table 3.2 Device Maximum Input Voltages

Device	Maximum Input Voltage (V)
LTC3109	±0.5
LTC3108	0.5
TI BQ25504	5.4
LTC3558	17
LTC3459	5.2
LTC3105	5

3.5.3 Experimental Setup

The LTC3109 has been used in this thesis as a power management board because of its dual polarity input capability and suitability for TEG applications. LTC3109 demonstration board was used for the experiments and the TEG output profile created in chapter 2.6.2 is given as input using N6705B, and the output from V_{out} and V_{store} pins is data logged using a Nidaq6211 data acquisition module, as shown in Figure 3.10. As the aircraft application is temperature dependent, the DC-DC converters need to operate at least from -40^{o}C to +40^{o}C. LTC 3109 was placed in the climatic chamber.

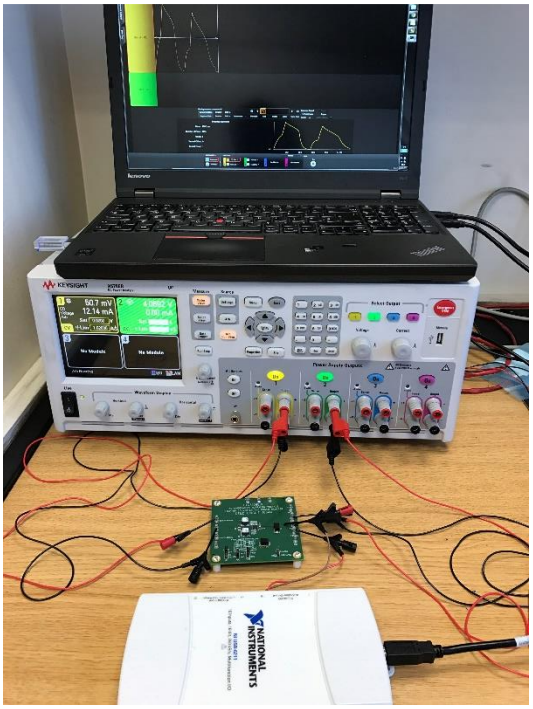

Figure 3.10 LTC3109 Vstore and Vout measurement setup

LabVIEW code was written to record two analogue inputs to ai0 and ai1 pins of Nidaq 6211 as shown in Figure 3.11. The code generates an array of two columns with analogue values from ai0 and ai1 pins and writes it in Excel format on the user-defined system location. The sampling rate can be adjusted by creating time delay for the loop execution.

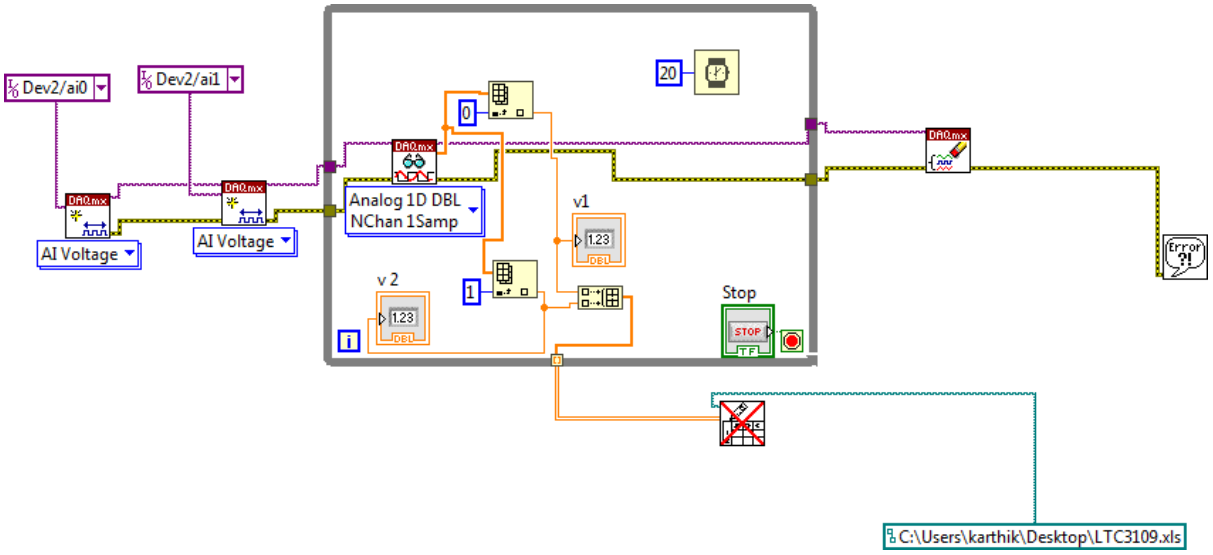

Figure 3. 11 LabVIEW coding for TEG Vout and Vstore data logging

Figure 3. 12 Climatic chamber set up for LTC3109 Vout and Vstore measurement and tested on a temperature range of -40°C to +40°C

3.5.4 Result Analysis

The LTC3109 has 3 output pins, V_{store}, V_{out} and V_{out2}. The V_{out} and V_{store} have commonly used as a pin for powering microcontrollers and energy storage. The V_{out} is charged from VAUX pin and is user-programmed to one of four regulated voltages using select pins VS1 and VS2, according to Table 3.3. The open circuit voltage at V_{out} and V_{store} pins were connected ai0 and ai1 to Nidaq 6211 respectively. The experiment was carried with the climatic chamber for a temperature range of -40°C to +40°C.

Table 3.3 LTC3109 Vout output configuration

VS2	VS1	V_{out}
GND	GND	2.35V
GND	VAUX	3.3V
VAUX	GND	4.1V
VAUX	VAUX	5V

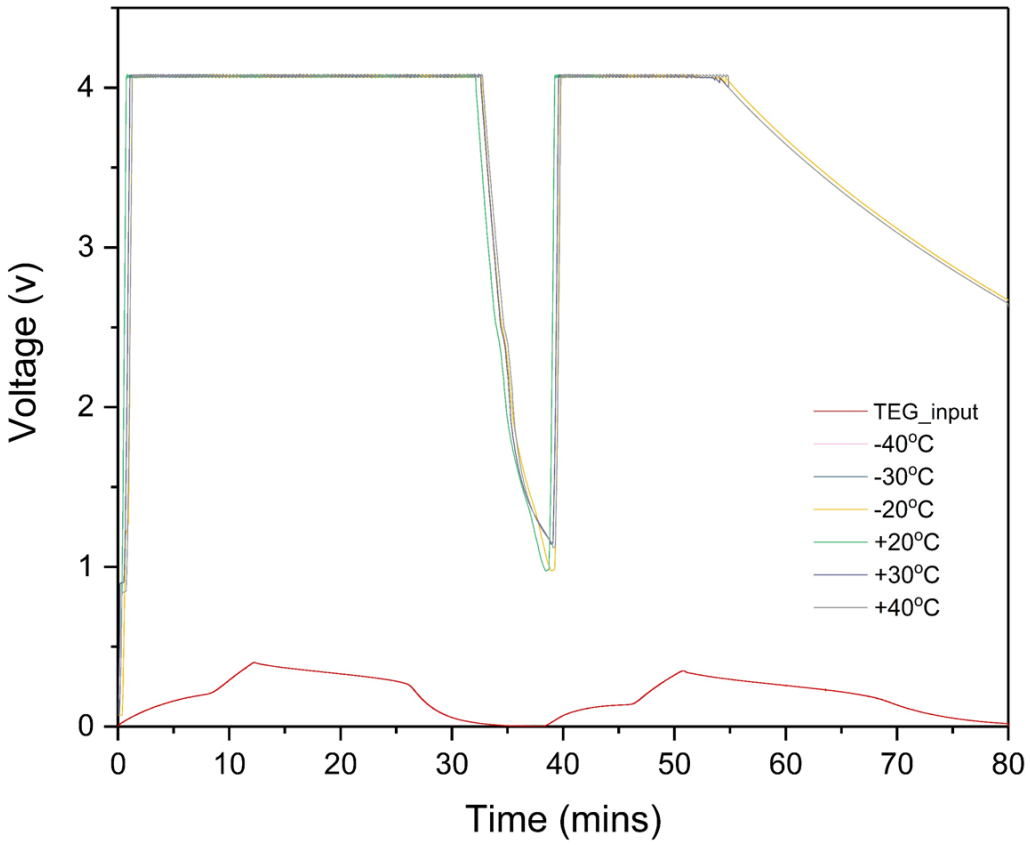

Figure 3.13 LTC3109 V_{out} for the generated TEG output profile on a temperature range of -40°C to +40°C

As shown in Figure 3.13 & 3.14, The output from the V_{out} and V_{store} reaches it is the peak value of 4.1 V and 5.2 V as the input voltage to LTC 3109 demonstrator board increases, as the input voltage decreases the output voltage from the V_{out} and V_{store} pins also decreases simultaneously.

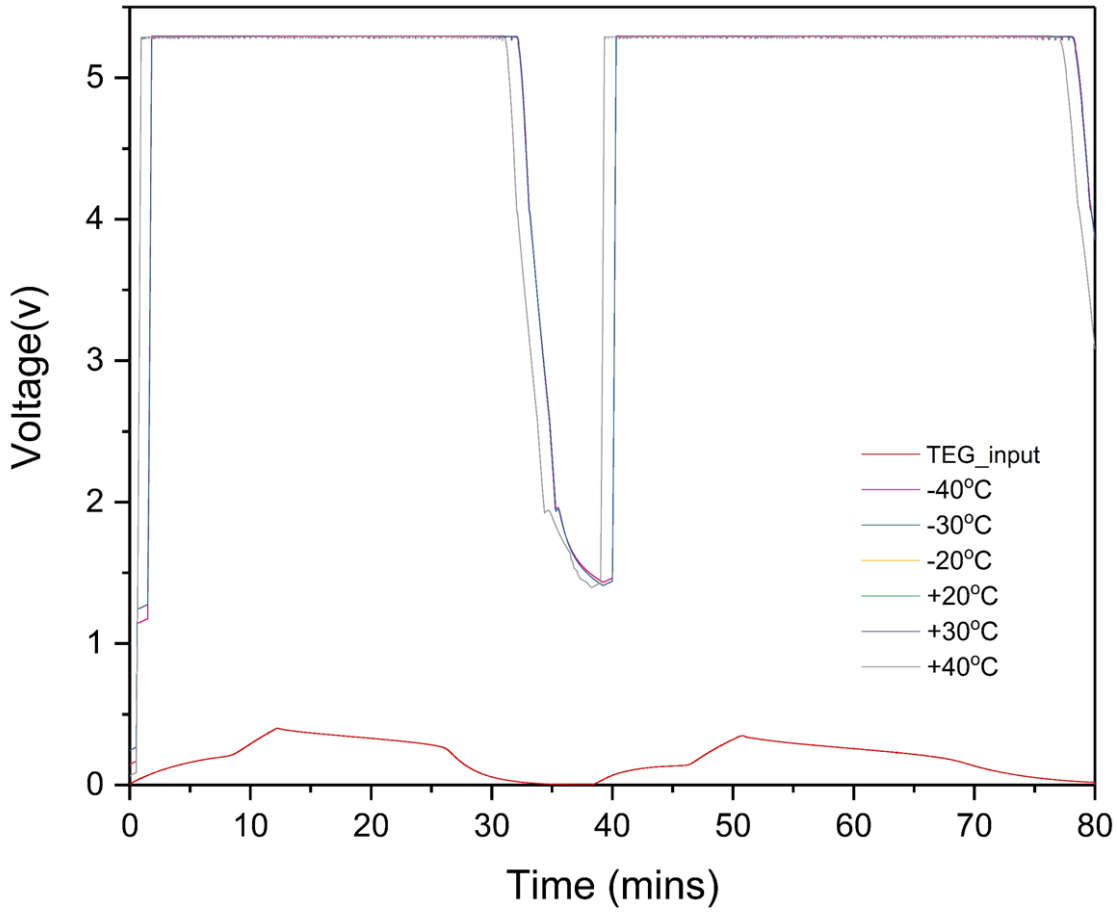

Figure 3. 14 LTC3109 V_{store} for the generated TEG output profile on a temperature range of -40°C to +40°C

The results show that LTC3109 is relatively unaffected by temperature. However, a detailed study must be conducted to measure the energy conversion loss in terms of switching loss, heat loss in the LTC3109.

3.6 Output Step-Up Converter

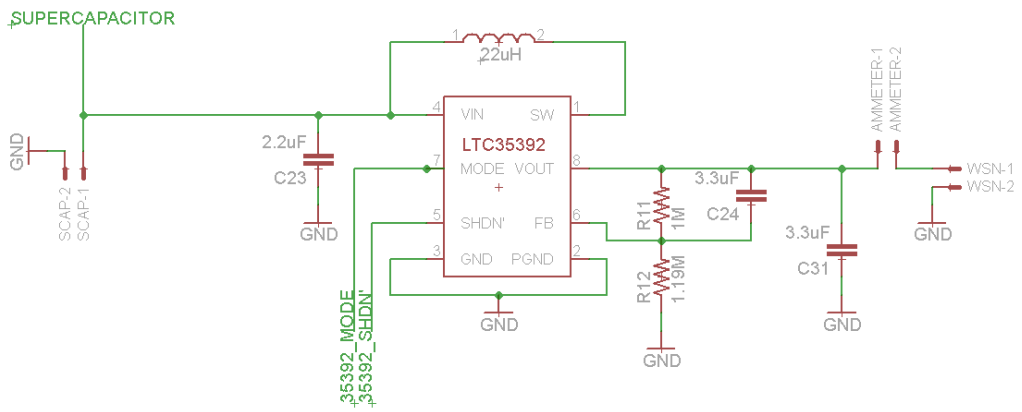

Figure 3. 15 Schematic of LTC 3539

AASHM WSN requires a constant input supply up to either 3.3 V or 5 V, and before being applied to the WSN load, the WSN circuit input voltage must be stepped up to a 3.3V or 5 V level via the step-up converter. The LTC35392 is a is a programmable synchronous step-up general-purpose DC/DC converter that operates between 0.8 -6V input voltages, and produces a 3.3 V or 5V output voltage, up to an efficiency of 94% (Linear Technology, 2008). With reference to Figure 3.16, the output voltage is set by the two resistors R11 and R12 by the formula:

$$V_{out} = V_{Ref}(1 + \frac{R_{11}}{R_{12}}) \quad (3.3)$$

With VREF=1.2V (Linear Technology, 2008), and assuming R11 to equal 1MΩ, a 5V output voltage is obtained from the resistor divider network with R12 obtained by:

$$R_{12} = \frac{1.2M\Omega}{3.8} = 315K\Omega = 309K\Omega \quad (3.4)$$

The inductor between SW and VIN is needed in the event that burst mode operation is desired. In this case, the load current at which burst mode operation entered can be adjusted by the inductor. A decoupling capacitor at the input reduces interference due to input switching noise. A typical value of 2.2µF is chosen. In addition, a decoupling capacitor at the output reduces the output current draw.

3.6.1 Result Analysis

To experimental verify the operating temperature of LTC3539, a 0.5F, 4V Supercapacitor storage element was used as an input to LTC3539 and the power consumption characteristic of the WSN based strain sensors, as identified in chapter 2.6, was used to provide a representative pulsed-load. The N6705B was used to generate the pulsed-load and to data log the output from LTC3539. The climatic chamber was used to create a temperature range of -40°C to +40°C

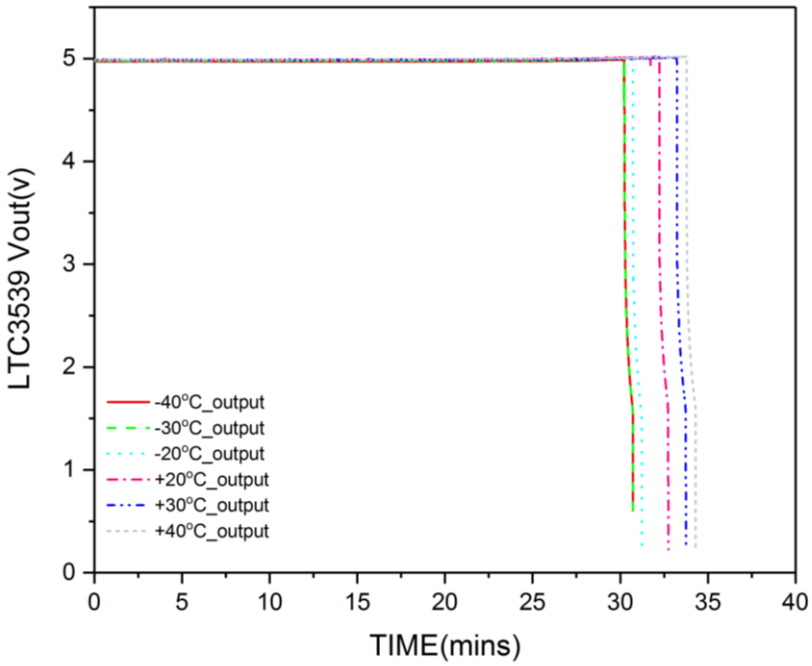

Figure 3. 16 Voltage output from LTC 3539 under pulsed-load condition in a temperature range of -40°C to +40°C

Inside the climatic chamber, LTC3539 and a supercapacitor were placed, channel 1 of N6705B acts as the pulse load, and the output from LTC 3539 is recorded in the channel 2 of N6705B. From the results shown in Figure 3.16, it can be seen that LTC3539 is relatively unaffected by temperature. The output voltage from LTC 3539 reduces to 0 V however when the supercapacitor voltage reaches 0.8 V. At +40 and -40°C; this happens at 35 minutes and 30 minutes respectively. This is due to the temperature influence on supercapacitor or the LTC 3539, or both. The discharge properties of supercapacitor based on the temperature are discussed in chapter 4.5. However, a further detailed study has to be conducted to measure the energy conversion losses and also the effect of temperature on the LTC3539.

3.7 Chapter Conclusion

Although WSNs have been increasingly developed over the past few years, one of the remaining challenges is the impact of the dynamic power requirements on the power management system. LTC 3109 is a dual polarity, low start-up voltage DC-DC booster, but it does not have an MPPT inbuilt like BQ25504 from Texas instrument. The BQ25504 is not a dual polarity input, and external rectifier circuit is required. LTC 3109 operates well within the temperature range of -40^{o}C to +40^{o}C. LTC 3539 is output step converter used in the power management. Any typical WSN needs a constant input supply up to 3.3 v or 5 V; this can be achieved by powering a WSN through step converter from supercapacitor. LTC 3539 steps converter with up to 94 % efficiency, with a minimum input value of 0.8 V and is well operated in the temperature range of -40^{o}C to +40^{o}C. However more experimental analysis is needed to understand the energy conversion loss in both.

As the power requirements change over time due to the changing functionality of the WSN, the requirements of the power management system also change. Voltage levels and sensitivity have to scale-down, and current consumption must be decreased to assure performance with the small amounts of energy available from the environment. A degree of intelligence to adapt to different operational modes is required to maintain minimum power consumption and so self-powered operation by energy harvesting transducers. Due to these small amounts of energy being processed, the power consumption of blocks like step-up converters or regulators has to be minimised, to arrive at an acceptable efficiency.

4. Energy Storage Options for Aircraft SHM System

An energy storage device is generally required to store the energy when it is available and supply power to an application when needed (Winter and Brodd 2004). Most ambient energy-harvesting systems are not a constant power supply and produce deficient power at highly variable voltage levels. Energy storage devices can provide an “immediate power” capability, eliminating the need for a system to wait for the required energy to become available before it can operate. Batteries and supercapacitors have so far been used as the primary solution for powering wireless sensor nodes (WSN) for various applications (Mathuna, O’Donnell et al. 2008). Depending on the application, storage elements have some distinct disadvantages. However, precisely their size, cost, need for maintenance and the cost of replacement. Influence of environment temperature on storage units must be evaluated carefully. Energy harvesting sources cannot provide constant power for charging and this can be problematic for energy storage units (Schalkwijk and Scrosati 2002). In addition, storage units should have low leakage current as energy harvesting in aircraft may be not available when the aircraft is grounded .

As shown in Figure 4.1 energy storage device with high-energy and power density are required along with energy harvesting system to enable autonomously powered embedded electronic systems. Even though there are many choices of storage elements, the aircraft SHM demands energy storage with high cycle-life, operating temperature in a range of at there has least -40^{o}C to +40^{o}C and with low resistance, leakage current.

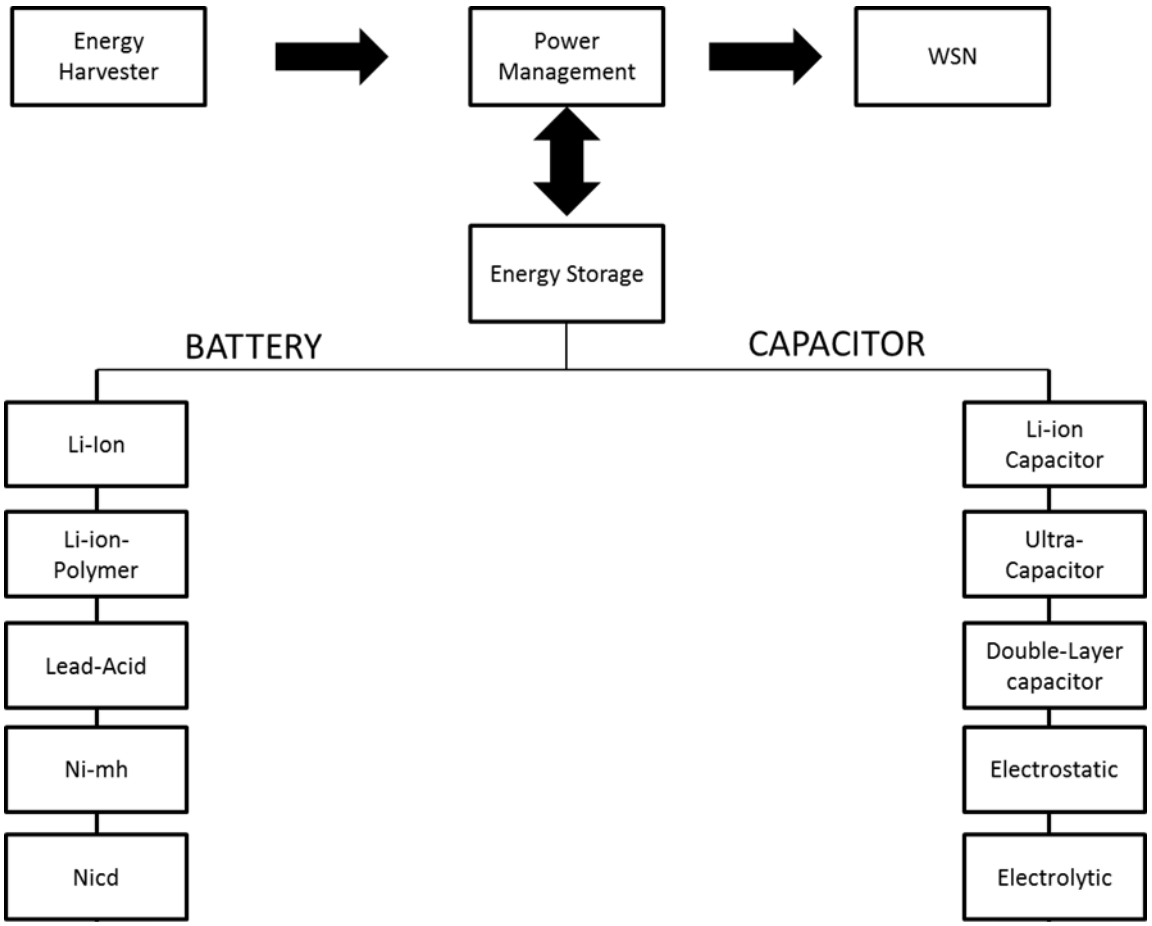

Figure 4. 1 Available storage elements

In order to deliver the power and energy demands of the WSN, an energy storage device combining high power and high-energy density is required. A Comparison of different storage elements on the basis of energy and power density is shown in Figure 4.2. Battery only solutions, due to their relatively high equivalent series resistance (ESR) and limited power density, can struggle to deliver the required current and voltage simultaneously. In addition to this, the fact that *whilst at room temperature, batteries work perfectly well, but at lower temperatures, the internal resistance increases leading to reduced capacity* is verified with experimental Characterisation and explained below. This disadvantage has led to the development of supercapacitors as an alternative storage approach, however, although their power density is much higher, their energy density is 10%-20% lower than that of a similar

physical size battery, so storage of large amounts of energy using supercapacitors will always be a constraint.

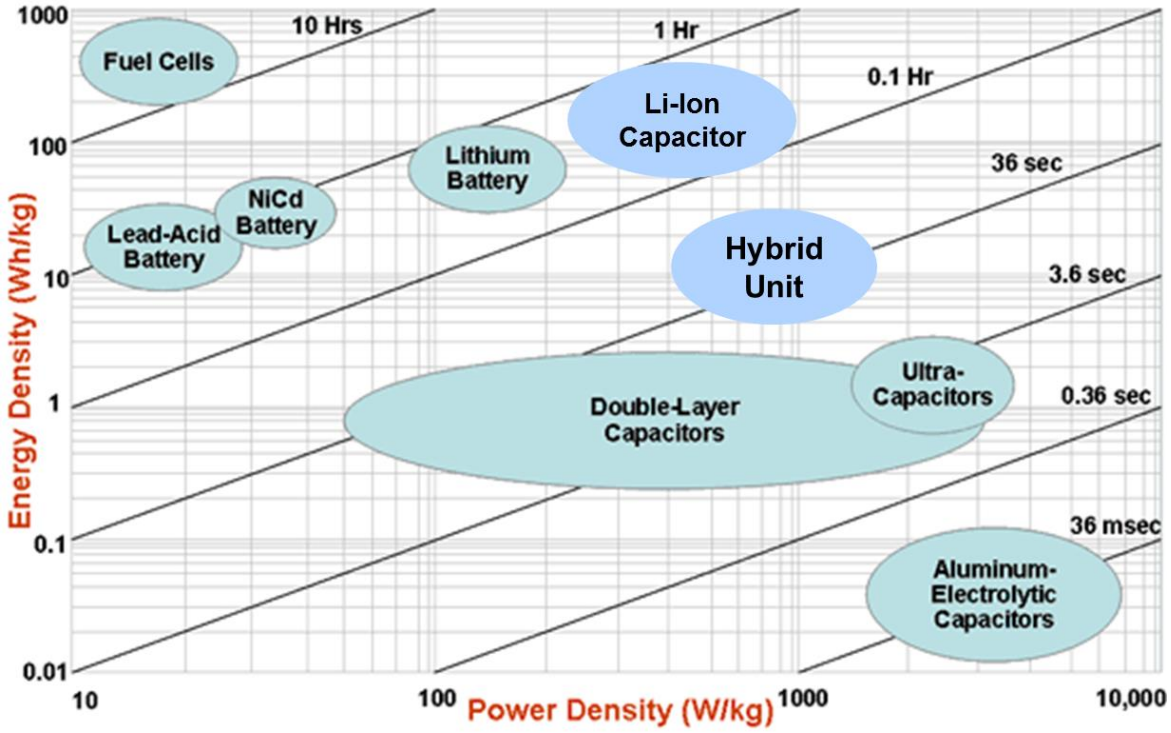

Figure 4. 2 Comparison of different storage elements on the basis of energy and power density (Maxwell Technologies marketing report)

The energy requirements of sensor nodes vary significantly, ranging for example from temperature sensors where the power demand is in the order of millijoules to acoustic-ultrasonic techniques requiring power levels up a number of Joules. The power consumption of the sensor node itself is also highly dynamic and varies depending upon its state at a particular time (*wake-up, sampling, switching, processing, protocol type, transmission or idle)*. During the *wake-up* state, for example, the sensor node demands significant current whilst also requiring a constant supply voltage.

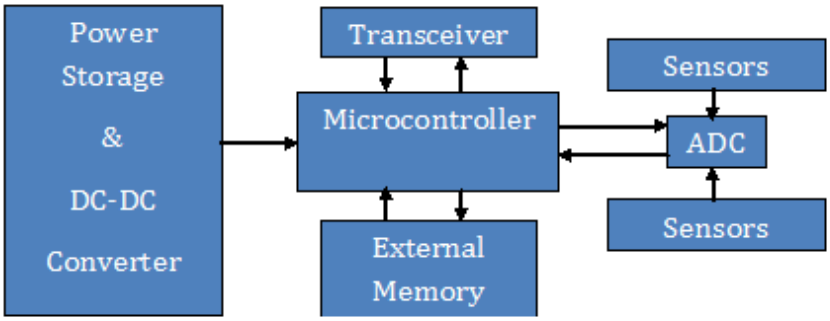

Figure 4. 3 Typical wireless sensor node architecture (Farooq 2011),

As the current demands of a node vary with function, it is crucial to develop an energy storage system that can compensate for these differences. A sensor node does not present a constant current load, instead of a pulsing load, with transient peak currents. The power storage system must be able to accommodate the transient peak currents that will be generated due to data transmission.

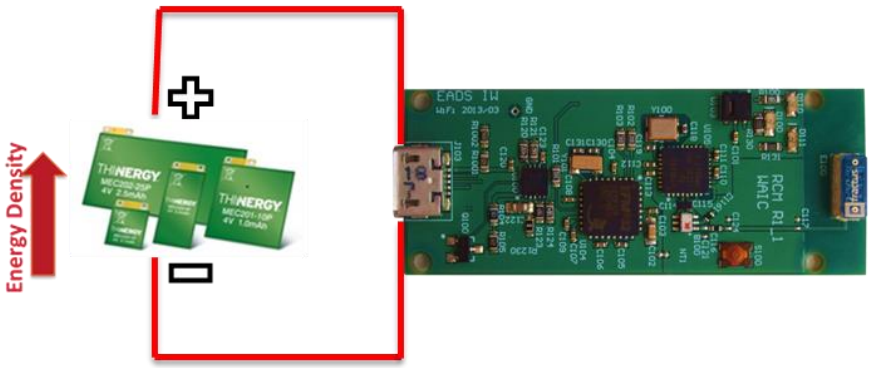

Figure 4. 4 Battery powered WSN – offers high energy density

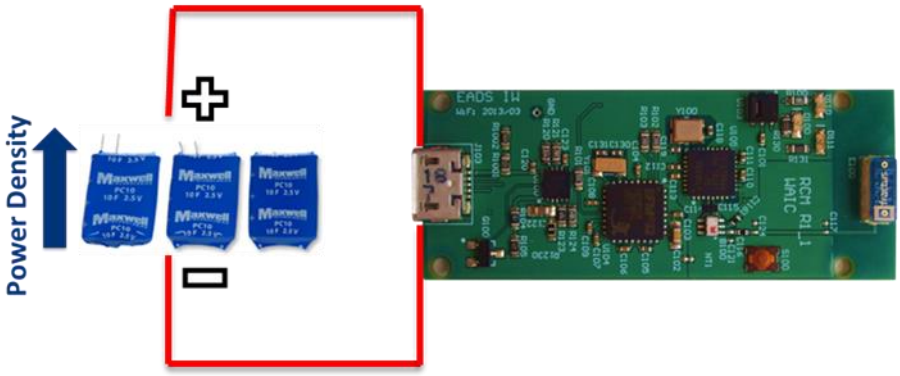

Figure 4. 5 Supercapacitor powered WSN – offers high power density

The highly dynamic power demands of a WSN need an energy storage unit that can accumulate sufficient energy for the required time of operation whilst being able to provide

instantaneous high current when required to accommodate, for example, the *transmission* state identified earlier in this thesis. Batteries and supercapacitors offer optimal storage characteristics for these two requirements respectively, as shown in Figure 4.4 and Figure 4.5.

4.1 Batteries

There are three essential factors that need to be considered when selecting a battery for the aircraft applications; operating temperature, cycle-life and weight.

4.1.1 Battery Specifications

I. State of Charge (SoC) %: SoC is generally calculated using current integration to determine the change in battery charge over time.

II. Depth of Discharge (DoD) %: The percentage of battery capacity that has been discharged. Discharge to at least 80% is referred to as a deep discharge.

III. Internal resistance: As internal resistance increases, the battery efficiency decreases, and thermal stability is reduced as more energy is converted into heat.

IV. Nominal Voltage: the Normal voltage of the battery, usually mentioned as operating voltage.

V. Energy (Wh): Energy is defined as the multiplication of discharge power (Watts) by the discharge time (hours).

VI. Cycle-life: The cycle-life is the number of complete charge/discharge cycles that the battery is able to support before that its capacity falls under 80%. The cycle-life not only depends on the depth of discharge but is also affected by temperature and humidity. The depth of discharge is inversely proportional to the cycle-life.

Commercially available batteries include Nickel-Cadmium (NiCd), Nickel-Metal Hydride (NIMH), Lead Acid, Lithium-Ion (Li-ion) and Lithium-Ion Polymer (Li-Ion Polymer). The comparison of advantages and limitations are described in Table 4.1

- **Nickel-Cadmium** (NiCd): NiCd batteries are considerably hazardous to the environment due to the presence of toxic heavy metals. The cost is relatively low

compared with other battery technologies, with a longer charge cycle with high discharge rate. This technology is mainly used in handheld electronic industrial devices.

- **Nickel-Metal Hydride** (NiMH): The cycle-life is no better than nickel-cadmium batteries, but the energy density is improved, and toxicity is lower. This battery technology is mostly used in handheld personal electronic devices as a replacement for NiCd batteries.
- **Lead Acid:** This battery technology is heavier than the previous two batteries, but with higher energy density, and id usually used in electronic equipment that can tolerate increased weight and that requires higher energy ratings.
- **Lithium-Ion** (Li-ion): Most personal mobile devices today are powered using Li-ion batteries. With reduced weight, this battery technology can provide significantly improved energy density compared to other battery technologies.
- **Lithium Ion Polymer** (Li-ion polymer): Mainly used in handheld communication devices and with similar advantages of Li-ion battery; the Li-ion polymer can be made to be flexible or to a specific shape, however.

Table 4. 1 Comparison of types of battery chemistry

Battery	Advantage	Limitations
Nickel Cadmium (NiCd)	Fast-Simple Charging	Relatively low energy density, toxicity.
Nickel-Metal Hydride (NiMH)	30-40% capacity increase over NiCd	Battery requires regular full discharge to prevent crystalline formation
Lead Acid	Low Self-discharge rate and high energy density	Poor weight-to-energy density ratio
Lithium-Ion (Li-ion)	Relatively high energy density, low weight, ease of manufacture	Moderate discharge current Improved life cycle characteristics
Lithium-Ion Polymer (Li-ion polymer)	Less chance of electrolyte leakage, flexible technology	Less life cycle compared with L-Ion

Energy density is defined as the amount of energy stored in a given system of space-per-unit-volume. Although higher energy density can be provided by traditional battery technologies such as Lead-acid, in order to achieve a required energy, the weight of the battery can increase considerably. Lithium has been the first metal of choice for modern batteries because it is the lightest of all metals. Rechargeable lithium batteries provide a high voltage, high capacity and high energy density compared with most other battery technologies. Some of the primary lithium battery technologies include Li/SO_2, LI/MnO2, and Li/ClO4. Since lithium metal is naturally unstable, especially during charging, the focus has recently shifted to non-metallic lithium batteries. The first Li-ion battery was introduced in 1991 by the Sony Corporation, and since, the Li-ion has become one of most popular storage units used in many different applications (Schalkwijk and Scrosati 2002). The lithium-ion system has a lower energy density than the older lithium metal system, but it is safer than its predecessors. The Li-ion is preferred because its characteristics include high voltage, high energy density, low self-discharge rates and excellent cycle-life compared with other batteries.

Although lithium-ion batteries have their obvious advantages, care must be taken when charging these batteries to prevent damage to the lithium cells. Peukert's Law (also known as the rate capacity effect) expresses the capacity of a battery in terms of the rate at which it is discharged, and describes the power relationship between the discharge current and the delivered capacity. For a one-ampere discharge rate, Peukert's Law states that:

$$C_p = I^k t \tag{4.1}$$

Where C_P is the capacity of the battery at one Ampere discharge rate, the unit is ampere hours, I is the actual discharge current, k is Peukert's constant, and is dependent on the battery chemistry, and t is the discharge time. This expression is often reformulated to a known capacity and discharge rate:

$$t = H(\frac{C}{IH})^k \tag{4.2}$$

Where H is the rated discharge time, and C is the rated capacity at that discharge rate.

Thus, if a battery is discharged at a higher current or shorter time than rated, the capacity of the battery will reduce. The discharge curve presented on manufacturer data sheets are mostly for constant current discharging, and the battery discharge current is calculated using

a constant current discharge figure at room temperature. However, WSNs commonly exhibit relatively large, fluctuating load currents, which can exceed the maximum discharging capacity of batteries, for example, during WSN during *wake-up* or *transmission* phases, and significant energy can be lost in the internal impedance of the battery. Catastrophic voltage drops can occur during these peak current demands, which in turn can lead to problems with voltage sensitive electronic components such as microprocessors. Typically, a battery is sized for a system based on its expected average power consumption, so the large pulsed--discharging current behaviour of a WSN can thus drastically shorten the cycle-life of a battery.

Battery Cycle-life is the number of charges, and discharge cycles before the current capacity of the battery falls to less than 80% of the capacity when the battery was new. The Li-ion thin-film battery has a higher cycle-life compared to other batteries. It is difficult to predict the cycle-life of batteries using an accelerated testing model, for example, since battery life is affected by temperature, as well as the rate and depth of the discharge cycle. In terms of the chemical reactions internal to the battery, these are driven either by voltage or temperature (Dearborn, 2005). Generally, however, the colder the battery, the slower the chemical reaction resulting in a decreased performance and loss of battery life and a reduction in performance. This can be a particularly important characteristic when selecting battery technologies for aerospace applications.

4.1.2 Li-Ion Battery used in the experiment

The MEC202 thin-film Li-ion battery was originally selected as the battery of choice by the industrial sponsor of this project. This battery was unfortunately discontinued mid-way through the research project, so a LIR2450 Li-ion battery, as shown in Figure 4.6 has been used as a replacement. The nominal voltage of the LIR2450 cell is 3.6V, its charging voltage is 4 V, and its discharge cut-off voltage 2.75 V. The batteries operating temperature range is specified as -20°C to +45°C, but for completeness, and as this was the plan for the original battery, the charging and discharging characteristics of LIR2450 was tested in the temperature range of -40^{o}C to +40^{o}C.

Figure 4.6 LIR2450 Li-ion batteries with battery cover

Although not the ideal choice of battery, the LIR 2450 was selected as the best alternative for this experimental study due to it being readily commercially available, and to allow the novel ideas of switched-energy storage in chapter 6 to be continued and further developed. Although there were other solid-state batteries available from Cymbet Corporation, the energy ratings (5µAh to 50µAh) were not suitable for this application.

4.1.3 Standard Li-ion battery VS Thin-film solid state battery

The rechargeable Li-ion battery has high energy density compared with other battery technologies and is usually the preferred choice of the power source from smartphones to aircraft applications. However, the standard rechargeable Li-ion battery suffers from the build-up of dendrites, a problem popularised by the grounding of Boeing flights in 2013, as Li-ion batteries, affected by dendrites were shone to be prone to failure, overheating and catching fire. Dendrites may occur due to the fast charging and discharging cycles or high current flow during the discharge. Dendrites are a growth of microscopic fibers of lithium on the surface of lithium electrolyte and can eventually contact the other electrolytic material.

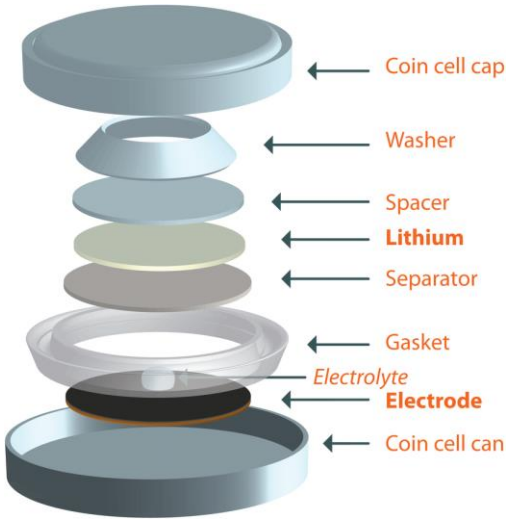

Figure 4.7 Li-ion coin cell cross-sectional view (Lin, Nordlund et al. 2014)

The electrical current that passes through this dendrite is thought to be the cause of overheating, resulting in the potential explosion of the battery (Tarascon and Armand 2001). Many researchers have worked on ways to prevent dendrites growth in Li-ion battery (Zhang 2007), and the most common method is a uniform current distribution throughout the *separator* of the battery. The separator is a layer between the two electrolytes as shown in Figure 4.7.

In contrast, the thin-film battery is not a standard Lithium battery and uses a solid-state electrolyte – a material referred to as LiPON (Lithium phosphorus oxynitride) as shown in Figure 4.8. This material has the benefit of allowing the ready flow of lithium ions for high currents, to avoid the risk of dendrites and minimizes the leakage current.

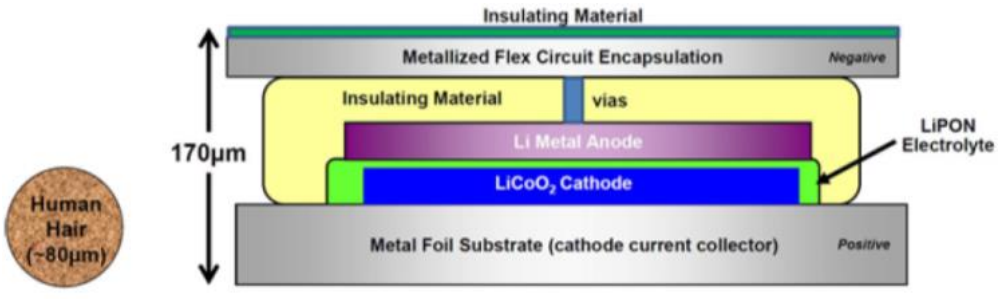

Figure 4.8 A cross-section of a solid-state thin-film battery (infinite power solutions, marketing material on advantages of MEC batteries)

Thin-film secondary cells are a specific class of lithium-ion cell in which the reduced dimensions of the components increase the active surface areas of the electrodes, allowing manufacturers to combine more active ingredients into a smaller cell volume. The result is dramatically increased performance, most notably in the power and energy density ratings. The electrolyte is also solid state; a unique benefit of solid-state thin-film batteries is their ability to work at low temperatures. Having a solid-state electrolyte ensures issues such as the battery case breaking and causing leakage, is no longer a limitation.

With more energy density, the use of the solid-state battery can considerably reduce the overall physical size of the WSN. Solid-state batteries are also environmentally friendly in comparison to traditional batteries, being less harmful to the environment. The advantage for this type of solid-state Li-ion battery are described in Table 4.2.

Table 4. 2 Comparison of commercially available batteries

Manufacturer	Chemistry	Operating Voltage	Cut-off Voltage	Average Cycle-life	Weight m gm	Temperature
Infinite Power Solutions MEC202	Li-ion thin-film	4	2.5	10000	975	-40^{o}C to +85^{o}C
Varta	Nickel-metal hydrate	3.6	3	1000	1300	-20^{o}C to +85^{o}C
Maxell	Li-Magnese Dioxide	3	2	1500	1500	-20^{o}C to +75^{o}C
	Li-Polymer	3.7	3	1000		-20^{o}C to +85^{o}C
Cymbet	Li-ion Solid State	4	2.4	5000	50	-40^{o}C to +85^{o}C
Yuasa	Nickel-Cadmium	1.2	-	1000	50000	-20^{o}C to +85^{o}C
Multicomp	LI-ion Coin	3.6	2.75	1000	5500	-20°C to 45°C

For the reasons highlighted below, the Li-ion thin-film battery is often used in aircraft energy harvesting applications and on this basis, requires further experimental characterisation.

- The MEC202 thin-film Li-ion battery is suitable for energy storage with energy harvesting sources because it can be efficiently recharged with pulsed or continuous current as low as 1 µA
- The average cycle-life of the thin-film solid-state Li-ion battery is 10000 cycles, whereas the standard Li-ion battery is typically only 1000.
- The operational temperature range is better in comparison with standard Li-ion cell batteries.
- With more energy density, think film Li-ion battery is preferred for powering WSN.
- Thin-film solid-state Li-ion batteries have a protection layer to prevent the occurrence of dendrites.

4.2 Supercapacitors

The disadvantages of batteries have led to the development of supercapacitors as an alternative storage approach. The supercapacitor, also known as a double-layer capacitor, can provide high-energy density as the capacitance increases. For this work, the most significant advantage over batteries, however, is the supercapacitor can also provide high power density. Typically, the WSN demands high current in various operational modes, and typically in pulses in the millisecond time range. Additionally, it should be noted that harvested energy does not provide a constant source of energy, and charging will only happen during times of energy availability. Because of this, the energy storage elements will be exposed to many charge and discharge cycles. With a much higher cycle-life performance compared to a battery, the supercapacitors are often the preferred choice.

4.2.1 Supercapacitors Specifications:

I. Polarity: Like batteries, supercapacitors are designed with positive and negative electrodes.

II. Cycle-life: Supercapacitors have a much longer cycle-life than rechargeable batteries, but not infinite. The effect of external factors such as temperature can increase the equivalent series resistance (ESR) and also reduces the capacitance, although this effect is much smaller in comparison to batteries.

III. Nominal Voltage: Supercapacitors are rated with a nominal working voltage. Prolonged exposure to increased working voltage can reduce the lifetime.

IV. Leakage current: Due to the way in which supercapacitors are constructed, there is a high-impedance internal leakage current path from the anode to the cathode. This means that in order to maintain the charge on a capacitor a small amount of additional current may be required.

In 1957, researchers from General Electric Company (GEC) performed the first experimental study into the concept of the supercapacitor, although at that time, there was no commercial application for such an electronic storage element. During the research work on the fuel cell in 1966, Standard Oil Company invented an efficient way of storing energy in the form of a double layer capacitor. This technology was sold to the NEC Company, who marketed it in 1978 as physical memory backup device for personal computers (Brodd, 2004).

With the advancement of materials in early 1990's the electric double-layer capacitor (EDLC) was manufactured with better efficacy than its predecessors. As shown in Figure 4.9, the EDLC consists of two layers activated carbon with an electrolyte and a separator. The double layer phenomenon is defined as the absorption and desorption of ions as the voltage is applied (Wei and Ng 2009). The capacitance is directly proportional to the surface area, as the energy density of the supercapacitor increases, the size also increases.

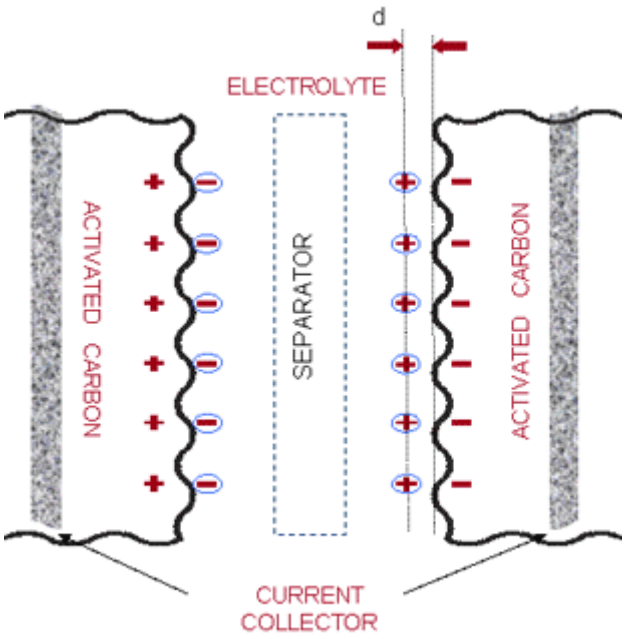

Figure 4. 9 Schematic of ELDC (white paper on cellergy CAP technologies)

The current supercapacitor competes with, and in some cases, can replace the battery due to advantages such as rapid-charging and near unlimited cycle-life. Unlike the electrochemical battery, which has a defined cycle-life, there is little degradation caused by cycling a supercapacitor and age does not affect the device in the same way as it has an impact on a battery. The supercapacitor can be charged and discharged, a virtually unlimited number of times (Wang et al., 2009). Unlike the battery, the supercapacitor does not require overcharging production circuit, the charging current stops once the supercapacitor is fully charged.

The advantages of supercapacitors are high power density and high cycle-life. Supercapacitors can accommodate the peak current demand from a wireless sensor, due to their enhanced power density. The electric double-layer capacitor or supercapacitor can operate comfortably over a wide temperature range, commonly -40^{o}C to +70^{o}C, which importantly is suitable for aircraft applications considered in this thesis. However, long time exposure of the supercapacitor to higher temperatures will reduce its cycle-life, as the temperature is a significant factor in the ageing of storage systems.

4.3 Experimental Setup: Characterisation of a Li-ion thin-film battery, a standard Li-ion battery and a supercapacitor

As the aircraft application considered here is temperature dependent, the storage elements need to operate at least from -20^{o}C to +40^{o}C, and as is considered here, a worst-case range between -40^{o}C to +40^{o}C. In the applications considered here, this allows the use of thermoelectric modules, but also presents a problem as the ESR of storage units varies significantly with temperatures. In the experimental work presented here, a climatic chamber within a range of -40^{o}C to +40^{o}C as shown in Figure 4.10 is used to model this environment, and to characterise the storage elements. Equipment used for the experiments are a Keysight N6705B-DC Power Analyser comprising a N6781A: a 2-Quadrant Source/Measure Unit for Battery Drain Analysis and a N6784: a 4-Quadrant General-Purpose Source/Measure Unit.

LabVIEW is an industry standard software programming and control environment that has been used to interface with and control the N6705B and for data logging. Keysight's 14585A control and analysis software were used for creating the energy harvesting power output profile required for TEG emulation.

Figure 4.10 Experimental set up for characterisation of energy storage elements under the different temperature range with climatic chamber

4.3.1 Charging Experiment

The TEG output profile created in section 2.5 was used to programme the N6705B power analyser, and to charge the batteries and supercapacitor. The charging voltage applied to the energy storage elements was data logged using a dedicated channel (channel-2) of the N6705B power analyser. The N6705B power analyser output was used to drive the LTC 3109, and the storage element was connected directly to the V_{out} pin of LTC3109. To analyse the influence of temperature on charging batteries and supercapacitors, an experimental arrangement was designed within a climatic chamber with a temperature range capability of -40^{o}C to +40^{o}C.

4.3.2 Discharging Experiment

A pulsed-load representing the *node-idle* and *transmission* states of the strain WSN, explained in chapter 2.5, was used as the load condition. This involved establishing a *node-idle* state with duration (t_o) of 4.95 s and a current demand of 0.07 mA, followed by a *transmission* state with duration (t_1) of 50 ms and a current demand of 14.95 mA. The total time (t) of one cycle was 5 s. This pulsed- waveform emulates the load, and the discharge voltage of each storage element is data logged and later plotted. To analyse the temperature influence on battery and supercapacitor discharge, an experimental arrangement was designed and cycled within a climatic chamber within a range of -40^{o}C to +40^{o}C.The batteries and supercapacitors were charged and discharged at the same temperature.

4.4 Result-Analysis: Characterisation of Li-ion thin-film batteries, LIR2450 standard Li-ion battery and Supercapacitor

4.4.1 Leakage Current Measurement - MEC 202 battery

To measure the leakage current, i.e. the additional charging current required to maintain the storage element at the specified voltage value, the Keysight N6705B was set-up as a DC power supply, and channel-2 was used for the current measurement. A 1 Ω, R_{ext} precision resistance was connected in series with the battery. The positive and negative terminal of channel

N6705B was connected to the positive and negative terminals of the battery. The channel 2 was connected across the $R_{ext,}$ and the channel 2 was set up as voltage measurement unit. A jumper was installed across the R_{ext}. The battery was charged to 4 V with a constant voltage charging method. After the one-hour hold, the jumper across the R_{ext} was removed. The voltage V_{ext} across the R_{ext} was data logged 1 sample per minute on channel 2.

$$Leakage\ current = V_{ext}/R_{ext} \quad (4.3)$$

The measured maximum leakage current for the MEC202 thin-film battery was found to be 0.006mA at room temperature (20^{o}C). This measurement was then repeated at various temperatures within the climatic chamber, as detailed in Table 4.3.

Table 4. 3 Leakage current of MEC 202 at various temperatures

Temperature ^{o}C	Maximum Leakage current mA
+40^{o}C	0.08
+30^{o}C	0.02
+20^{o}C	0.006
-20^{o}C	0.006
-30^{o}C	0.012
-40^{o}C	Discharging collapsed

4.4.2 Charging Characteristics of Li-ion thin-film battery-MEC202

The MEC 202 battery was charged at a constant voltage of 4V as shown in Figure 4.10, using the Keysight N6705B. Constant voltage charging is recommended throughout in the datasheet as the MEC 202 has high internal resistance and provides sufficient current limiting so long as the voltage does not exceed the maximum charge voltage. No current limiting circuit or battery charging IC is used in this charging experiment as Keysight N6705B is a precise DC power source and analyser.

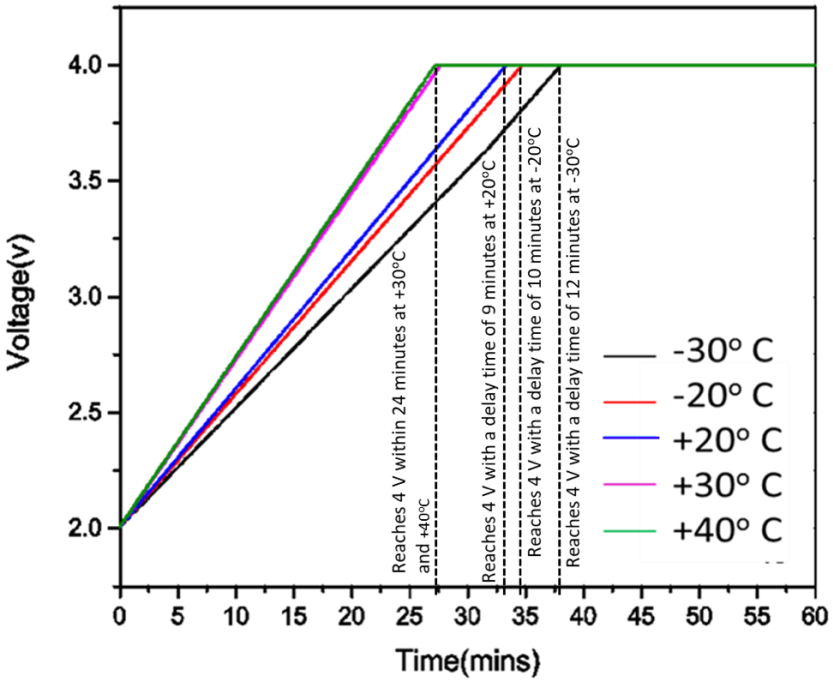

Figure 4. 11 Charging profile of a MEC 202 in different temperature range

In all cases, the charging was initiated from 2 V, which is the battery's cut-off voltage and was charged at a constant voltage of 4V, with 25 mA charging current as shown in Figure 4.11. The charging time can be seen to be more or less same for -20^{o}C and +20^{o}C. The Charging time is considerably reduced as the temperature increases, and in -40^{o}C no charging took place, so it was not shown.

The MEC202 thin-film battery was not charged using the TEG output profile created in chapter 2.5; the battery was discontinued. LIR 2450 standard Li-ion battery will be used as a replacement.

4.4.3 Charging Characteristics of Li-ion battery - LIR2450

The experiment was set up for 80 minutes and tested in 2 trials, with +/- 1% error bar added to the graph, to identify any errors over +/- 1 % of the values.

The LIR2450 was charged in two different voltages, first with a constant voltage of 4V, and then using the TEG voltage output profile as identified section 2.5.1. To demonstrate the switched-energy storage, LIR 2450 was charged with created TEG output profile from chapter 2.5. The LIR 2450 operating temperature range is -20°C to 45°C, but to suit the aerospace application, this was extended to include testing at -30^{o}C and -40^{o}C.

For the constant voltage charging method, the battery was discharged with 1Ω load resistance down to 3.5 V at the same temperature used for charging. The constant voltage experiment was tested in 2 separate trials to establish some degree of repeatability and accuracy of the results. Channel-1 of N6705 B was set up as a source, and channel 2 was used for data logging the charge curve of the battery.

As shown in Figure 4.12, the LIR2450 starts to charge immediately and reaches it charging voltage level of 4 V within minutes in the positive temperature range of +30°C to +40°C. The increase in temperature increases the movement of ions in battery and so the charging time was lesser in high temperatures. The battery reaches it charging voltage of 4 V with a delay time of 28 minutes at -20°C and +20°C. The charging rate reduces further to 33 minutes delay at -30°C. And in -40°C it never reaches the 4 V charging voltage during the 80 minutes experiment.

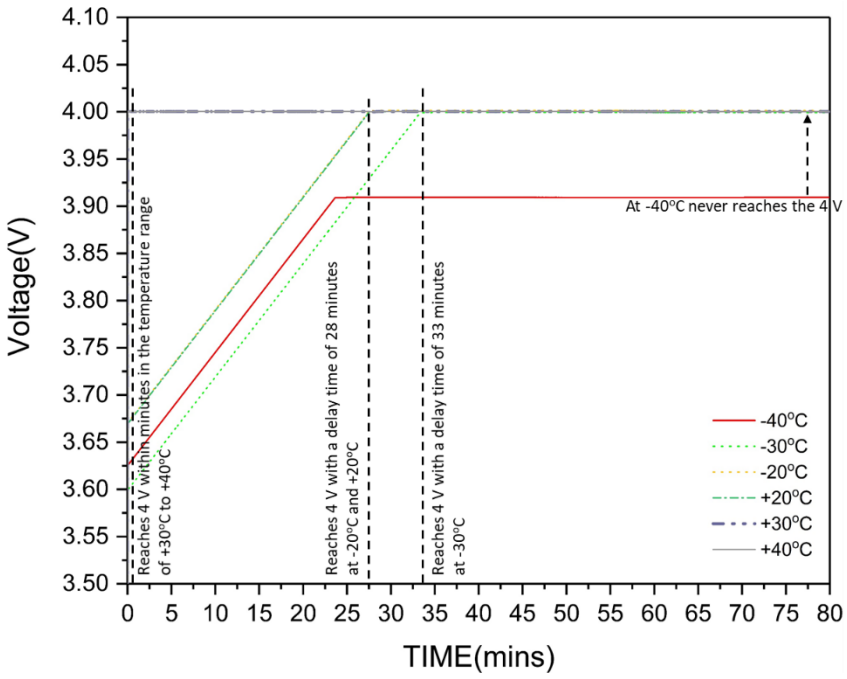

Figure 4. 12 Charging profile of a LIR2450 in different temperature range with a constant charging voltage

1% error bar was added to the graph, as shown in Figure 4.13. There is no error observed outside of this bound, for the 2 trials.

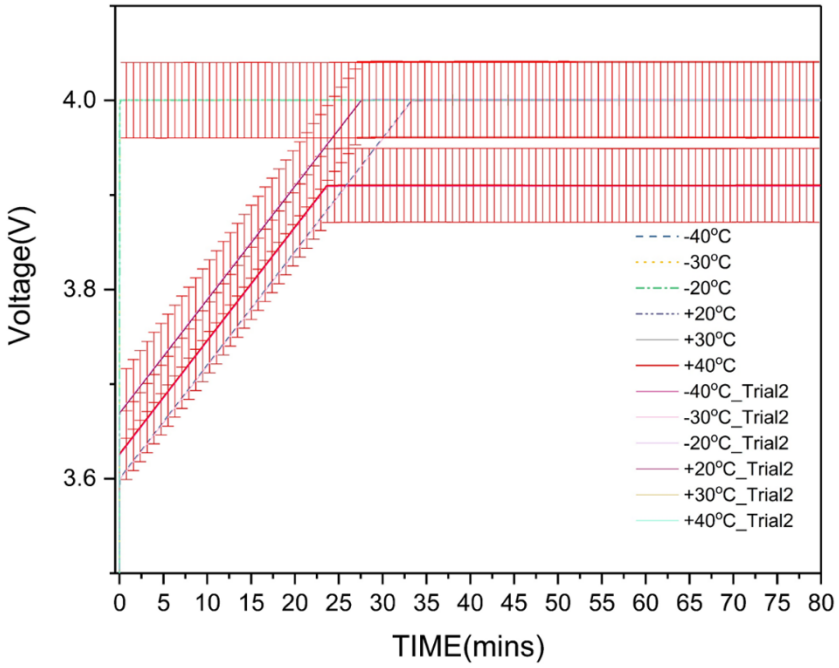

Figure 4. 13 Charging profile of a LIR2450 in different temperature range in 2 trials with +/-1% error bar

The LIR 2450 charges well within the temperature range of +20°C to +40°C and with charging time delay in the temperature range of -20°C to -40°C. -30°C to -40°C is below the operating temperature range of LIR 2450.

The TEG output profile generated by the N6705B was delivered to the input of the LTC 3109 DC-DC converter, and channel 2 was used for capturing the battery voltage at the V_{out} pin of LTC3109. As shown in the Figure 4.14 the LIR2450 charging rate considerably reduces as the temperature decreases. At constant voltage charging method in -40°C, LIR 2450 was charged only up to 3.90 V from 3.5 V, in other temperatures the battery was able to reach 4 V with time delays. The LIR 2450 charged with LTC 3109, was able to reach 3.9254 V from 3.9461 at -40°C, at both the charging methods the -40°C temperature range was the least charging rate compared with other temperatures.

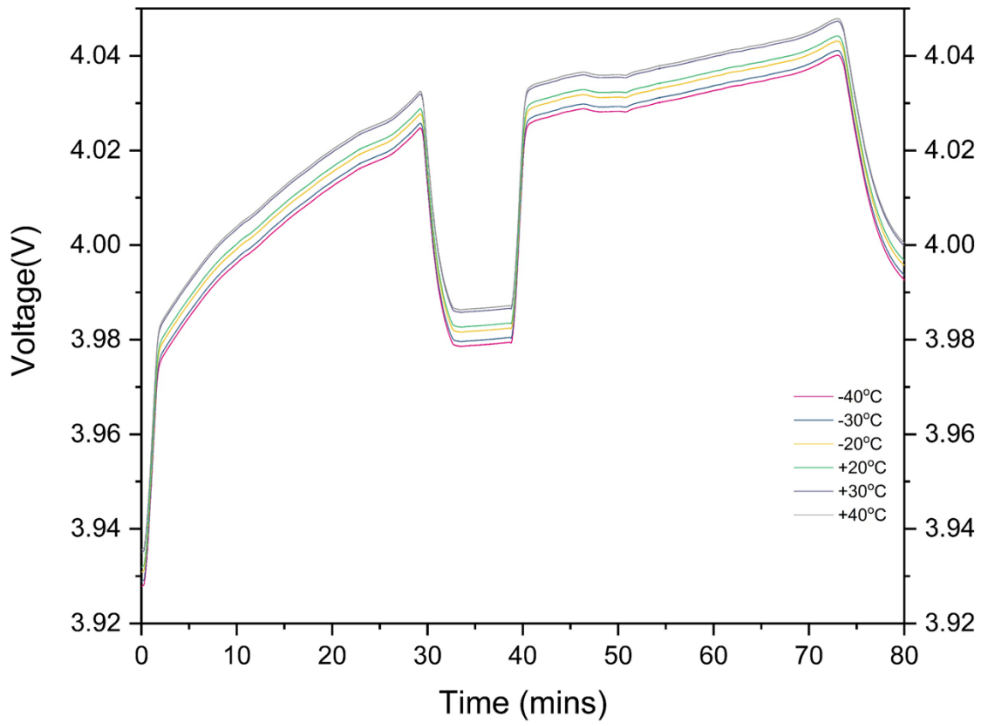

Figure 4. 14 Charging profile of a LIR2450 in different temperature range with generated TEG energy harvesting output profile at different temperature range

The LIR2450 could charge up to 4.0025 V at +40°C and charge up to 3.9925 V at -40°C, as described in Table 4.4. No error over plus or minus 1 % were identified with the measured values as shown in Figure 4.15.

Table 4. 4 LIR2450 charged voltage levels at various temperature ranges

Temperature at degree Celsius	LIR2450 charged voltage V
-40°C	3.9925
-30°C	3.99483
-20°C	3.9953
+20°C	3.9965
+30°C	3.9969
+40°C	4.0025

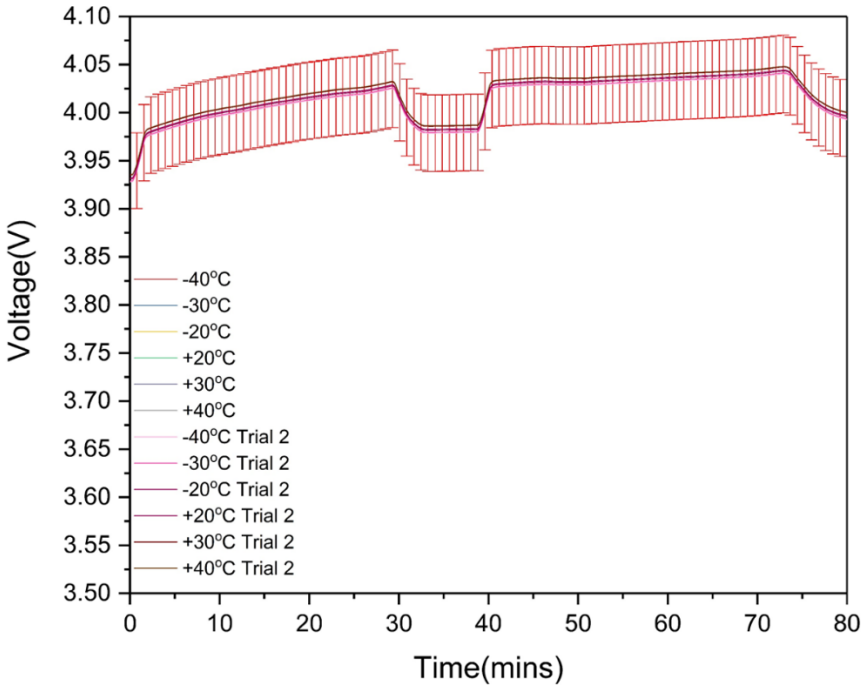

Figure 4. 15 Charging profile of a LIR2450 from the generated TEG energy harvesting profile at different temperature range with +/-1% error bar, for 2 measurement runs

4.4.4 Discharge Characteristics- Li-ion battery- MEC202

At higher temperatures, the MEC202 can be seen to have improved performance as the mobility of the electrolyte materials increases, resulting in lower internal resistance, which in turn increases the effective capacity of the battery, as shown in Figure 4.16. At a low temperature below -20 °C, the MEC202 battery clearly cannot function correctly and does not achieve the charge voltage. For negative temperatures, there is an abrupt collapse in voltage at different points of the discharge curve. This is because the increased internal resistance of the battery leads to reduced capacity. At -40°C the battery does not function at all, and the experiments were repeated to confirm this. As the temperature increases, the movement of ions increased, and the capacity improves leading to better performance of the battery.

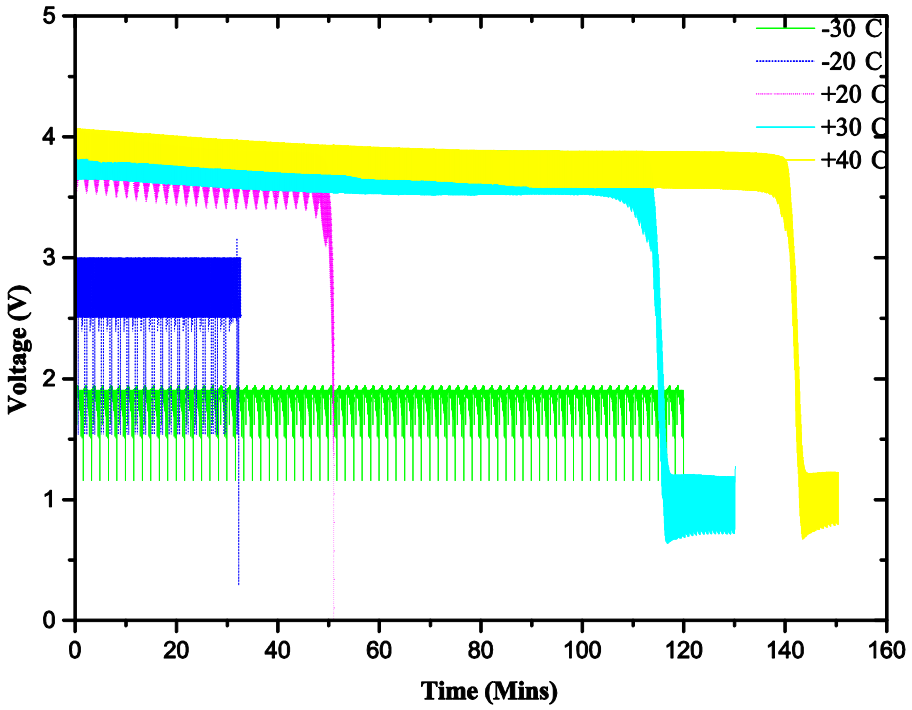

Figure 4.16 Discharge curve of thin-film Li-ion Battery under Pulsed-load Condition at different temperatures.

The discharge curve data was logged at 20ms/Sample; the voltage drop was created by the high peak current demand at every 5 seconds, explained the batteries reduced discharge rate under pulsed-load condition. With the increase in battery resistance at a negative voltage, the voltage drops increases, and the batteries discharge curve collapsed. With a high sampling rate of 20ms/sample resulted in the distorted curve as shown in Figure 4.16.

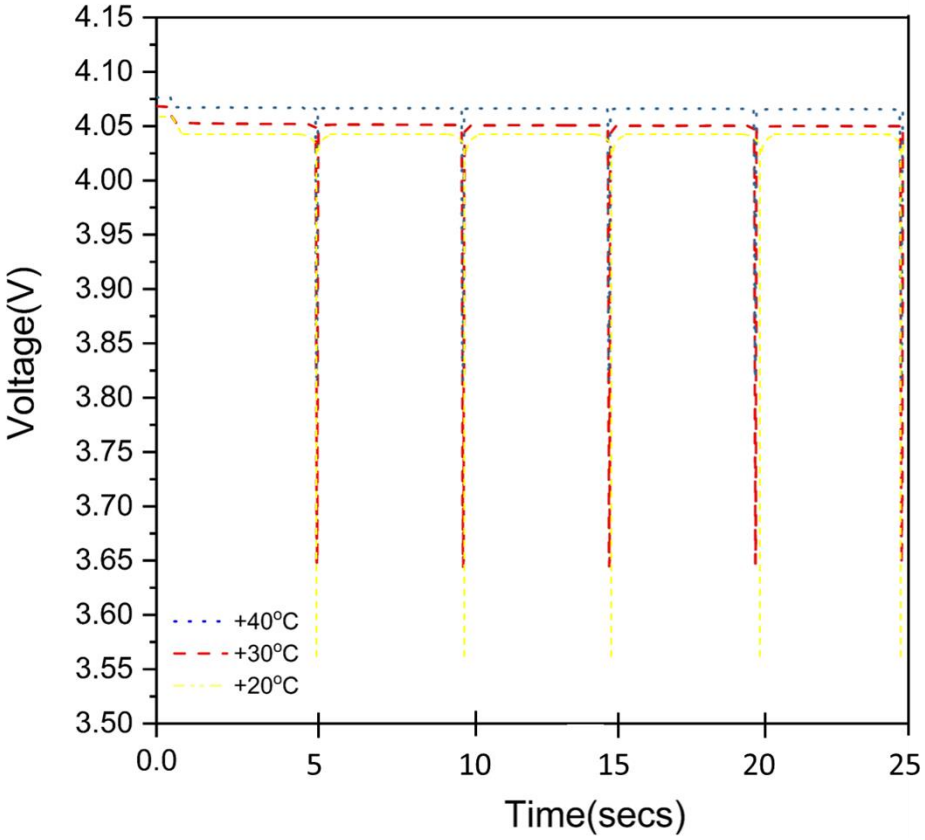

Figure 4.17 Voltage drop comparison from +20°C to +40°C of thin-film Li-ion battery under Pulsed-load Condition (this is the same plot as Figure 4.16 but for a compressed time frame)

The power density of the battery is low compared with supercapacitors, and with a relatively low capacity of 1.7mAh and high internal resistance of 22Ω, the MEC 202 was not able to provide sufficient current during the …transmission state (t_1) of 50 ms. However, the MEC202 tries to meet the high current demand during the pulsed-load peak current demands and results in the high voltage drops as shown in Figure 4.17. At negative temperatures, the movement of the electrolyte was restricted resulting in higher internal resistance, and the voltage drops increase more for those peak current demands.

4.4.5 Discharge Characteristics- Li-ion battery- LIR2450

As was the case with the MEC202, at higher temperatures the LIR2450 has better performance, but as the temperature decreases the voltage drop increases as shown in Figure 4.18.

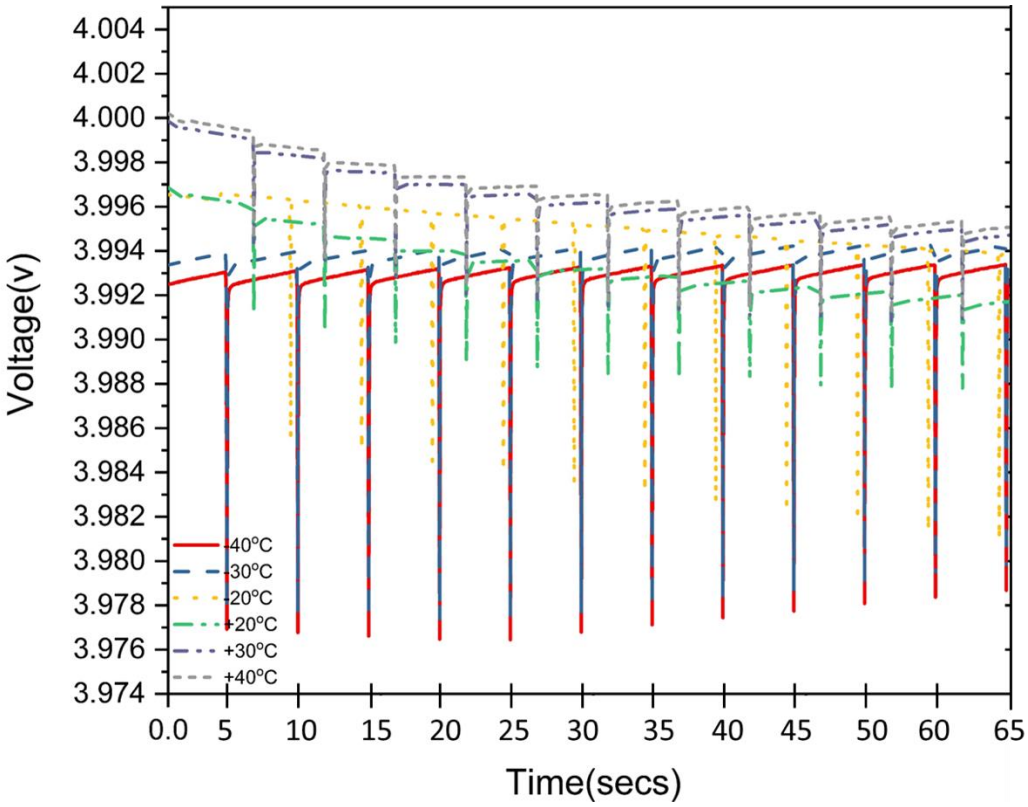

Figure 4. 18 Discharge curve of Li-ion LIR2450 battery under Pulsed-load Condition in different temperatures.

The increasing voltage drop for negative temperatures will reduce the runtime of WSN. As shown in Figure 4.18 the voltage drop is only 0.0006V at +40°C and increases to 0.016V at -40°C. Due to the increase in internal resistance of the battery at lower temperatures, the voltage drops is increased in lower temperatures.

Two separate runs of the experiment were carried out for the confirmation of results. The discharge experiment was conducted within 3 minutes of the charging experiment to make sure charging and discharging are experimented were in the same temperature range. As shown in Figure 4.20, the repeat measurement results varied by much less than 1% .

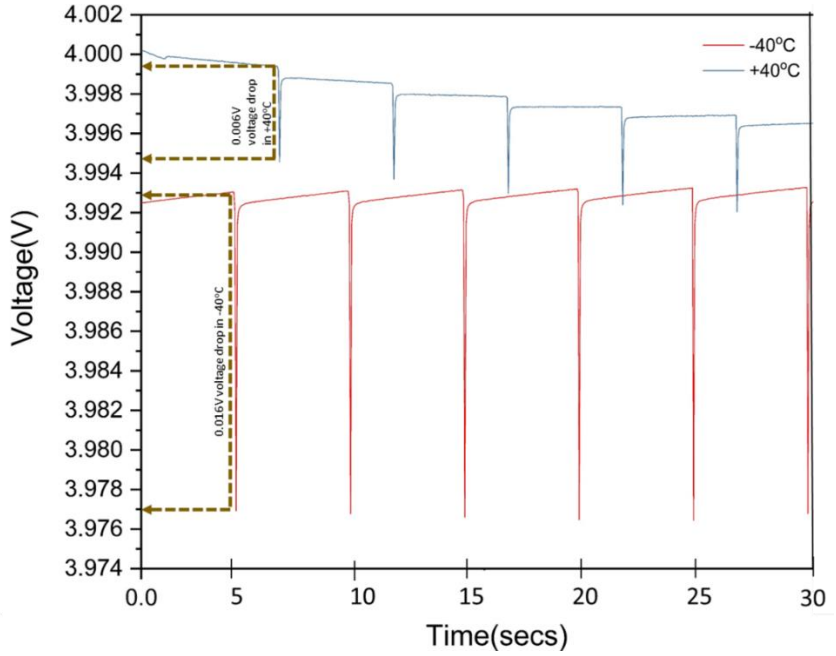

Figure 4. 19 Voltage drop comparison at -40°C and +40°C of Li-ion LIR2450 battery under Pulse Load Condition (this is the same plot as Figure 4.18 but for a compressed time frame)

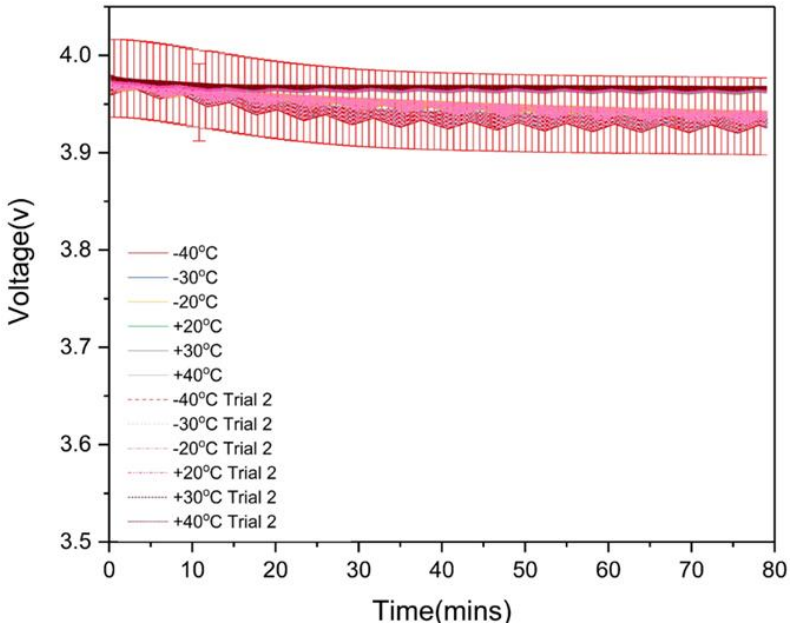

Figure 4. 20 Discharge profile of Li-ion LIR2450 battery under Pulsed-load Conditions, for different temperatures with +/-1% error bar

The operating temperature of LIR 2450 is -20°C to +45°C, but the experiment was carried out at a lower temperature than their minimum operating temperate. The exposure of the battery to lower operating temperatures considerably decreases the cycle-life of the battery.

4.4.6 ESR and capacitance of a supercapacitor

The equivalent series resistance (ESR) contributes towards the voltage drops for the pulsed-load discharge. The ESR varies depending on the temperature as the application demands the supercapacitor to work in the temperature range of -40^{o}C to + 40^{o}C. It is necessary to measure the ESR at a different temperature to understand the voltage drops caused due to pulsed-load in a supercapacitor(Gualous, Bouquain et al. 2003). The value of capacitance also varies based on the temperature, and to calculate the exact amount of energy to be stored in a supercapacitor. The change in capacitance of supercapacitor based on temperature must be measured.

In order to measure the ESR and capacitance of various supercapacitors, the Keysight N6705B power analyser instrument specific parameters were established through the instrument's user interface software: *amp*= 0; *end amplitude* = -2; *delay* = 2; *pulse time* =4; *end time*= 2; *reset count* = 1 (Maxwell technical guide). The required discharge curve was established by setting up the markers on the data logger. The capacitance and ESR were then measured and calculated using equations (4.4) and (4.5). The experiment is conducted between -40^{o}C to + 40^{o}C in the climatic chamber using Keysight N6705B.

$$Capacitance = \frac{Id*td}{Vw-Vf} = \frac{Id*td}{Vd} \quad (4.4)$$

$$ESR = \frac{Vf-Vmin}{Id} \quad (4.5)$$

Based on the constant current test (Maxwell Technical Guide 2010), it was possible to calculate initial working voltage $V_{w,}$ discharge current I_d, voltage 5 seconds after removal of load $V_{F,}$ minimum voltage under load V_{min}, and time to discharge from the initial voltage to minimum voltage $t_{d.}$

Increases in ESR at the lower temperature are only a temporary effect due to the increased viscosity of the electrolyte and slower movement of the ions. Increases in ESR at the higher

temperature are a result of permanent degradation due to the electrolyte decomposition inside the supercapacitor (Uno and Tanaka 2012).

Table 4.5. Measurement of ESR and Capacitance for a variety of different supercapacitors at different temperatures.

Manufacturer	Maxwell PC 10-5 F		Maxwell BP series-5 F		Panasonic 5 F		Nesscap 2.5 F		Cap xx 1.20 F	
Temperature degrees	ESR mΩ	Capacitance	ESR mΩ	Capacitance	ESR mΩ	Capacitance	ESR mΩ	Capacitance	ESR mΩ	Capacitance
-40	389	4.82	152	4.67	261	4.78	72	2.42	70	1.53
-30	381	4.86	149	4.76	254	4.82	66	2.29	64	1.49
-20	379	4.89	142	4.84	249	4.94	62	2.32	54	1.46
+20	371	4.85	140	4.89	244	5.2	65	2.38	52	1.46
+30	402	4.84	144	4.72	249	4.98	72	2.28	59	1.38
+40	418	4.82	154	4.66	259	4.88	81	2.17	64	1.24

4.4.7 Self-Discharge Characteristics of Supercapacitor

The main disadvantage of the supercapacitor is the high associated self-discharge rate and leakage current (which is essentially the same thing measured in different ways). These are due to the supercapacitor construction which results in a high impedance internal current path from the anode to the cathode. To maintain the charge on the capacitor a small amount of additional current is required and during charging is referred to as the leakage current. When the charge voltage was removed, and the supercapacitor not loaded, the capacitor will naturally discharge through this high-impedance, and this is referred to as self-discharge. The initial self-discharge rate and the effect of time are as shown in Figure 4.21.

The supercapacitors were charged to 4 V, using the channel 1 of N6705B. The same channel was switched into voltage measurement mode, and the open circuit voltage of the supercapacitor was recorded for 24 hours. With equation 4.6, the self-discharge in percentage was calculated using the excel. V the charge voltage and V_o the measured open circuit voltage.

Self-discharge (%)= $abs(100 * \frac{V-Vo}{Vo})$ (4.6)

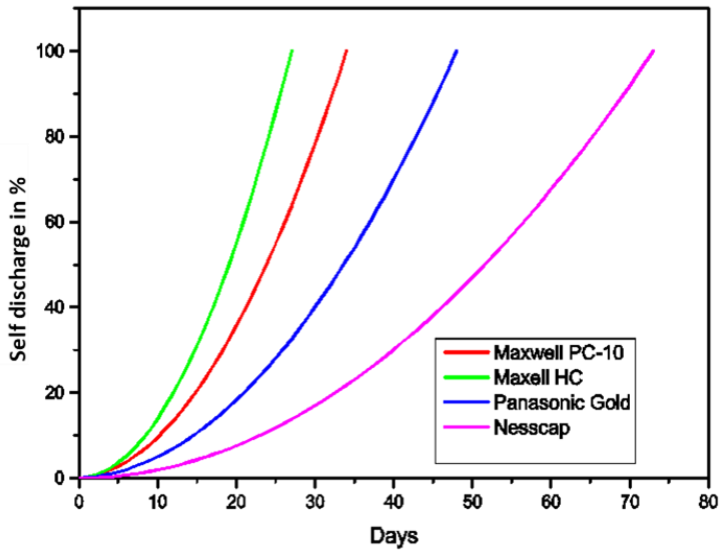

Figure 4. 21 Self-Discharge rate at room temperature

The self-discharge rate was not monitored over different temperature ranges, but it is known that it varies as the ESR and Capacitance changes. Leakage current was measured for two Maxwell PC-10 5 F supercapacitors in series, in various temperature as listed in Table 4.6, with the same principle used for battery using Keysight N6705 B. As expected there was little difference in leakage current difference as a function of temperature, however, the leakage current for the MEC 202 battery comparatively high.

Table 4. 6 Leakage current of two Maxwell PC-10 in series 5 F at various temperatures

Temperature °C	Leakage current mA
+40°C	0.094
+30°C	0.091
+20°C	0.086
-20°C	0.086
-30°C	0.078
-40°C	0.072

4.4.8 Charging Characteristics of Supercapacitor- with constant voltage

The Maxwell two PC-10 in series 5 F, was charged up to 4 V at a charging current of 50 mA in a temperature range of -40°C to +40°C using the Keysight N6705 B. The channel of 1 N6705B was connected to the supercapacitor and the data was logged at 1 sample per second.

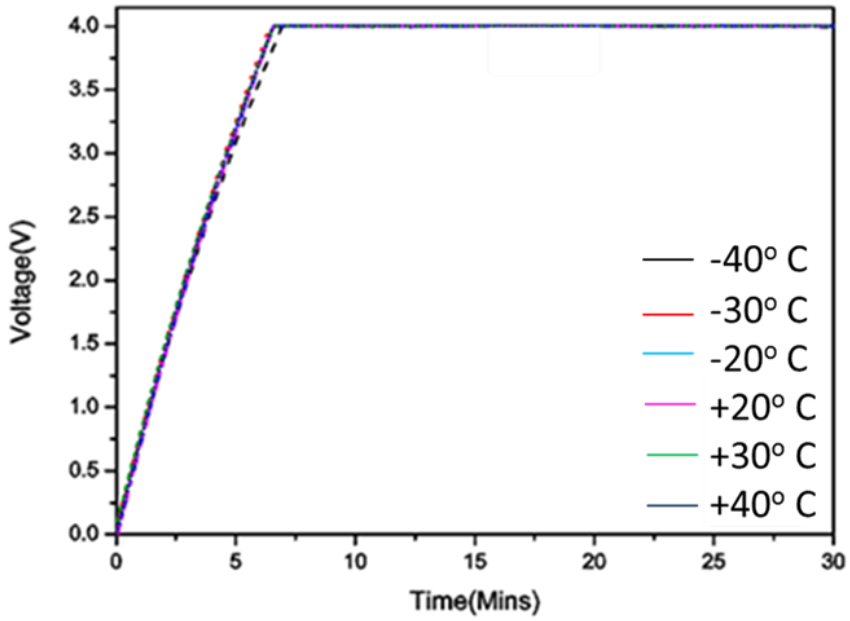

Figure 4. 22 Charging of Maxwell two PC-10 in series 5 F supercapacitor at different temperatures

As shown in Figure 4.22 the temperature does not affect the charging of the supercapacitor, that charge more or less at the same rate from -40°C to +40°C.

4.4.9 Charging Characteristics of Supercapacitor- with energy harvesting

As was the case for the batteries, the supercapacitor is also charged with TEG output profile as explained in the experimental setup, involving a voltage source and series resistance. The LTC 3109 is used as the power management unit and the supercapacitor used is a Nesscap 1.5 F is connected to the V_{out} pin of the LTC 3109. The LTC 3109 and the supercapacitor were placed in the climatic chamber, and the experiment was tested in 2 separate trials for measurement robustness. The supercapacitor was discharged down to 0.8 V at +20 ^{o}C before it was charged at +20 ^{o}C. The supercapacitor was discharged down to 0.8 V for every measurement, at the same temperature as that which it was to be charged.

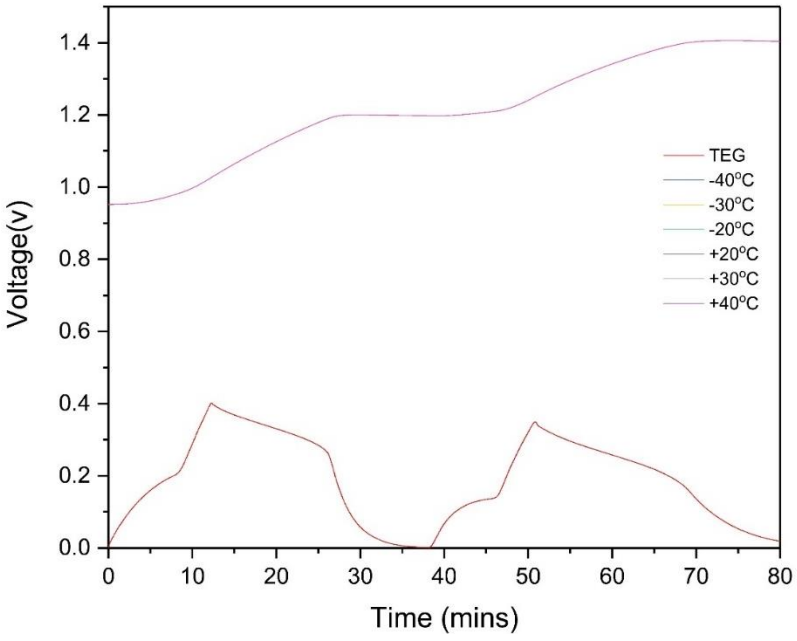

Figure 4. 23 Charging profile of a Nesscap 1.5 F using TEG output profile for different temperatures

As shown in Figure 4.23, the Nesscap 1.5 F reaches the charging voltage of 1.4 V from 0.8 V at same charging time in the temperature range of 40^{o}C to +40^{o}C for the given input voltage from LTC 3109. Similar to Maxwell 5 F supercapacitor, Nesscap 1.5 the charging time was not affected by the temperature. This is considered as on the most important advantages of supercapacitors over batteries.

As shown in Figure 4.24, no variation between measurements over plus or minus 1 % were identified with the measured values from the two repeat experiments.

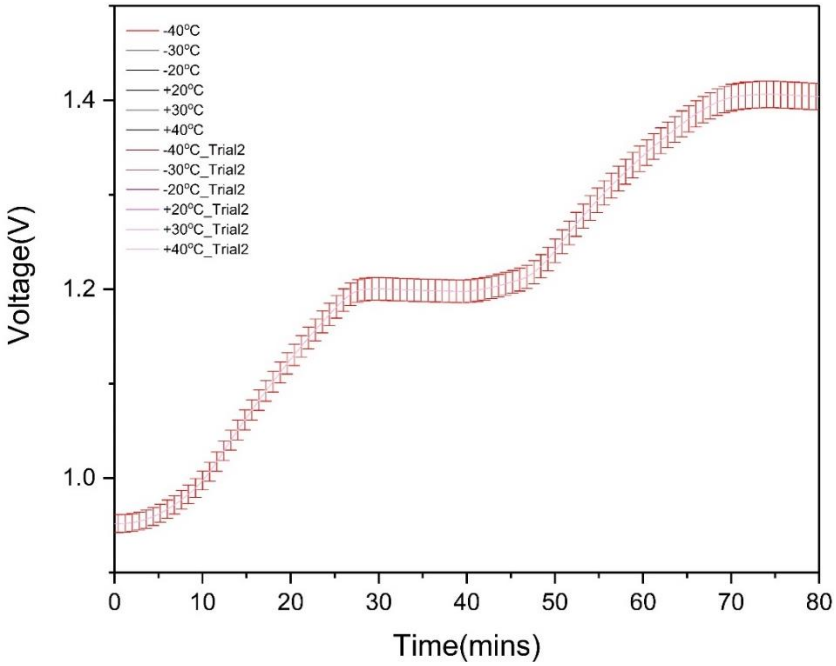

Figure 4. 24 Charging profile of a Nesscap 1.5 F using TEG output profile in different temperature range with +/- 1% error bars

4.4.10 Discharge Characteristics of Supercapacitors- without step-up

The Maxwell two PC-10 in series 5 F, was charged up to 4 V and discharged under the pulsed-load condition at temperatures in the range of -40°C to +40°C in the same way as the batteries.

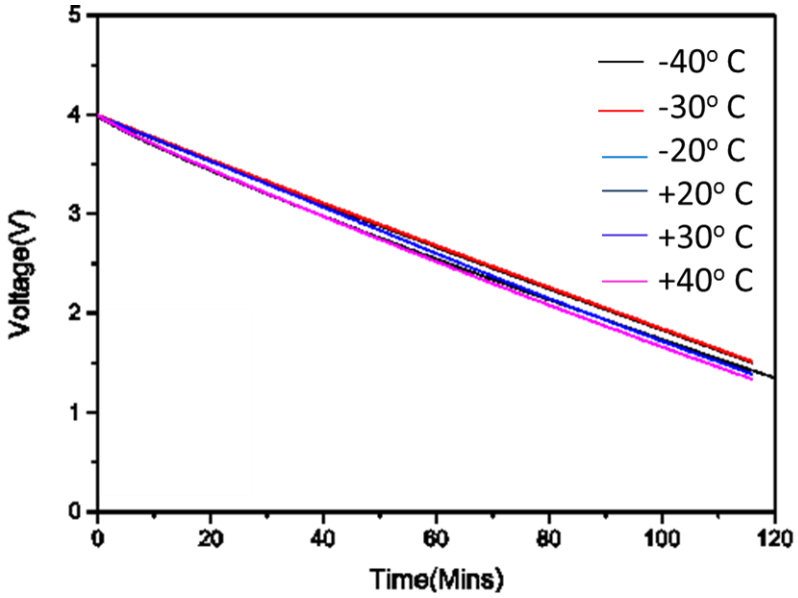

Figure 4. 25 Discharge curves of Supercapacitor under Pulsed-load Condition in different temperatures.

The discharging of the supercapacitor is not significantly affected by the temperature range as shown in Figure 4.25. In prolonged use, the temperature in combination with voltage can affect the cycle-life of the supercapacitor.

There are even small levels of voltage drop in the supercapacitor for WSN application. To minimise the voltage, drop, it is better to use a low ESR value supercapacitor. I the discharge current for t seconds and *C* is the capacitance.

$$V_{drop} = I\,(R + t/C) \qquad (4.7)$$

Figure 4.26, demonstrates that, as is the case for batteries, there is a small voltage drop in supercapacitors when presented with a pulsed-load, representing WSN. The voltage drops were relatively very small compared to the battery. So, for WSN application supercapacitor with low ESR and leakage current are preferred.

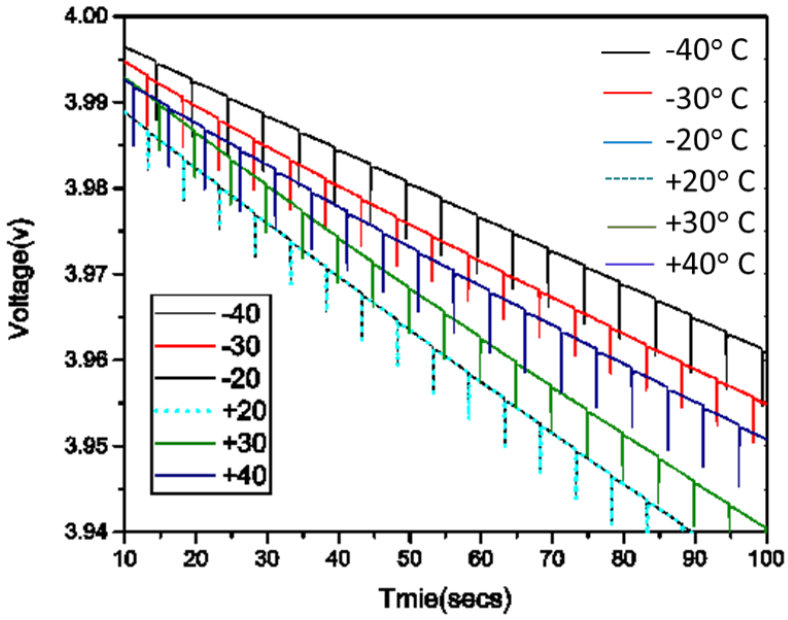

Figure 4.26 Voltage drops in supercapacitors under Pulsed-load Condition at different temperatures

4.4.11 Discharge Characteristics of Supercapacitors- with step-up converter

Even though the supercapacitor does not have a cut-off voltage like a battery, all the energy stored in the supercapacitor cannot be used because any ASHM WSN requires a constant voltage supply of typically 3.3 V or 5 V, so, powering a WSN through step-up converter from supercapacitor was a preferred method. The LTC 3539 was tested for the 5 V output, in ordered to understand the efficiency, for the maximum output voltage. The LTC 3539, has a high conversion efficiency and with no performance degradation with temperature variation as described in chapter 3.7.

The Nesscap 1.5 F supercapacitor was charged up to 4 V at + 20 ^{o} C. The supercapacitor attached as the input (V_{in}) to the LTC 3539; channel 1 of N6705B was connected to the supercapacitor for data logging the discharge curve. The pulsed-load representing WSN function of *node-idle* and *transmission* was provided as a load to LTC3539 through channel 2.

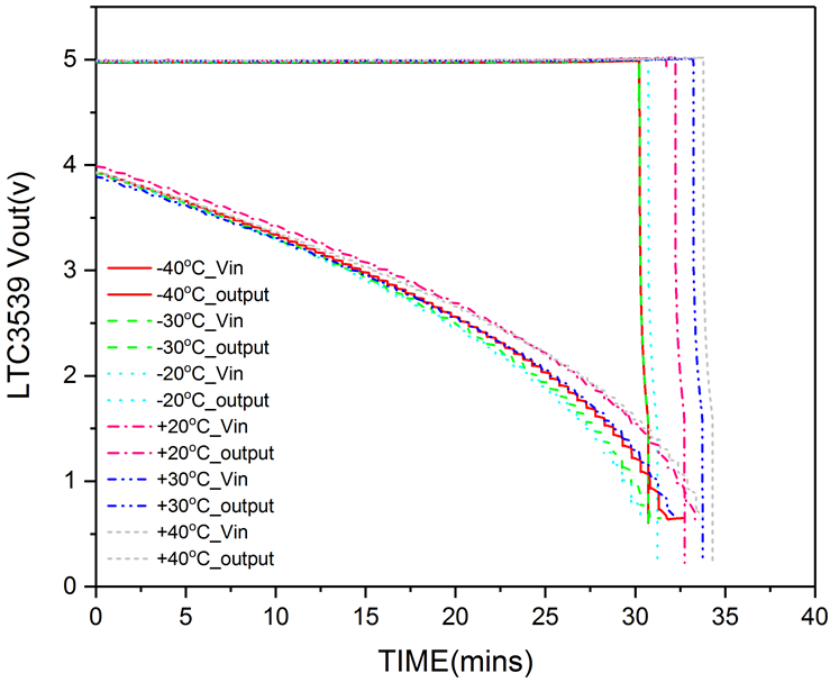

Figure 4.27 Discharge curve of Supercapacitor with Step-up LTC3539 under Pulsed-load Condition for different temperatures.

As shown in Figure 4.27 , the output voltage from LTC 3539 drops to 0 V as the supercapacitor reached 0.8 V. The Step-Up converter was able to provide a constant output voltage of 5 V under the pulsed-load condition until the supercapacitor reaches 0.8 V.

At -40 ^{o} C, the supercapacitor discharges to 0.8 V in 30 minutes, and as the temperature increases to +40 ^{o} C, it reaches 0.8 V in 35 minutes. A detailed study on energy conversion losses in LTC 3539 must be conducted, but it can be seen that by using this approach, virtually all the energy stored in the supercapacitor can be used to power the WSN. The influence of temperature introduces a discharge rate difference of approximately 5 minutes in this application. From the experimental result of Maxwell 5 F supercapacitor without a step-up converter, the discharge rate was more or less equal for all the temperature range, so the five minutes difference can be considered due to the influence of temperature in LTC3539.

4.5 Chapter Conclusion

From the critical analysis made in this chapter, two significant effects have been demonstrated. The first is, at negative temperatures a battery's internal resistance increases due to the restriction of ion movements. Secondly, The ESR of a supercapacitor increases at positive temperatures. Battery efficiency increases at a positive temperature and supercapacitor efficiency increase at negative temperatures, but prolonged usage of storage elements in adverse temperatures will reduce the life cycle of those elements. As MEC202 was discontinued, the LIR2450 was used as an alternative battery. The three major differences between these batteries are the LIR2450 has an operating temperature of -20^{o}C to +45^{o}C, the average cycle-life of 1000 measured for constant current discharge and do not have a protection layer to protect the possible occurrence of dendrites. Even though LIR2450 performed better than MEC202 in lower temperature, because of the high capacity of 120mAh, continuous exposure will further reduce the cycle-life. Both batteries and supercapacitors have their own advantages and disadvantages.

To meet the requirements of a WSN, the energy storage should have both energy density for longer running time and power density for the peak current demand, so, the battery and supercapacitor cannot be used as a standalone storage unit for WSN applications. From the

experimental results in this chapter both the MEC 202, LIR 2450 has higher voltage drops compared with a supercapacitor and the voltage drops increases with a decrease in temperature. Supercapacitor has a lower voltage drop for a pulsed-load representing WSN, but with lower energy density it is compromised in terms of how long it can supply power. To overcome this limitation, high Farad supercapacitors can be considered, but the as the capacity increases so too does the ESR and leakage current. In energy harvesting applications, energy loss in the from leakage current will be a bigger disadvantage.

Energy storage in energy harvesting is crucial; there is a need for energy storage that can address challenges above. Typical energy storage for AASHM should be capable of working at different temperatures with minimal energy loss. One such system is discussed in the next chapter.

5. Hybrid Energy Storage

Batteries and supercapacitors are popular choices of storage device for conventional WSNs without energy harvesting, but as discussed in Chapter 5, neither represents the ideal solution. Supercapacitors possess low energy density while batteries have low power density. When using a battery-only solution for storage, the runtime of a sensor node is typically reduced by the battery's relatively high internal impedance and other internal losses. Supercapacitors can overcome some of these problems, but generally, do not provide sufficient long-term energy to allow advanced health monitoring applications to operate over the extended period is necessary. Supercapacitors have complementary characteristics to batteries and vice versa, therefore using them in a parallel combination can be complimentary. A number of researchers are undertaking both theoretical and experimental studies to demonstrate that hybrid energy, as shown in Figure 5.1, is a possible solution for wireless sensors (Smith, Mars et al. 2002). However, despite extensive work done with hybrid energy storage units, their advantages and disadvantages have not been thoroughly analysed in low-power wireless sensors and in particular, performance when combined with energy harvesting. To fully evaluate the value of including supercapacitors in hybrid systems is a major task.

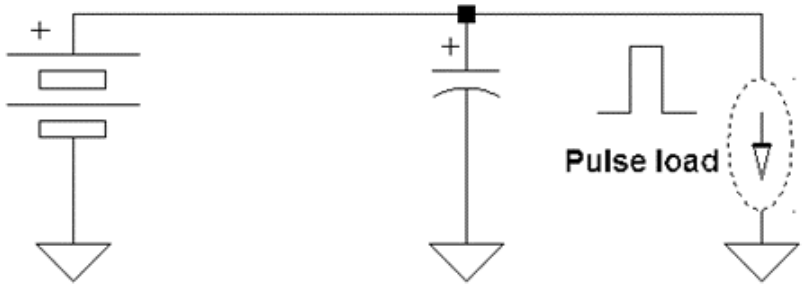

Figure 5. 1 Hybrid Energy Storage in Parallel Connection

The idea of using hybrid energy storage for WSN was developed originally for the automotive industry (Anthony US Patent 2006). Here, large supercapacitors were used, placed across batteries to match the high current demand from speakers for large base or heavy drum beat. This scenario is analogous to the high current demand for the *node-idle* and *transmission* functions of a WSN. Although normal ceramic capacitors can be used as buffer capacitors for hybrid systems, the supercapacitor is preferred in aircraft applications for their operating capability in the different temperature range.

A hybrid energy storage solution can provide both energy and power density to a WSN as shown in Figure 5.2. The common definition of an efficient energy storage system for a WSN is a storage unit that can provide longer run-time (Penella and Gasulla 2010).

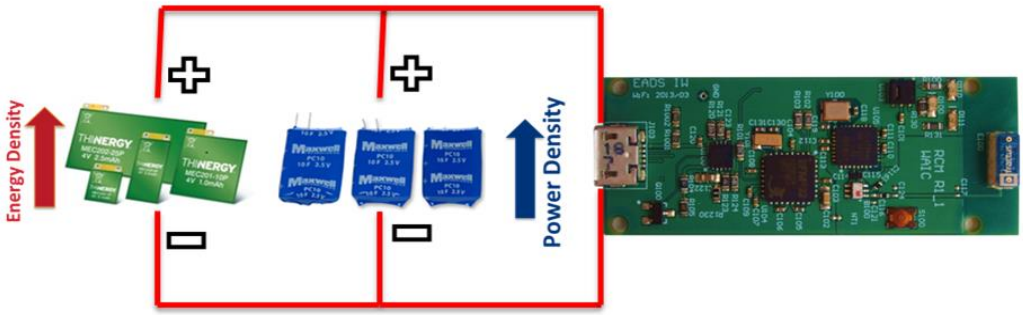

Figure 5. 2 Overview of Hybrid energy storage with WSN

Longer WSN run-times can be achieved by using batteries with higher energy density. However, because of the high associated internal impedance or equivalent series resistance (ESR), a significant voltage drop can appear, as explained in chapter 5.

The voltage drops developed across the internal resistance of the battery prevents access to all the available charge, thus leading to a reduction in the runtime of the WSN. One way to decrease the batteries' internal resistance is to increase the surface area available for the chemical reaction within the battery. However, the disadvantage is this leads to a reduced energy density and higher leakage, which again decreases the runtime. From the Characterisation conducted and presented in this thesis, it is understood that the battery's ESR increases with reducing temperature, leading again to potential run-time reduction.

Unlike batteries, supercapacitors do not have high ESR and associated voltage drops, and as a result, can provide longer run-times for a conventional WSNs. High capacitance (> 1 Farad) supercapacitors need to be used to store sufficient energy. As capacitance increases, it should be remembered that the leakage current, ESR and weight will also increase, and this is considered as a drawback.

In (Holland, Weidner et al. 2002), an experimental approach was proposed for calculating the optimal value of C capacitance, to be added in parallel to the battery in a hybrid system. A series of equations were theoretically derived, which were used to compare the voltage developed across a load against the internal resistance of the battery. Battery technologies with lower ESR such as NiMH do not generally benefit by having a parallel supercapacitor connected across them. In AASHM applications, a battery's ESR varies with temperature, so it would be difficult to adopt the proposed equations of Holland. In (Dougal, Liu et al. 2002) power and life extension under pulsed--load conditions for a hybrid system is theoretically analysed, but no experimental results were provided. Both papers discuss conventional WSNs without energy harvesting. For AASHM applications, energy storage is a crucial part of the system and energy stored during the times of inactivity can be used to power the WSN later in the flight cycle for example. The Energy loss in the form of internal impedance in a battery or leakage current in a supercapacitor is not acceptable, so the selection of storage elements is mainly made based on the needs of the application. The WSNs used in aircraft applications use low power sensors and need to be powered from locally harvested energy. The amount of energy storage required is basically calculated depending on the power level and time required for the application. The stored energy can be equally divided between battery and supercapacitor in the hybrid system. From chapter 4 however, it is understood that the leakage current is higher in a supercapacitor, so it is desirable to minimise the amount of energy stored in the supercapacitor. The battery, with higher energy density and lower weight, will be a possible option to store more energy in the hybrid system. Figure 5.3 shows an assembled hybrid storage unit for testing.

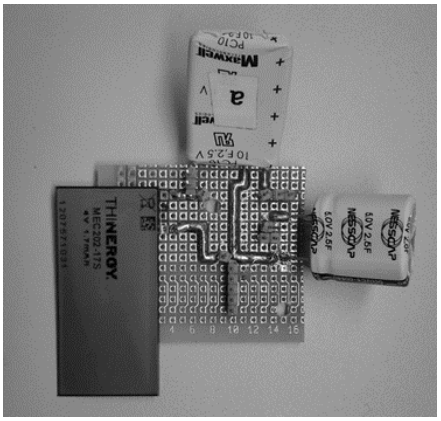

Figure 5. 3 Assembled storage units showing two supercapacitors and a battery

5.1 Characterisation of Hybrid Energy Storage

In the average energy consumption of a strain wire sensor was measured as 40 J, and based on this value, a battery and supercapacitor were selected. A comparison was made between two storage units comprising of two series connected Maxwell PC-10 series supercapacitors yielding an overall capacitance of 5.54 F, and a hybrid energy storage unit comprising a single Nesscap 2.4 F supercapacitor in parallel with a MEC202 1.7 mAh thin-film battery. The combination of LIR 2450 and Nesscap 1.5 F was not tested in hybrid combination, as LIR 2450 standard Li-ion was only chosen to demonstrate switched-energy storage in chapter 6. The exact capacitance values measured using Keysight N6705B is used to calculate the energy. This results in the two energy storage solutions offered similar energy density and similar operating voltages as shown in Table 5.1.

Table 5.1 Comparison of storage units

Storage Unit	Voltage Applied (V)	Energy (J)	Weight (g)
Maxwell PC-10 (2 in series: 5.54F)	4	41.32	12.6
MEC202+ Nesscap	4	44.48	5.975
LIR2450+Nesscap (Possible Combination)	4	1578	10.02

5.1.1 Charging of Hybrid Energy Storage-1(MEC202+Nesscap)

A supercapacitor is charged using a Li-ion battery under various temperature ranges using a climatic chamber. As shown in Figure 5.4 charging profile of the hybrid combination- 1 looks similar to the charging profile of battery. With charge current limited to 25mA, the charging time was lower at positive temperatures. The charging was initiated from 2 V, which was the battery's cut off voltage. However, the hybrid energy storage reaches 4V more similarly to battery charging time, but it took longer time stabilise charge state as shown in Table 5.2. This because the addition of the charging rate of the supercapacitor is restricted to fewer discharges current of the battery.

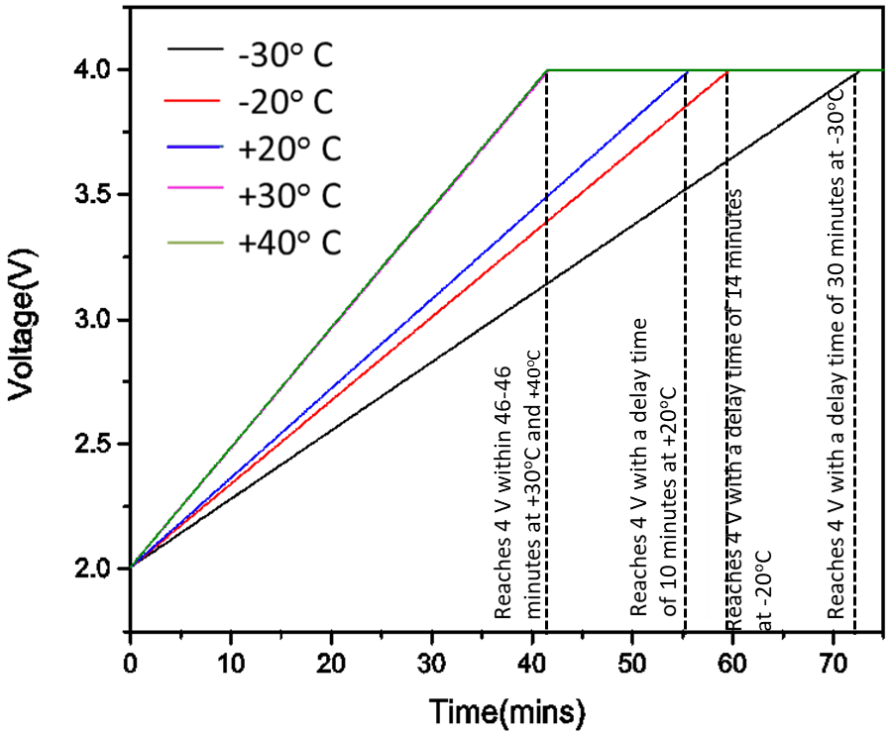

Figure 5. 4 Charging profile of hybrid energy storage at different temperatures

Table 5.2 Charging time of hybrid storage unit at various temperatures

Temperature ^{o}C	Time (minutes)
+40^{o}C	44
+30^{o}C	46
+20^{o}C	56
-20^{o}C	60
-30^{o}C	74
-40^{o}C	Charging not initiated

5.2 Runtime Extension of a WSN

To demonstrate that a hybrid storage unit can increase the runtime of a sensor node, the comparison between equivalent storage units was made under the same pulsed-load conditions that are used for the above, single element experiments.

The hybrid combination of MEC202 + Nesscap 2.4 F has 3 Joules more energy capacity than that of the Maxwell PC-10 (two in series with a total capacitance of 5.54 F). In addition, the weight of the hybrid system is almost half the weight of the supercapacitor only solution which is an important advantage of the hybrid. This comparison is summarised in Table 5.2.

The LIR2450 + Nesscap were not considered for this experiment because their total energy density of hybrid 2 combinations is 1470 J. To match that energy joules supercapacitor of 183 F is required. For an increase in supercapacitor Farad considerably the weight and ESR, leakage current will in also increase.

To determine the period over which the WSN could be powered by each storage unit, a discharge cut-off voltage of 2.5 V was assumed below which the WSN would not operate reliably. This value was based on the fact that most of the commercially available WSNs include a microcontroller, which typically has lower operating voltage limits of 2.2 V.

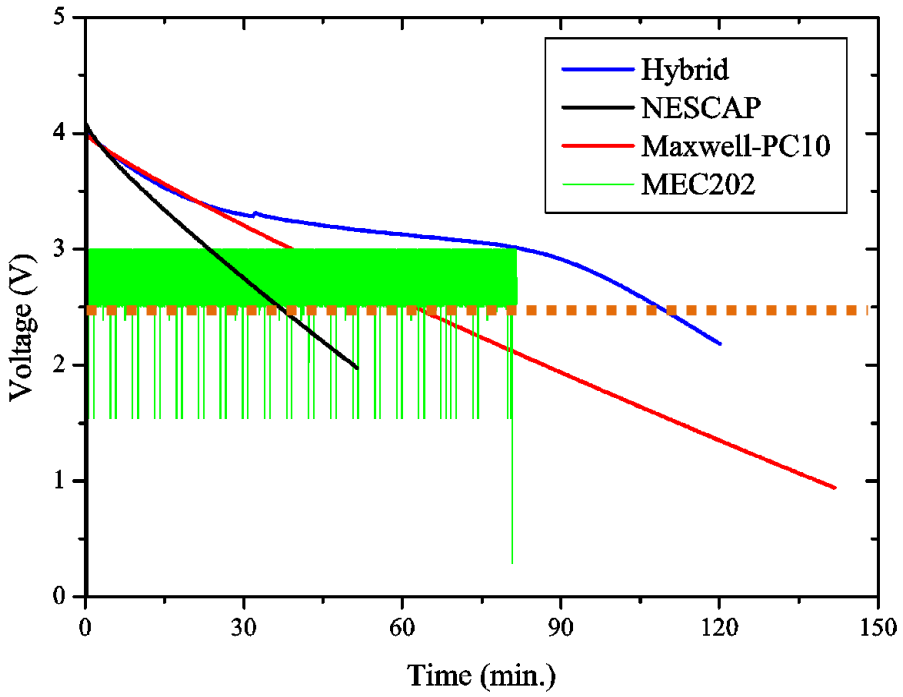

Figure 5. 5 Comparison of discharge curve for storage units (MEC202 battery, Maxwell, Nesscap Supercapacitor, MEC202+Nesscap – Hybrid) at -20^{o} C in the pulsed-load setup the thick dashed line indicates minimum operating voltage threshold.

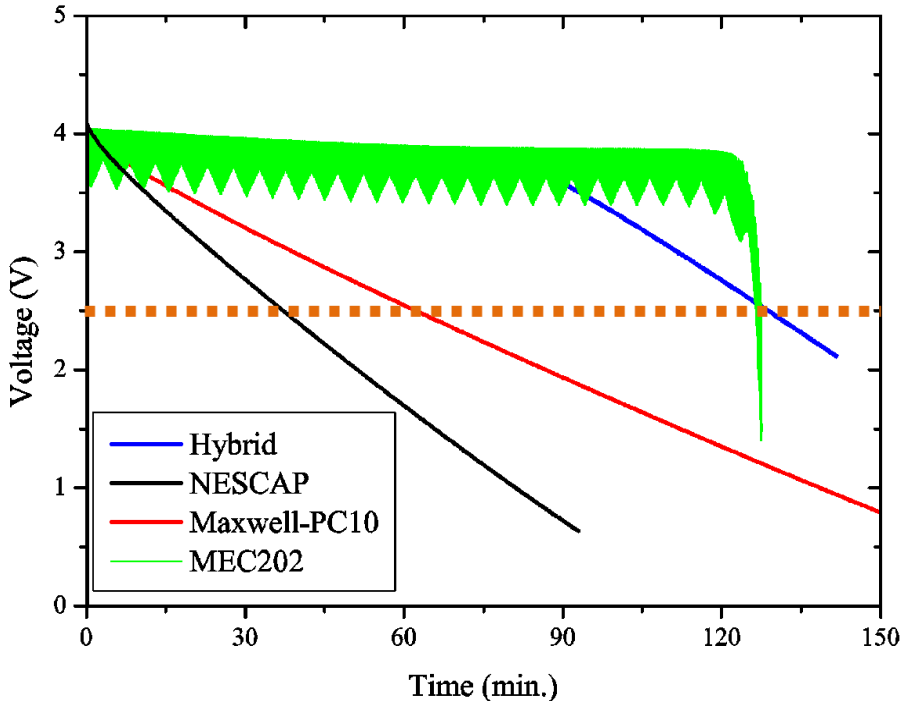

Figure 5. 6 Comparison of discharge curve for storage units at +20^{o}C in the pulsed-load setup the thick dashed line indicates minimum operating voltage threshold.

Figure 5.5 & 5.6 shows the discharge properties of the different storage elements, at -20°C and +20°C. At the higher temperature, the MEC202 can be seen to have the better performance, with nearly 130 minutes operation time compared to 62 minutes for the Maxwell and 46 minutes for the Nesscap. At the lower temperature, the MEC202 battery clearly cannot function correctly, and does not achieve the charge voltage, limiting at just over 3 V. For both temperatures, there is an abrupt collapse in the MEC202 voltage at different points of the discharge curve (3.8 V at +20°C and 2.8 V at -20°C). The hybrid system has over 120 minutes of operational time at +20°C and over 110 minutes at -20°C.

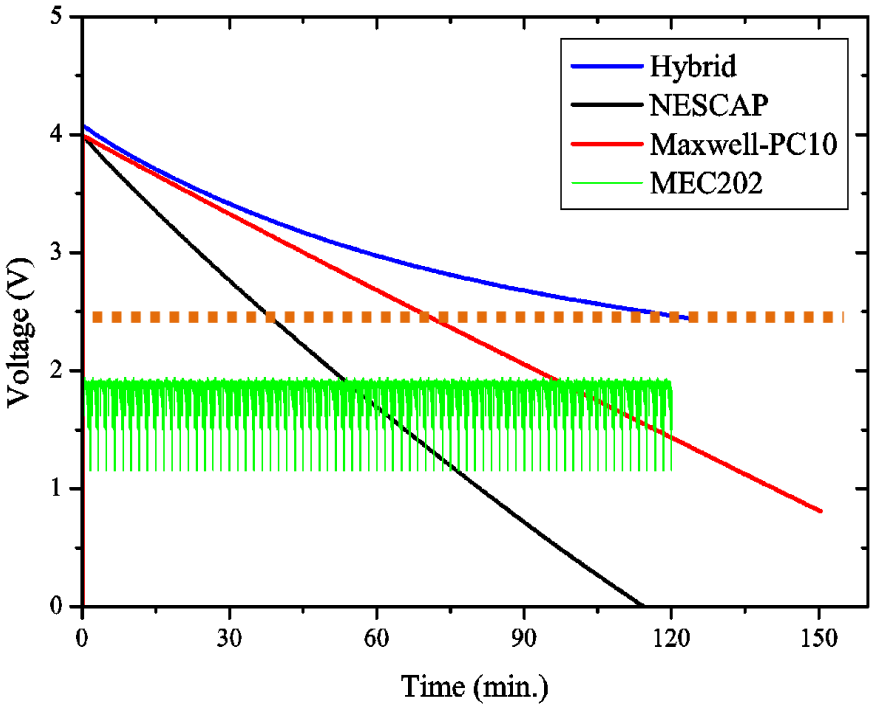

Figure 5. 7 Comparison of discharge curve for storage units at -30° C in pulsed-load setup - thick dashed line indicates minimum operating voltage threshold

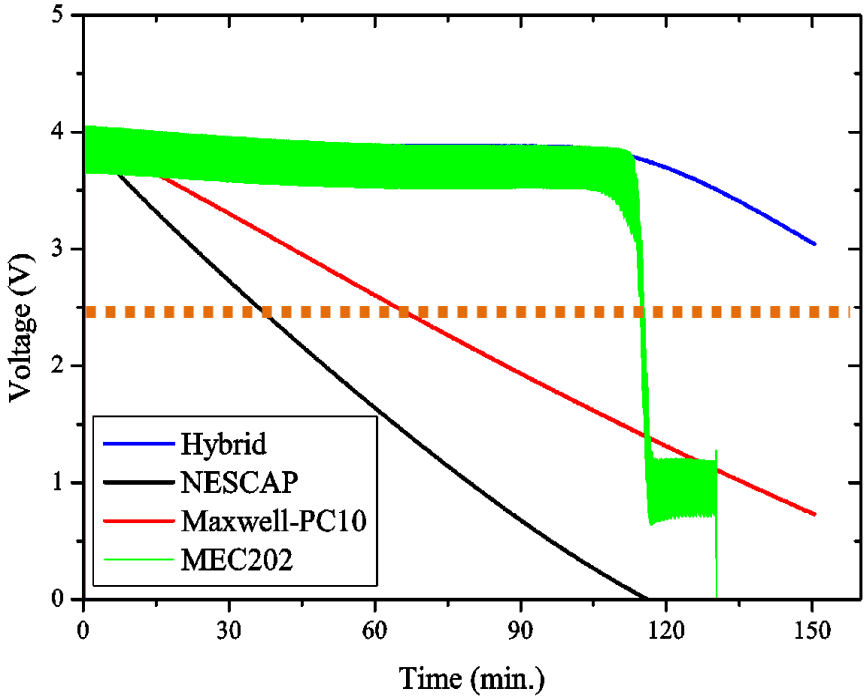

Figure 5. 8 Comparison of discharge curve for storage units at +30° C in pulsed-load setup - thick dashed line indicates minimum operating voltage threshold

Figure 5.7 & 5.8 show the discharge properties of the different storage elements, at -30°C and +30°C. At +30°C the MEC202 battery has 110 minutes of operation time compared to 70 minutes for the Maxwell and 40 minutes for the Nesscap. At 30°C the MEC-202 battery has a voltage drop which is higher and collapses at 1.8 V. The hybrid system has over 150 minutes of operation time at +30°C and over 120 minutes at -30°C.

Finally, Figure 5. 9 & 5.10 show the discharge properties of the different storage elements at -40°C and +40°C. At +40°C, the MEC202 can be seen to have a better performance, with nearly 140 minutes of operation time compared to 65 minutes for the Maxwell and 35 minutes for the Nesscap.

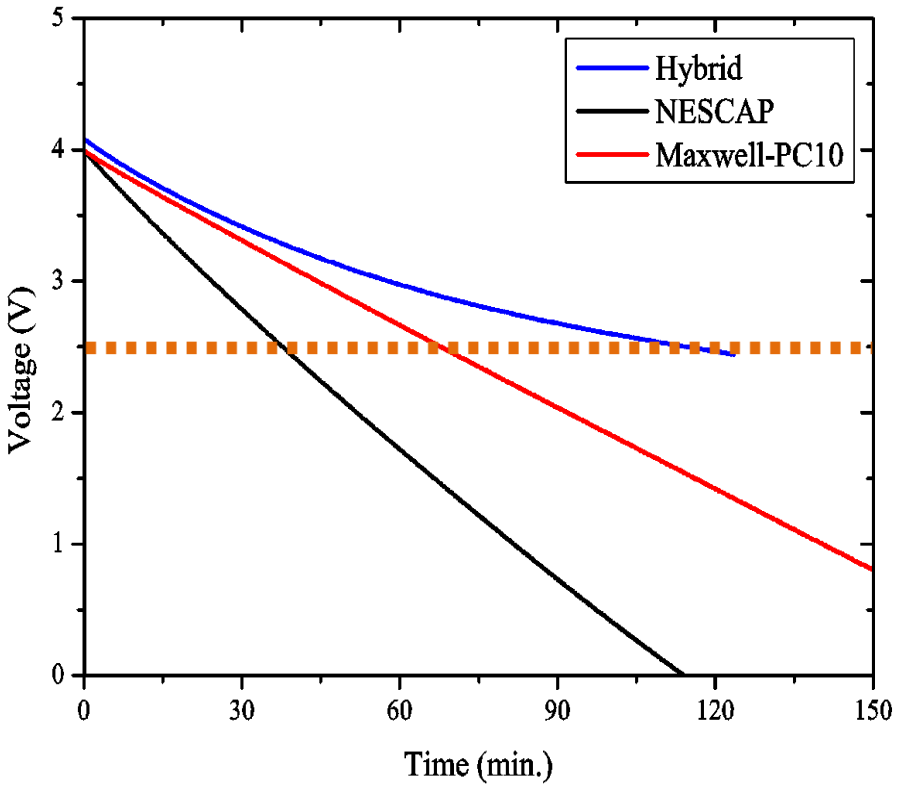

Figure 5. 9 Comparison of discharge curve for storage units at -40°C in pulsed-load setup- thick dashed line indicates minimum operating voltage threshold

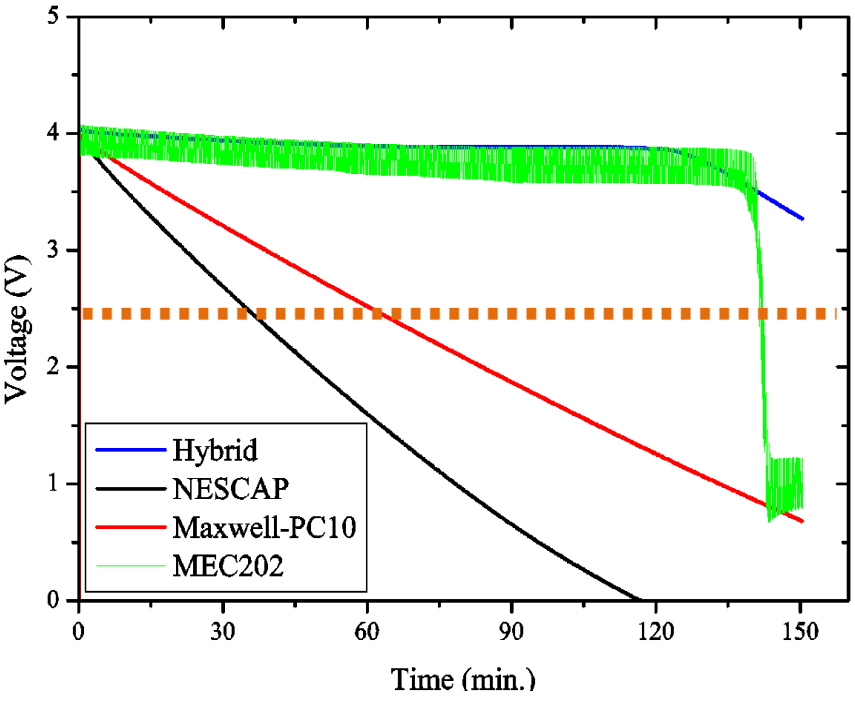

Figure 5. 10 Comparison of discharge curve for storage units at - +40°C in pulsed-load setup- thick dashed line indicates minimum operating voltage threshold

At -40^{o}C, the MEC202 battery does not function at all, with the experiment being repeated to confirm this result. The hybrid system operates for over 150 minutes at +40^{o}C and over 120 minutes at -40^{o}C.

At higher temperatures, the MEC202 can be seen to have the better performance, because higher temperatures increase the mobility of the ions in the electrolyte, which results in a lower internal resistance, which in turn increases the effective capacity of the battery. At lower temperatures, the MEC202 battery clearly cannot function correctly and does not achieve the charge voltage. For negative temperatures, there is an abrupt collapse in voltage at different points of the discharge curve. This is because the increased internal resistance of the battery leads to reduced capacity. At -40^{o}C the battery does not function at all, and the experiments were repeated to confirm this. It is concluded that the MEC202 cannot be used as a stand-alone storage unit for this application. The Nesscap 2.4 F, 5 V supercapacitor has a reduced rapid discharge due to its smaller overall capacitance, and it has been selected only to be used as part of the hybrid storage unit. Both supercapacitors are clearly less affected by the temperature range, discharging at more or less same rate for both conditions, demonstrating that supercapacitors have better performance than batteries in negative temperatures. Finally, at all the temperatures within the test range, adding a supercapacitor in parallel to the battery significantly increases the runtime of the WSN.

For the hybrid units, the discharge performance is significantly better than for the Maxwell PC10 supercapacitor and MEC202 battery acting alone. The hybrid system slowly discharges to approximately 3.25 V as shown in Figure **5.**16 and the discharge rate is steep (like a supercapacitor) as the battery reaches its discharge threshold voltage. Large voltage drops on the battery are eliminated using the supercapacitor in parallel to the battery, which in turn produces a steady discharge from the storage unit. Finally, the runtime of the WSN is increased by using the hybrid storage unit, over the typical aircraft temperature range. There are two main reasons for this increase runtime of the WSN by a hybrid system, and they are as follows.

5.3 Application to a WSN – aircraft temperature sensor

To confirm the performance of the hybrid storage unit in real-time applications, a performance comparison was conducted between the Maxwell supercapacitor and the hybrid system by powering a temperature and humidity wireless sensor at room temperature.

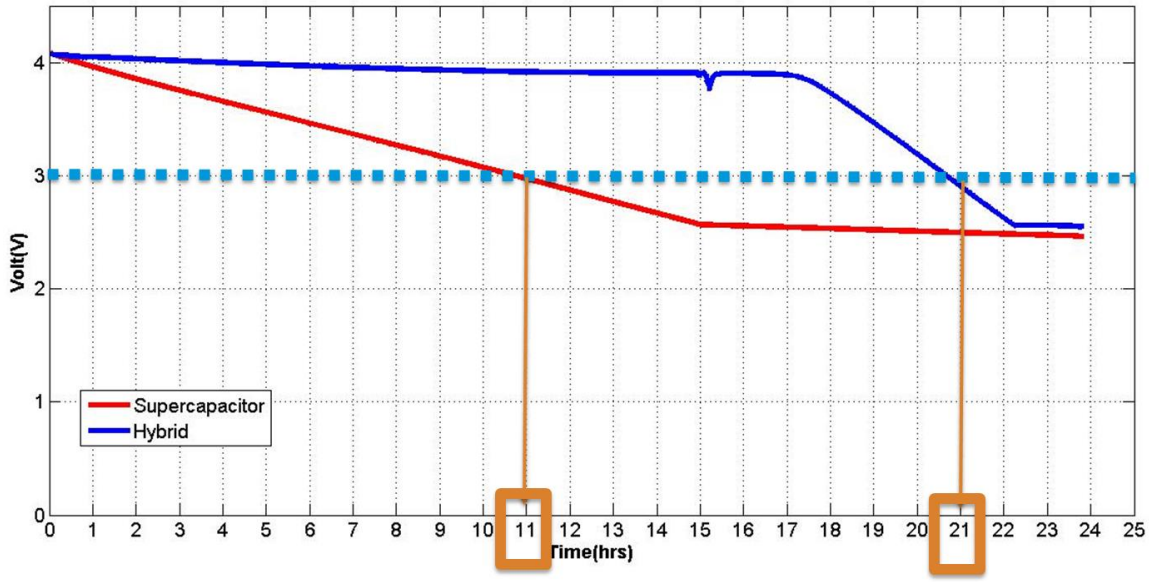

Figure 5. 11 Comparison of discharge curve of supercapacitor and hybrid storage at room temperature (runtime extension of a WSN using hybrid storage unit, the energy stored in hybrid storage is just 3J more than in supercapacitor)

The cut-off voltage for the controller for controlling the temperature and humidity WSN used was 3 V with an 11-mA start-up current. The supercapacitor was able to provide power for 11 hrs. The MEC202 was not able to provide the start-up current, however, by adding a supercapacitor in parallel, this problem was solved increasing the runtime of the WSN to 21 hrs. as shown in Figure 5.15 So in summary with more than approximately3 J, and yet only half the weight of Maxwell PC10, the hybrid system gave over 10 hrs. of runtime extension. From the result presented it can be seen that the significantly increases the runtime of a WSN.

5.4 Critical Analysis on runtime extension of WSN

The supercapacitor acts as a filter and reduces the voltage drop across the battery, which in turn increases the run-time of WSN. As shown in Figure 5.12, the MEC-202 battery has large voltage drops of approximately 0.5V under pulsed-d load discharge. In hybrid mode, the voltage drops are virtually removed, as shown in Figure 5.13 and this is the main reason for runtime extension of WSN.

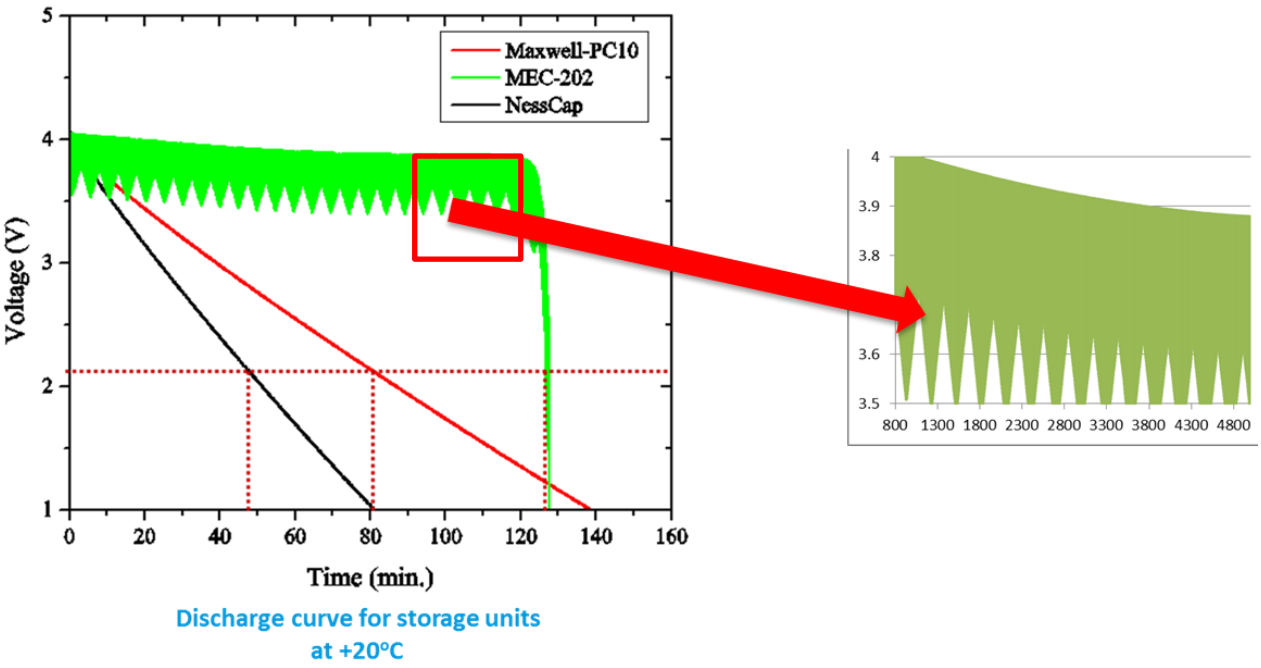

Figure 5. 12 comparisons of voltage drop in battery and supercapacitor storage arrangements

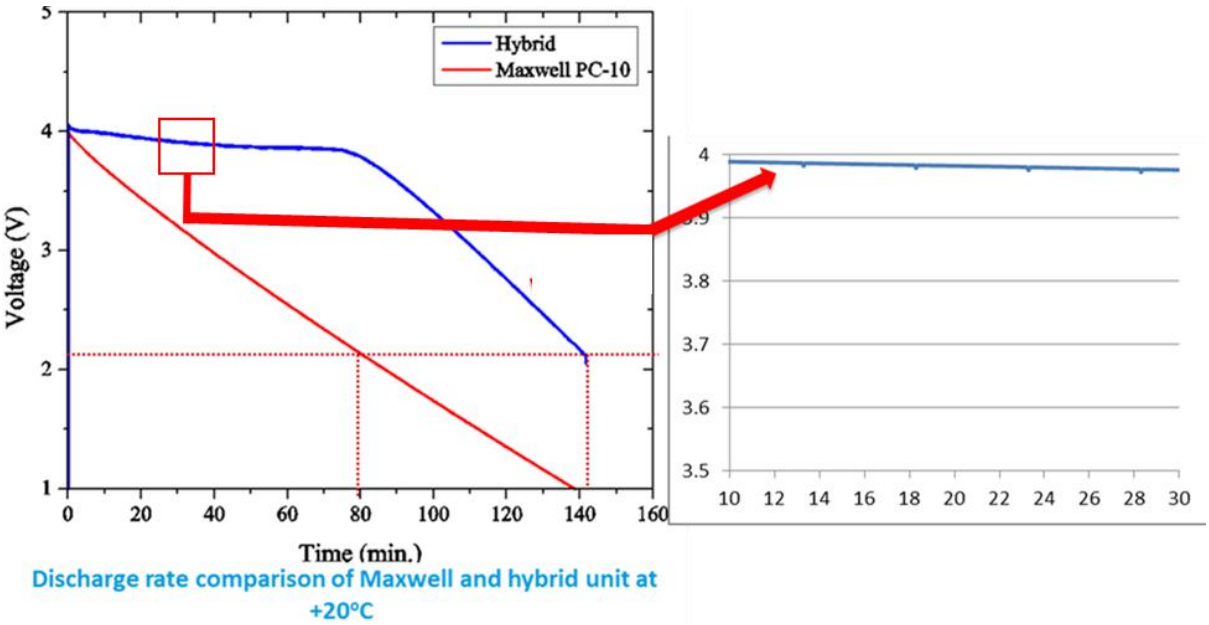

Figure 5. 13 comparisons of voltage drop in battery and hybrid storage arrangements

The cut-off voltages are higher on the batteries compared with the supercapacitor, so the energy stored in the battery cannot be used completely. By adding the supercapacitor in parallel, the cut-off voltage of the battery is increased. In battery alone mode, once the discharge reaches 2.8 V, an immediate drop is shown in Figure 5.14. By discharging the battery below its cut-off voltage, the cycle-life of the battery is reduced. But in hybrid mode, the storage unit has a smooth and controllable discharge until 2.1 V as shown in Figure 5.15. This also explains the reason for a runtime extension of a WSN in hybrid mode.

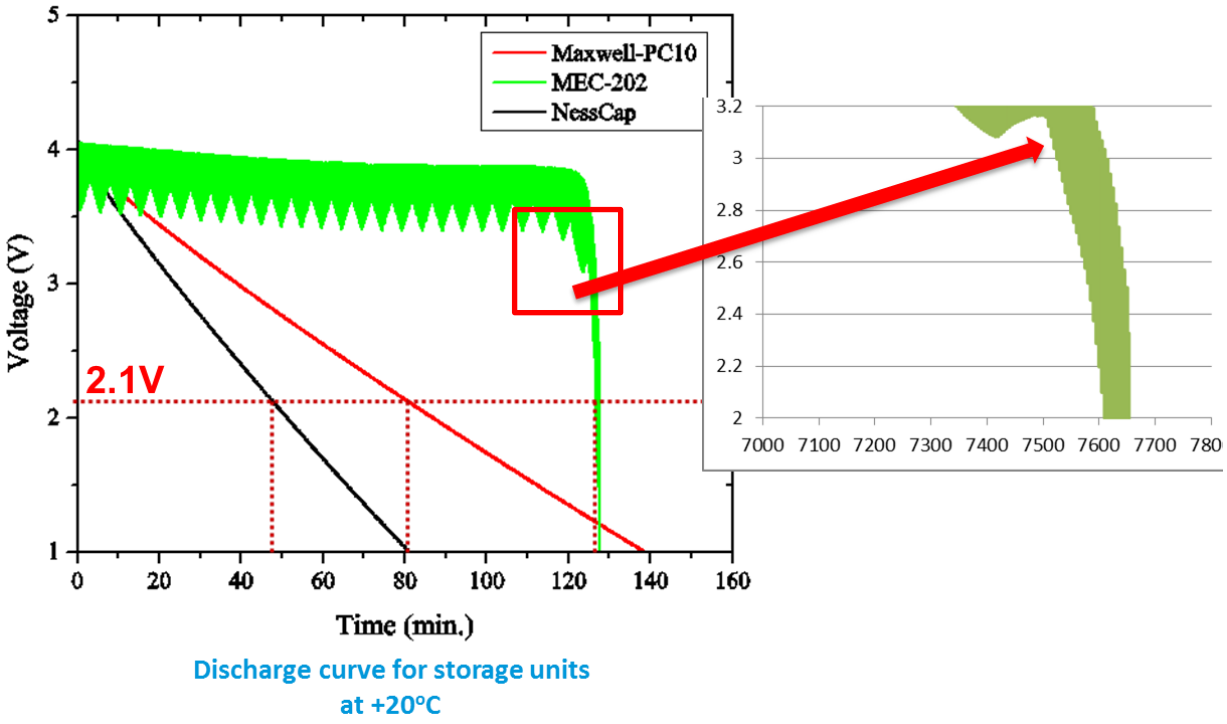

Figure 5. 14 Extension of batteries cut-off voltage in battery

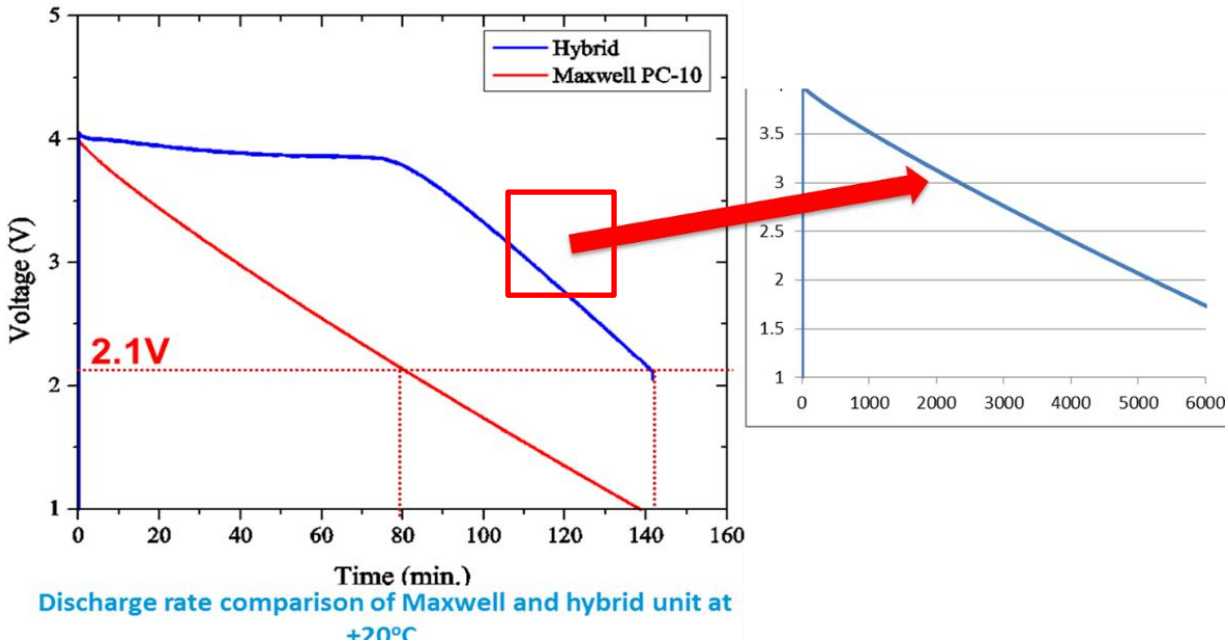

Figure 5. 15 Extension of batteries cut-off voltage drops in hybrid arrangement

5.5 Chapter Conclusion

It has been shown that the thin-film MEC202 battery is not suitable as a stand-alone storage element for a WSN due to its relatively high internal resistance (approximately20 Ω), lower capacity 1.7 mAh and poor performance at lower temperatures (from -20^{o}C to -30^{o}C) becoming unusable at -40^{o}C. The LIR2450 battery with higher energy density has less cycle-life; under the pulsed-load condition, the voltage drops increases the temperature decreases. The Maxwell PC-10 2 in series with a total capacitance of 5.54 F supercapacitor was not affected by temperature in the range of -40^{o}C to +40^{o}C. The Nesscap 2.4 F has very low ESR of 0.042 Ω, but lower capacity and it was characterised to be used in the hybrid storage unit. A hybrid system-1 consisting of a MEC202 battery plus Nesscap supercapacitor was compared with two Maxwell supercapacitors in series and was demonstrated to provide approximately 3 J more energy at almost half weight whilst significantly increasing the runtime of a typical WSN based on temperature and humidity measurement. The hybrid system-2 consisting of LIR 2450 plus Nesscap supercapacitor weighs 10 g can be able to store energy 1574 J. This combination does not serve the purpose of weight reducing by hybrid energy storage. The large voltage drops on the battery are eliminated using the supercapacitor parallel to the battery, which in turn gives steady discharge characteristics and increases the cut-off voltage of the MEC202. These are the reasons for the runtime extension for WSN using the hybrid storage unit. The hybrid energy storage does not provide a complete solution for AASHM, and the disadvantages of this system are discussed in next chapter.

6. Efficient Switched-Energy Storage

6.1 Overview

A simple battery-supercapacitor hybrid is an intuitive way of reducing the effect of load fluctuation on the supplied voltage level. The addition of a supercapacitor connected in parallel can be considered as a low pass filter that prevents rapid or transient voltage changes, as shown in Figure 6.1. The battery-supercapacitor hybrid is thus effective in mitigating the rate capacity effect for intermittent (rather than continuous) high load current as shown in Figure 6.2. The supercapacitor (Seah, Eu et al. 2009) helps with the short duration; high amplitude loads current spikes, which subsequently results in the increase of WSN runtime extension powered by simple battery-supercapacitor hybrid storage.

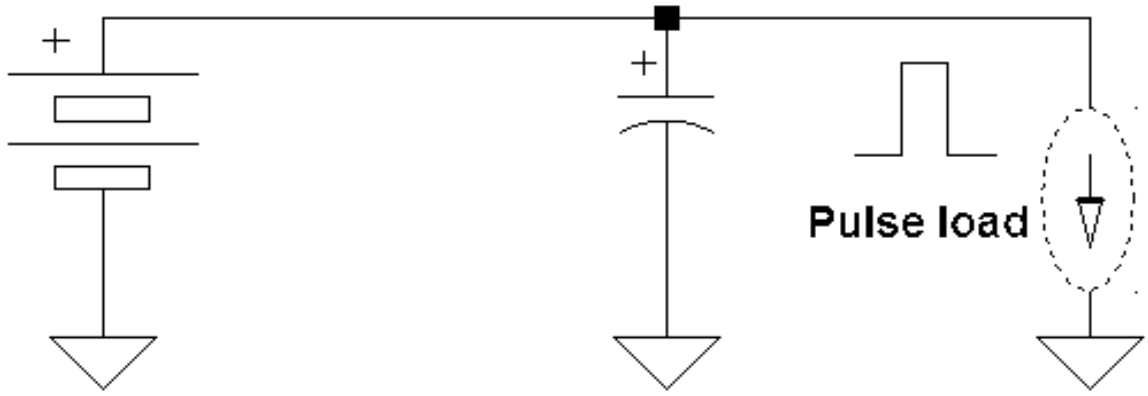

Figure 6. 112 Simple hybrid Energy Storage in Parallel Connection

Although a larger capacitance results in better filtering effect, the parallel arrangement has limited ability to reduce the rate capacity effect in the Li-ion battery as shown in chapter 4, any significant increase in capacitance will add weight to the hybrid storage unit and also brings in disadvantages such as high ESR and leakage current.

.

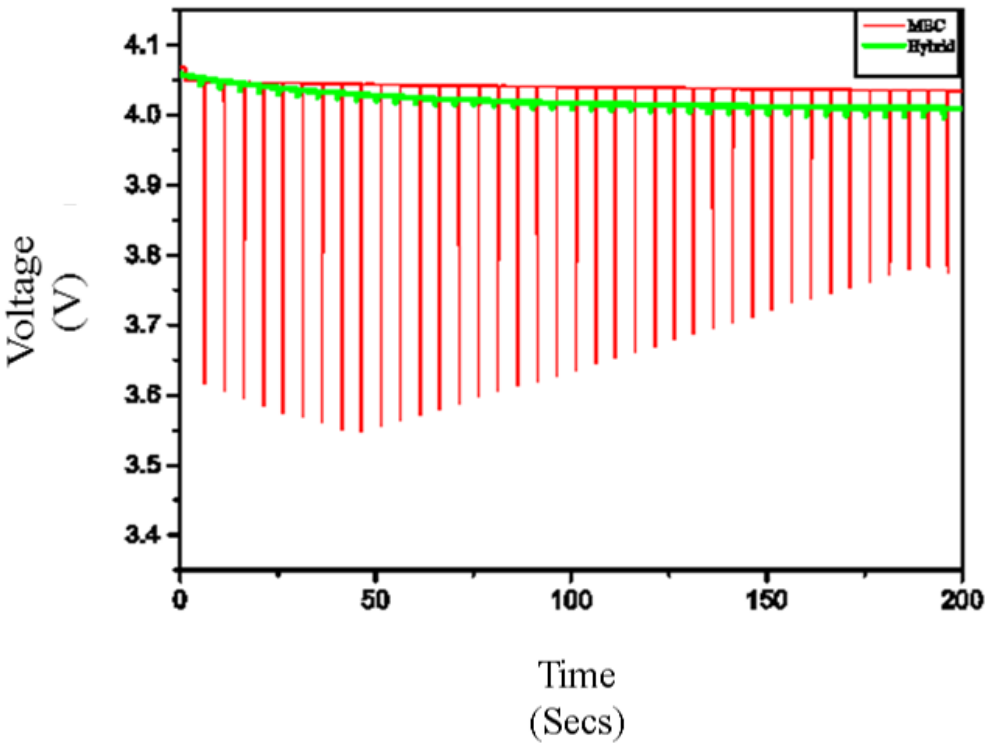

Figure 6. 13 Discharge curve of battery and simple hybrid Storage Unit under Pulsed-load Condition at different temperatures

A hybrid energy storage unit can provide both energy density and power density to a wireless sensor node (WSN). However, the high leakage current of supercapacitors can be a significant disadvantage in hybrid systems utilising a simple, parallel connection of storage components. A second disadvantage relates to the life cycle of the storage units and the fact that batteries can tolerate significantly fewer charge cycles than supercapacitors before degradation. In a simple hybrid storage system, the battery reaching its life cycle limit can reduce the effectiveness of the system, as it then has to be replaced. In (Kuperman and Aharon 2011) an experimental approached was proposed to make the battery the primary energy storage element, with the supercapacitor providing temporary energy storage. Batteries and supercapacitors are separated using solid-state switches. The supercapacitor will power the WSN and will be charged with the battery when the supercapacitor voltage drops below a threshold voltage level.

There is no controlled charging between the supercapacitor and battery as they are just separated by the switches. Increase in energy consumption and cost by adding switches will also be an added disadvantage to this system has to be considered. In (Ongaro, Saggini et al. 2012) explains an energy storage system with a combination of battery and supercapacitor, with both battery and supercapacitor being charged separately with two separate DC-DC converters connected with a common dc bus. This method could be suitable for photovoltaic energy harvesting with a vast amount of solar energy available energy conversion using two DC-DC converters are feasible.

There are several problems (Simjee and Chou 2008) that must be addressed in order to develop an efficient energy storage system.

- The nominal voltage of the battery should be more or less equal to the supercapacitor charging voltage.
- The charging current and the terminal voltage of the supercapacitor should be carefully controlled to achieve efficient and suitable operation.
- The terminal voltage of the supercapacitor must thus be maintained within a proper range in order to meet the load power demand.

6.2 Characterisation of switched-energy storage

To maintain the system in suitable operational condition, the optimal charging current and initial terminal voltage of the supercapacitor must be obtained. Constant voltage charging is used mainly for charging Li-ion batteries. Constant-voltage (often called constant-potential) chargers maintain nearly the same voltage across the battery throughout the charging process, regardless of the battery's state of charge. The (Gao, Dougal et al. 2005) DC-DC boosters used in a power management board will normally provide battery from overcharging. Given this over-charging protection behaviour, constant-voltage chargers are frequently found in applications that normally allow extended charging periods to attain full charge. Constant-voltage chargers should not be used where there is a need for frequent

cycling and charging. Repeated discharges without returning the cell to its full charge will eventually decrease the capacity and may damage Li-ion cell.

6.2.1 Leakage Current

In a simple parallel connection of batteries or of supercapacitors, the leakage current will be proportional to the number of cells, whereas, in a series connection, the leakage current will be same as the single cell (Kötz, Hahn et al. 2006). Also, in a simple parallel combination of battery and supercapacitor, the overall leakage current will increase with temperature as shown in Table 6.1. Figure 6.3 shows the comparison of leakage current of a simple hybrid storage unit at different temperature levels.

Table 6.1 Leakage current of simple hybrid system at various temperatures

Temperature ^{o}C	Average leakage current mA
+40^{o}C	0.12
+30^{o}C	0.098
+20^{o}C	0.096
-20^{o}C	0.094
-30^{o}C	0.092
-40^{o}C	0.089

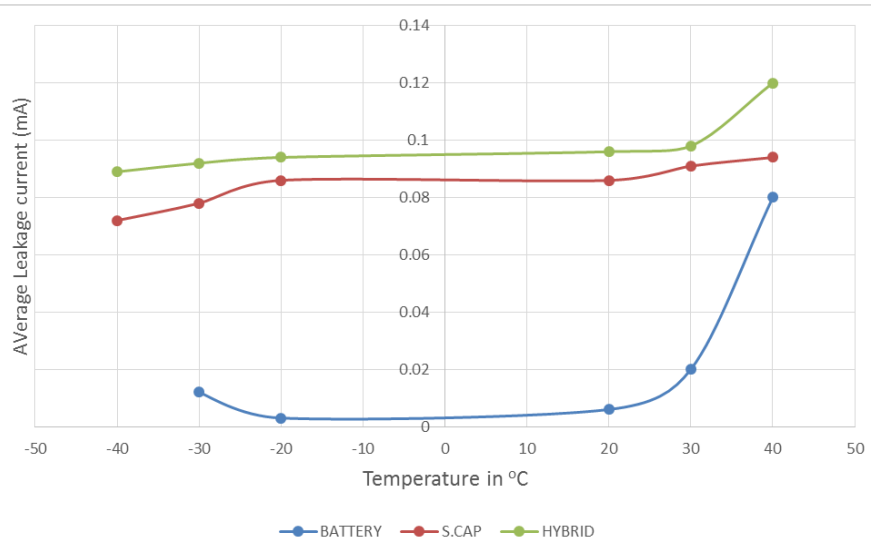

Figure 6. 3 Average leakage current of Li-ion battery, supercapacitor and simple hybrid storage unit at various temperatures

6.2.2 Cycle-Life

Whereas supercapacitors can be charged and discharged virtually an unlimited number of times, batteries have defined and limited cycle-life. Because of this, ageing does not affect the supercapacitor, as it does a battery.

Table 6.2 Average cycle-life of different energy storage

Energy Storage	Average Cycle-life
Li-ion thin	10000
Nickel-metal hydrate	1000
Li-Magnese Dioxide	1500
Li-Polymer	1000
Li-ion Solid State	5000
Nickel-Cadmium	1000
Supercapacitor	> 500000
Hybrid Energy Storage	Depends on batteries cycle-life

Under normal operating conditions for low-power applications, a supercapacitor degrades from the original 100 percent capacity to 80 percent in 10 years. The supercapacitor functions

well at -40^{o}C and +85^{o}C, (Kötz, Hahn et al. 2006) but continuous exposure at lower or high-temperature will affect the efficiency of the supercapacitor as ESR and leakage current are temperature dependent. The cycle-life is one of the major limitation for batteries in WSN application (Du Pasquier, Plitz et al. 2004). The cycle-life of the battery can be prolonged by maintaining batteries discharge cut-off voltage while discharging. The shorter the duration of discharge (DoD), the longer the battery will last.

6.3 Constant current charging (CCC)

When rapid charge time is critical, constant current charging provides the fastest charge method. Constant power charging can transfer all the available power from the charge source into the energy storage capacitors. The LTC4425 was used as constant current charging regulator between the battery and supercapacitor and produced the results shown in Figure 6.4. A pulsed-load representing the *node-idle* and *transmission* states of the strain WSN, as explained in chapter 2.5, was used as the WSN representative load, using channel 1 of the Keysight N6705B DC power analyser. LabVIEW code was written to record the two analogue inputs (ai0 and ai1) of a Nidaq 6211 data acquisition unit. A while loop was used to monitor and detect when the supercapacitor voltage reached 0.8 V when a FALSE condition is set, and a logic high is generated at port-1 of Nidaq 6211 and delivered to the 'enable charging' pin of the LTC4425. This simple code was later developed into the switching algorithm to demonstrate the advantages of switched energy storage. The code generates an array with two columns of voltage measurement from analogue inputs ai0 and ai1 and writes these top an Excel format file. The data was logged at a rate of 1 sample-per-second. One of the important criteria for an ASHM system is that all associated electronics should operate in the range of -40^{o}C to +40^{o}C. The charging of a 0.6 F supercapacitor from an LIR 2450 battery using LTC 4425 was monitored over the temperature range of -40^{o}C to +40^{o}C, in a climatic chamber. The LIR 2450 battery was charged up to 4 V using channel 2 of N6705B when the supercapacitor was discharged under pulsed load conditions.

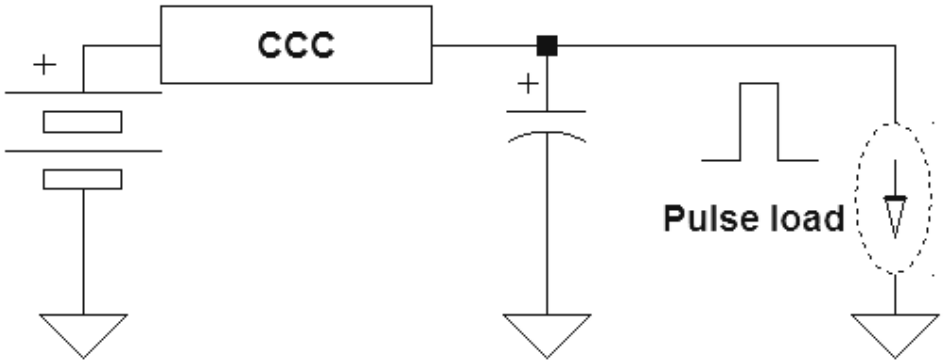

Figure 6. 4 Energy Storage with battery, supercapacitor with constant current charging (CCC)

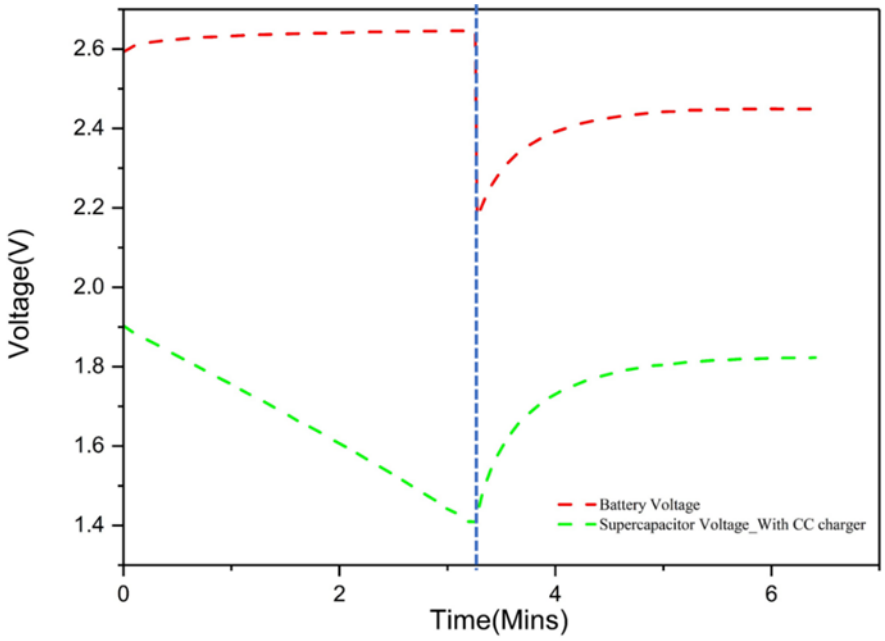

Figure 6. 5 Constant current charging of supercapacitor from thin-film Li-ion battery using the LTC4425, at room temperature

A supercapacitor is charged using a Li-ion battery with a charging control circuit is shown in Figure 6.5. By using a CCC stage between the battery and supercapacitor, the large voltage drops across the battery that are usually experienced in a parallel hybrid system are significantly reduced. The thin-film battery was discharged near its cut-off voltage, to understand the expected voltage drop across the battery, during charging in the worst-case scenario. Unfortunately, the thin-film battery was discontinued, so the experiments over other temperature ranges were conducted using the LIR 2450 standard Li-ion battery.

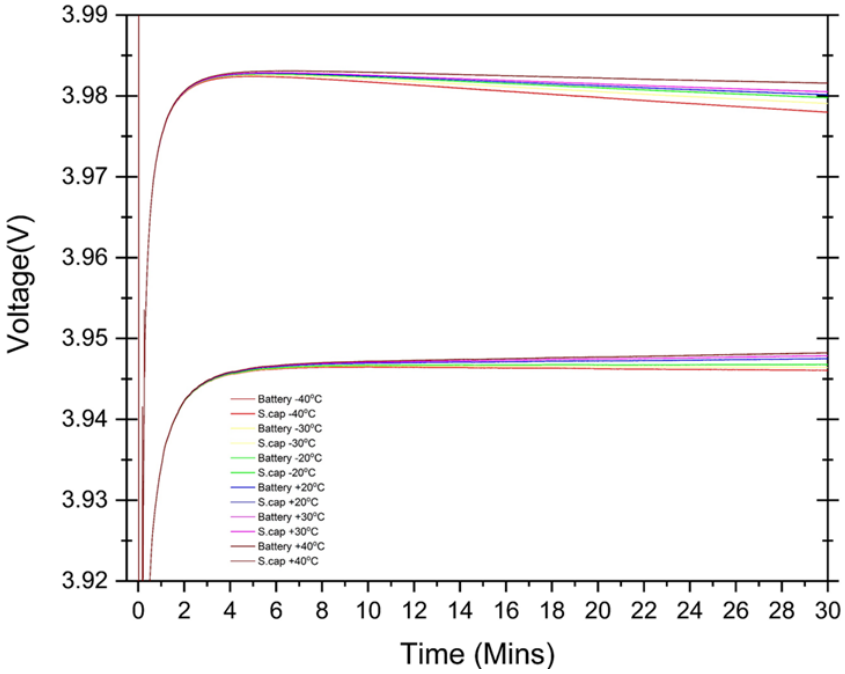

Figure 6. 6 Charging of supercapacitor from LIR 2450 standard Li-ion battery with LTC4425 over a temperature range of -40°C to +40°C in a climatic chamber

As shown in Figure 6.7, once the charging was initiated, the voltage of the LIR 2450 battery dropped to 3.92 V from 4 V and recovered to a constant 3.98 V at all the temperatures monitored.

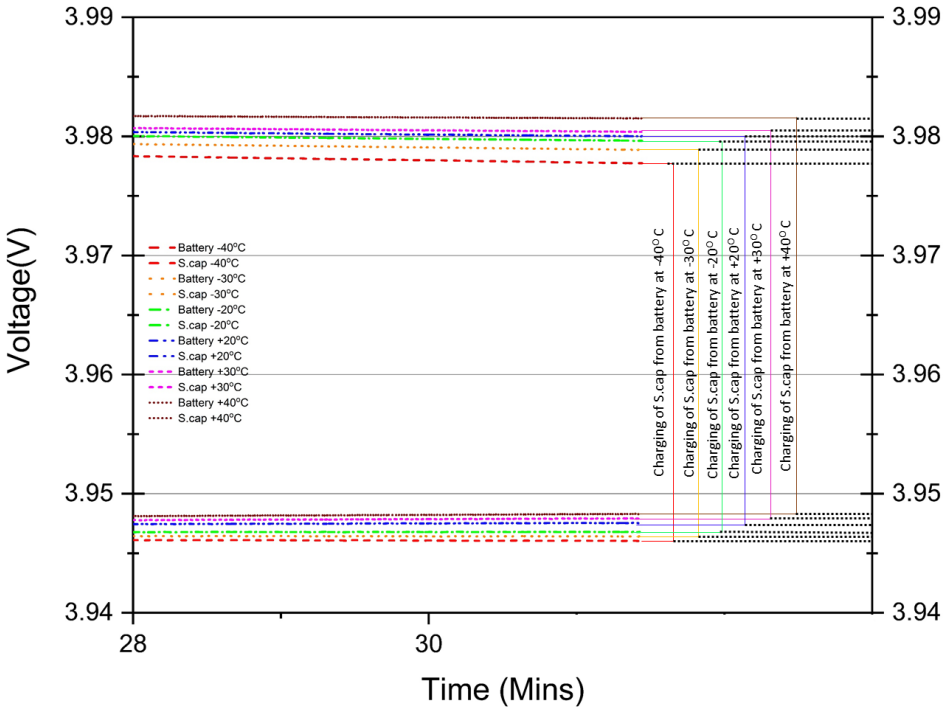

Figure 6. 7 Charging of supercapacitor from LIR 2450 standard Li-ion battery with LTC4425 (this is the same plot as Figure 6.6 but for a compressed time frame)

As shown in Figure 6.7 the supercapacitor charging rate was considerably from 3.9483 at +40°C to 3.94604 at -40°C reduced as the temperature decreases. The decrease in charging rate supercapacitor from batteries at lower temperatures is observed as the internal resistance of battery increases in negative temperature and movements of ions become restricted.

6.4 Step-up Converter

A step-up converter LTC3539 is used at the output of supercapacitor to establish a constant output voltage, as shown in Figure 6.8. A typical operating voltage of any microcontroller may range from 3.5V to 5V and requires an uninterrupted power supply. For these reasons, this step-up converter is used.

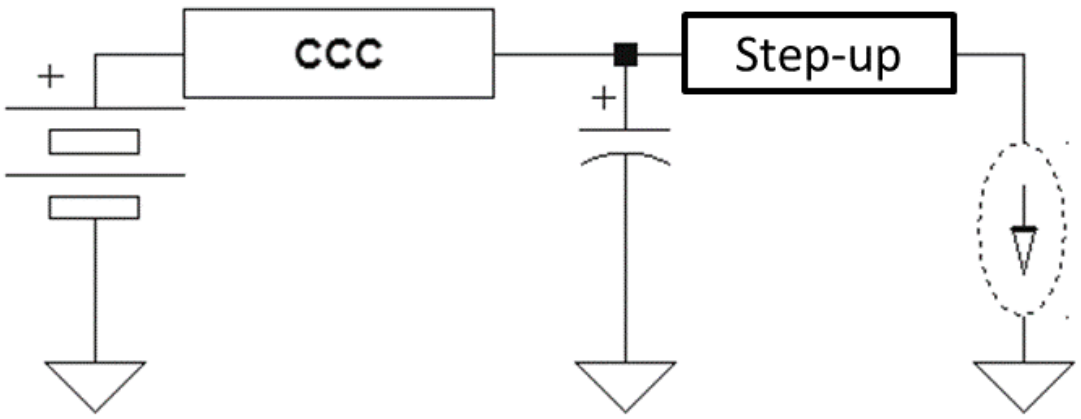

Figure 6. 8 Hybrid Energy Storage with constant current charging and output step-up converter.

The LTC3539 is a commercially available step-up converter that can provide a constant 5 V output with an efficiency level of up to 94%. The LTC3539 was tested with 1.5 F Nesscap supercapacitor, and it performed well over a temperature range of 40^{o}C to +40^{o}C. Using a step-up converter will allow the supercapacitor to discharge to a voltage level of 0.8 V, the minimum input voltage for LTC3539. This means most of the energy stored in the supercapacitor can be used before it needs to be recharged.

6.5 Switched-Energy Storage Controller Architecture

After understanding both the advantages and disadvantages of a hybrid storage approach, an efficient energy storage unit is designed that combines constant current charging (LTC4425) and a step-up converter (LTC3539), as shown in Figure 6.10. In this arrangement, the two main disadvantages of hybrid storage, specifically common leakage current and limited battery cycle-life are minimised by treating the battery and supercapacitor as separate storage elements, while retaining the overall advantages of the hybrid storage approach The values of resistor, capacitor and inductor used in the LTC4425 and LTC3539 arrangement are calculated based on the data sheets from the manufacturer .

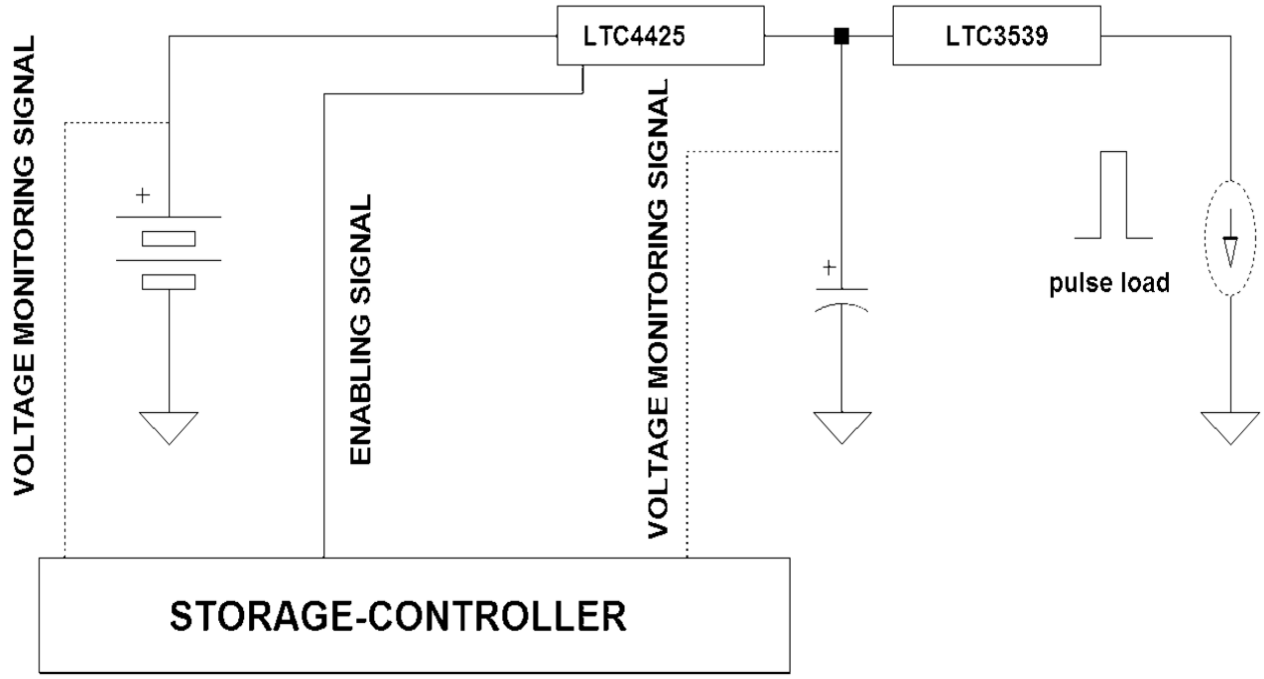

Figure 6. 9 Overview of Switched-energy Storage Unit

The role of the storage controller is extended to monitor the charge and discharge behaviour of battery and supercapacitor storage elements, and to switch appropriately and optimally between the two, improving performance and extending battery life. The enable pin in LTC4425 will be used as a switch for charging control instead of a separate switch.

An experimental Characterisation system has been developed that uses National Instruments data acquisition hardware programmed using LabVIEW as shown in Figure 6.10, to emulate the function of the proposed storage controller. Two analogue input channels ai0, ai1 of a Nidaq 6211 data acquisition unit are used to monitor the discharge voltages from a battery and a supercapacitor. And inside a while loop, once the supercapacitor voltage reaches 0.8 V, which is set as a FALSE condition, the code sends out a digital signal 1 from port 1 of Nidaq 6211 to enable the charging pin LTC4425. When the supercapacitor voltage reaches 4 V, which is set to a TRUE condition the code stops, the code sends out a digital signal 0 to turn off the enable pin in LTC4425.

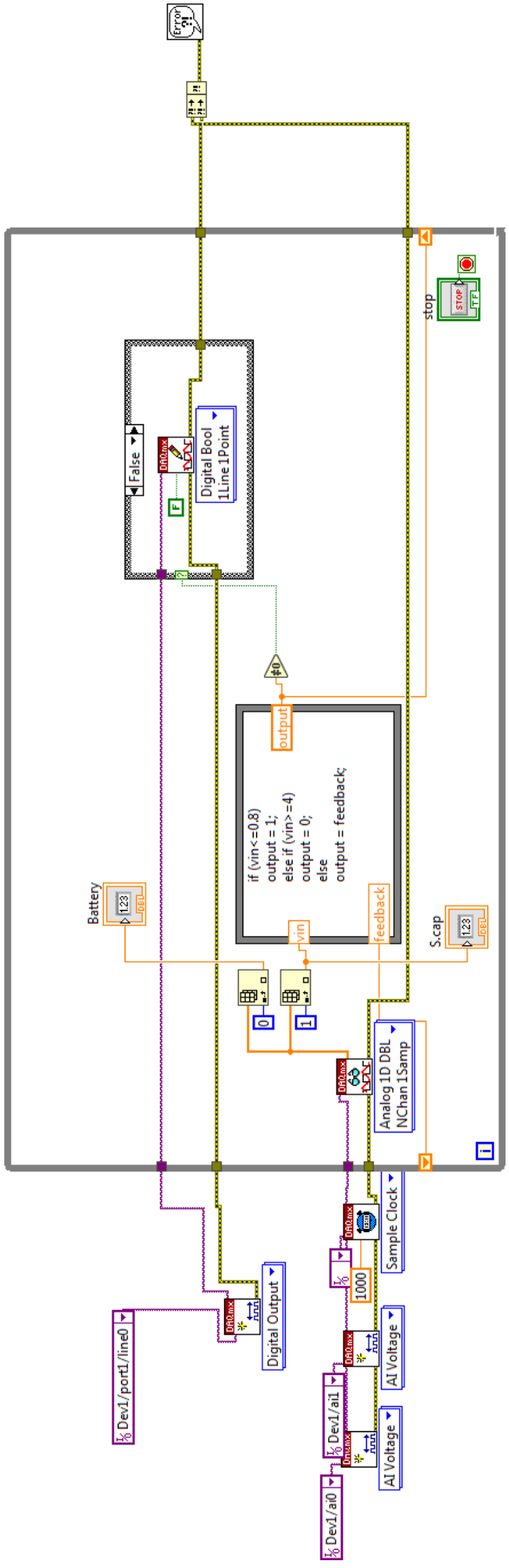

Figure 6. 10 LabVIEW code for switched storage

Figure 6.11 shows a flowchart depicting the algorithm used for switched-energy storage: i.e., as the voltage of the supercapacitor drops below 0.8 V, the LTC4425 charging IC is enabled and allows the supercapacitor to charge the battery. Once the supercapacitor voltage reaches 4V, the LTC4425 is disabled and charging ceases. Importantly, the LTC4425 is also used as a switch to control storage unit selection, avoiding further energy loss through additional external switches. The charging current can be programmed and monitored.

In summary, this improved and easily optimised switchable energy storage architecture can be used to control the frequency of battery charge and to prolong the lifetime of the hybrid energy storage element, without sacrificing overall performance.

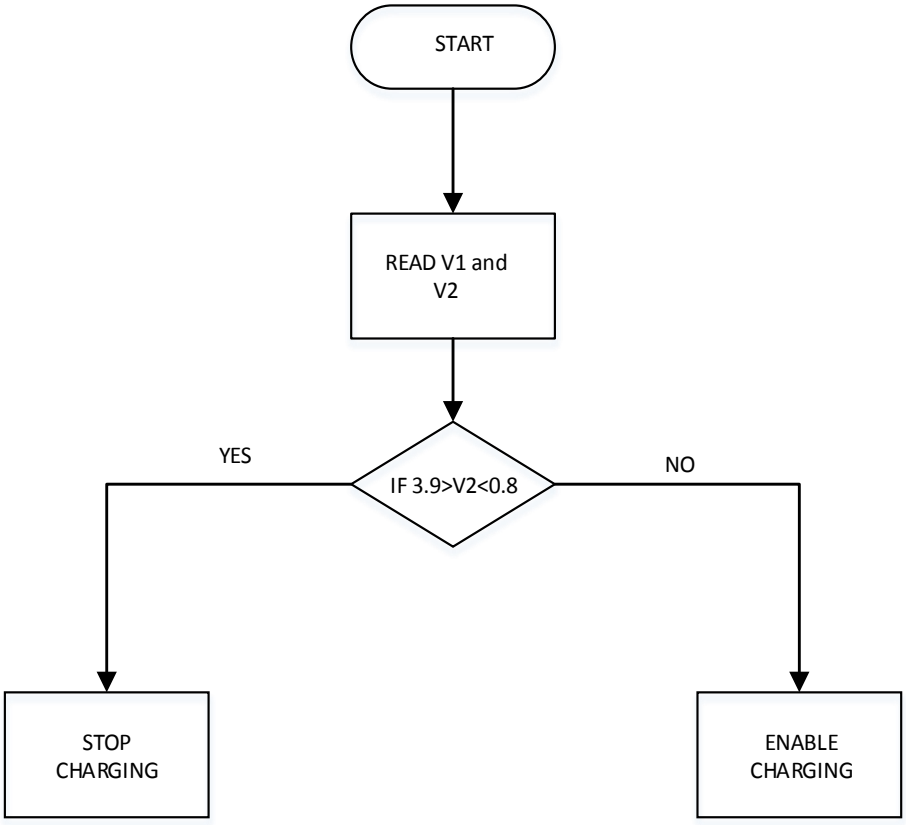

Figure 6. 11 Flowchart control flow for the storage controller.

6.7 Power management circuit with Switched-energy Storage

As mentioned in chapters 3 and 4, power management and energy storage are the two main building blocks for an efficient automated wireless sensing system. By combining experimental observations from studies conducted from chapters 3 to 6, an efficient power management approach with switched-energy storage, that combines the key advantages of batteries and supercapacitors into a single solution was designed and is outlined in this section.

The overall schematic of the proposed power management system is shown in Figure 6.12, and has two energy inputs; one for thermoelectric and the other for vibrational energy harvesting. An LTC3109, dual-polarity DC/DC converter is used to convert thermoelectric harvested energy and an LTC3538, full-wave bridge rectifier with a buck converter is used to convert the vibrational harvested energy. The circuit diagram is divided into a number of different sections (see figures 6.14 to 6.17) for a detailed explanation.

The PWM system comprises two MOSFET solid state relays and can be controlled using a microcontroller or LabVIEW. Relay S1 is single-pole double-throw, and relay S2 is single-pole single-throw. S1 is connected between the two batteries and the supercapacitor charger LTC 4425, S1 double- throw section of the switch will be connected to battery B1 and B2 respectively. The switch S 1 will have an active connection with battery B1 always , so the Enable pin on LTC 4425 will be kept ‘low’ always to avoid charging of supercapacitor through battery b1. S2 is connected between supercapacitor and LTC3539 step-up converter as shown in Figure 6.13. The components used in the power management with switched-energy storage circuit are shown in Table 6.3.

In terms of operation, the circuit has two energy inputs, one for the LTC3109 and the other for the LTC3588 DC-DC converters, that convert the raw energy collected from thermoelectric and vibrational energy harvesters, respectively. The converted energy is stored in batteries B1 and B2 respectively. As explained in section 6.5 detailing the switched-energy storage system, the supercapacitor will power the WSN, and the battery will be used as a primary reservoir energy storage element. The switch S2 connects the two series 1.2 F, 5V Cap-xx supercapacitors to the LTC 3539 step-up converter.

Table 6.3 Components used in the power management board with switched-energy storage

Name	Manufacturer	Description
LTC 3109	Linear Technologies	DC-DC converter for thermoelectric energy harvesting
LTC 3588	Linear Technologies	AC-DC converter for vibrational energy harvesting
LTC 4425	Linear Technologies	Constant current supercapacitor charger
LTC 3539	Linear Technologies	Output step-up converter
Two LIR2 450-standard Li-ion batteries, one for each harvester	Multicomp	Primary energy storage
Two 1.2 F supercapacitor connected in series	Cap-xx	Secondary energy storage
LCA 110	Clare Technologies	S2- switch- Single pole single throw
LCC 2101	Clare Technologies	S1 switch- single pole double throw

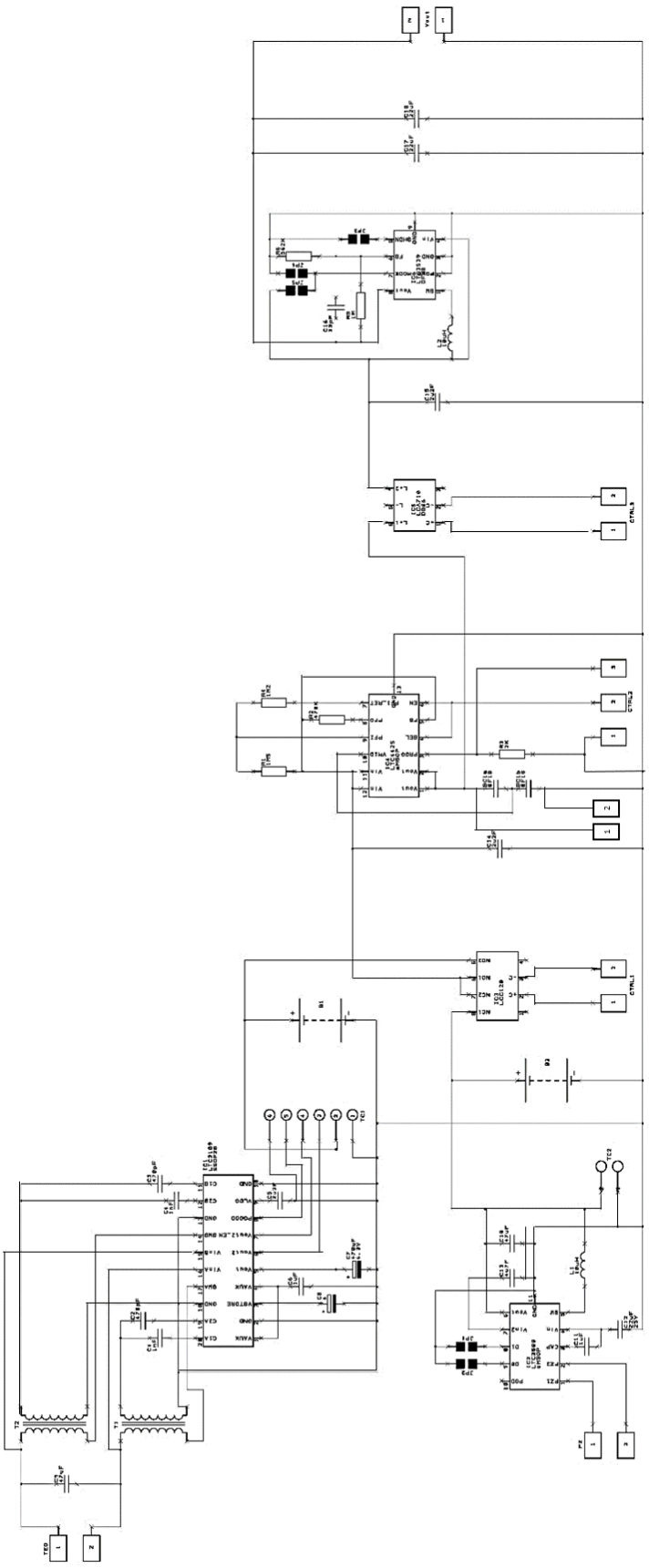

Figure 6. 12 overall view of the proposed power management system with switched energy storage-individual stages discussed in more detail in following sections

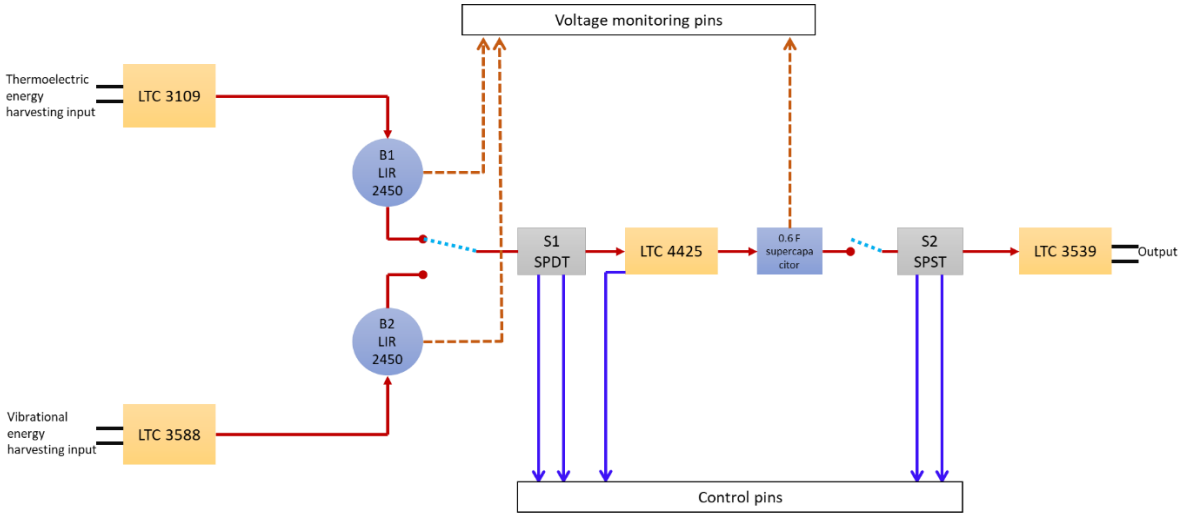

Figure 6. 13 Block diagram of proposed power management system with switched-energy storage

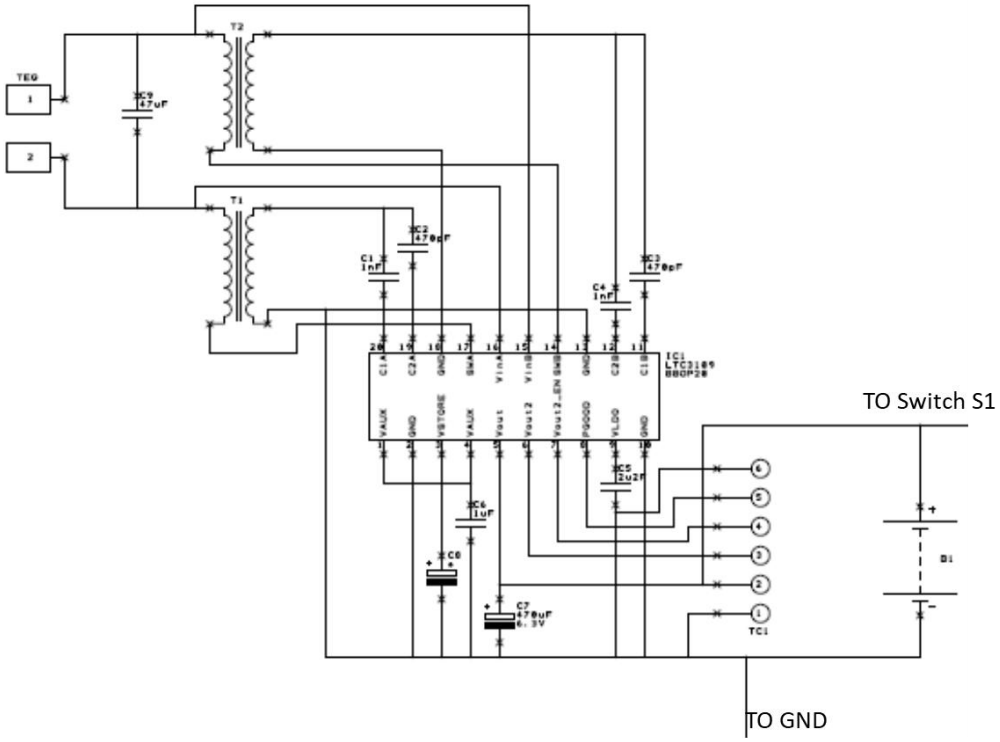

Figure 6. 14 Proposed power management system with switched-energy storage – focussing on LTC 3109 DC-DC converter section for thermoelectric harvested energy

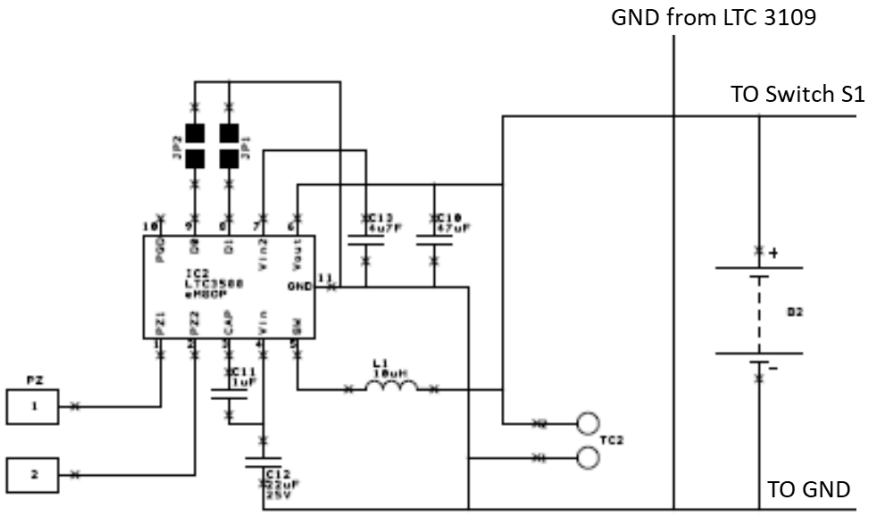

Figure 6. 15 Proposed power management system with switched-energy storage – Focussing on the LTC 3588 AC-DC converter section for vibrational harvested energy

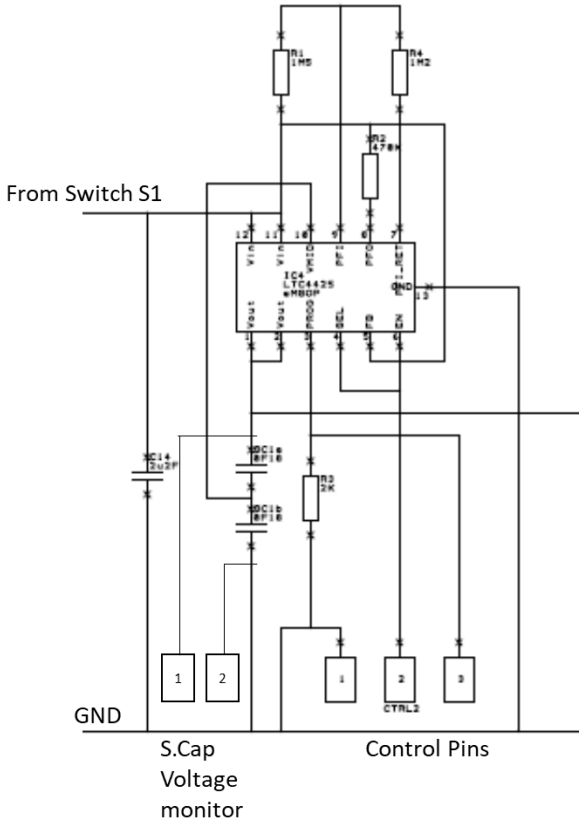

Figure 6. 16 Proposed power management system with switched-energy storage - Focussing on the LTC 4425 supercapacitor charger

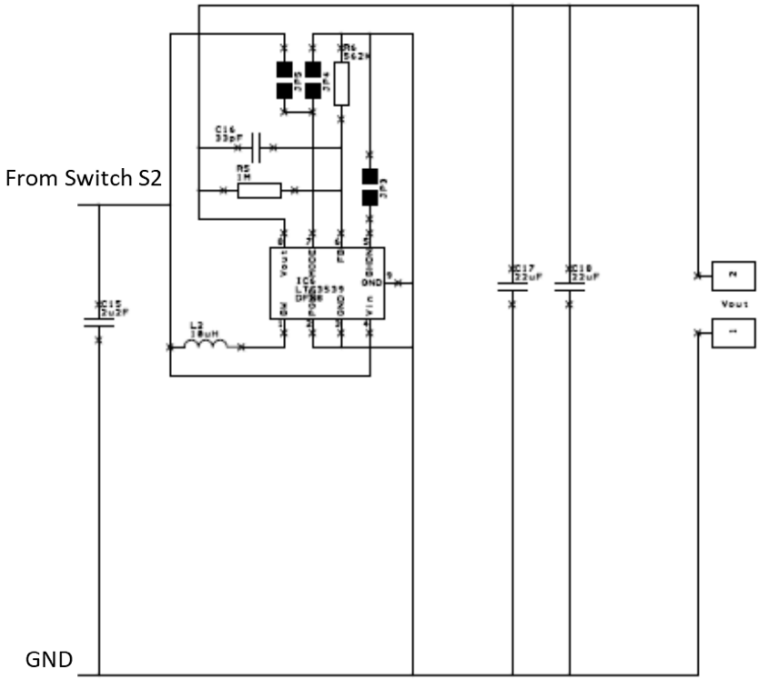

Figure 6. 17 Proposed power management system with switched-energy storage - Focussing on the LTC 3539 step-up converter

Based on the proposed circuit schematic, a PCB prototype was designed using Eagle PCB design software, and single-sided PCB was manufactured as shown in Figure 6.18 to 6.20.

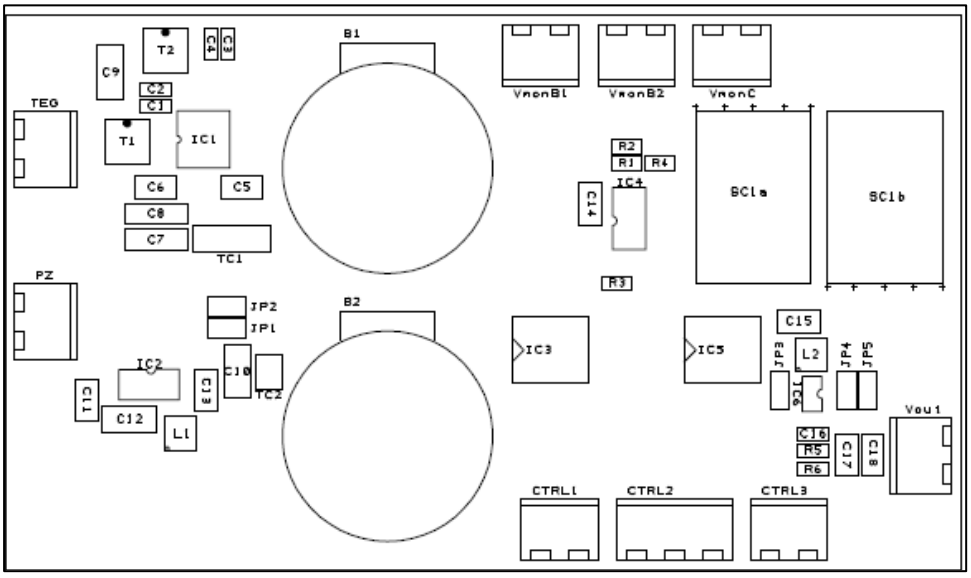

Figure 6. 18 Proposed power management system with switched-energy storage (top view of assembled PCB)

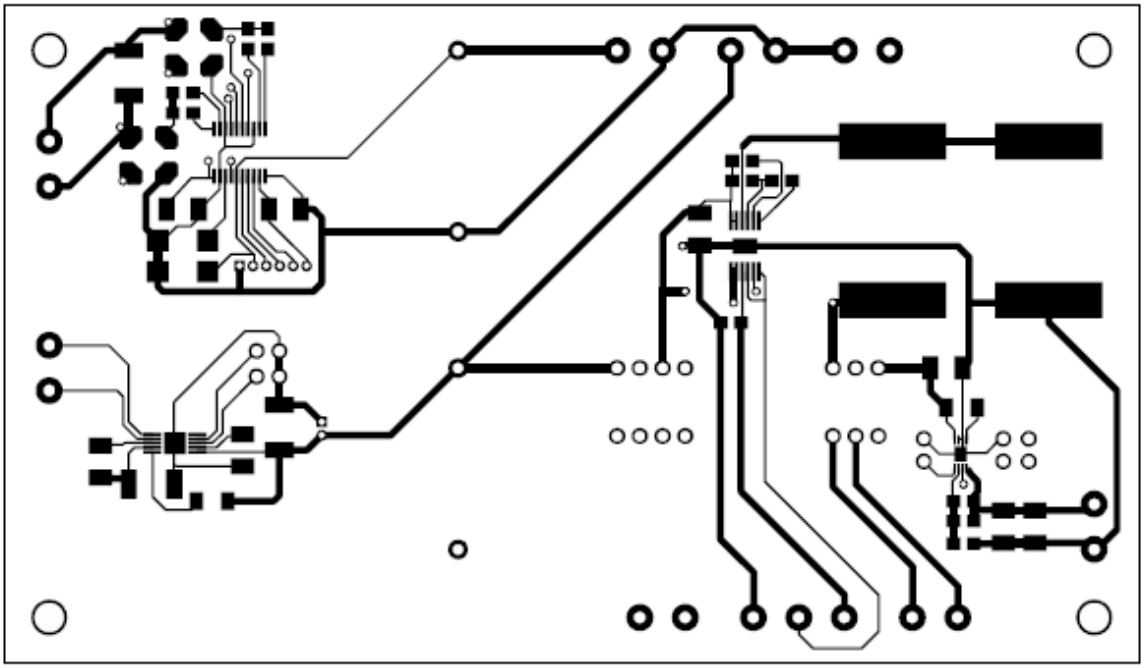

Figure 6. 19 Power management system with switched-energy storage (PCB-Layer 1)

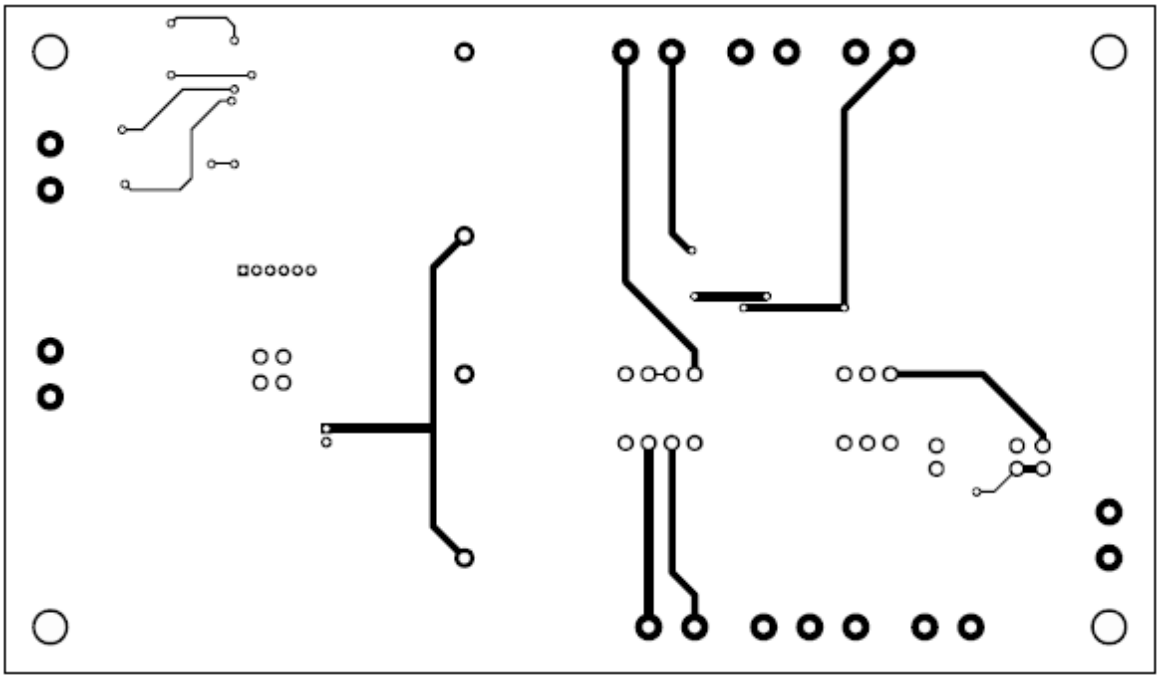

Figure 6. 20 Power management system with switched-energy storage (PCB-Layer 2)

6.7.1 Working Principle of circuit

The PWM system has two energy inputs, one for the LTC3109 and the other for the LTC3588 DC-DC converters, that convert the raw energy collected from thermoelectric and vibrational energy harvesters, respectively. The converted energy is stored in batteries B1 and B2 respectively. As explained in section 6.5 detailing the switched-energy storage system, the supercapacitor will power the WSN, and the battery will be used as a primary reservoir energy storage element. The switch S2 connects the two series 1.2 F, 5V Cap-xx supercapacitors to the LTC 3539 step-up converter.

As shown in Figure 6.21, the TEG output voltage profile, as identified in chapter two, is emulated using the Keysight N6705-B programmable voltage source in series with a 1.3 Ω series resistance and used as the input to LTC 3109. For the single polarity input, channel 1 of the N6705-B is connected to the V_{inA} input pin of LTC 3109. For dual polarity inputs, V_{inA} and V_{inB} Pins of LTC 3109 are connected to TEG.

The vibrational energy harvesting was included for future study.The Labview code as shown in Figure 6.22 was used for control. Switches S1 and S2, and the enable pin of LTC 4425 were connected to the digital outputs DO-0, DO-1 and DO-2 of Nidaq6211 data acquisition unit respectively. To monitor charging and discharging, the battery B1 and the supercapacitor charging voltages were connected to analogue ai0 and ai1 inputs of the Nidaq6211 data acquisition unit respectively. The voltage of battery and supercapacitor were logged at a rate of 1 sample per second. The pulsed-load, representing the *node-idle* and *transmission* function of strain WSN was generated from channel 2 of N6705B and connected to LTC 3539 as a load. Within Labview, the measured data was then converted to an array and written to an Excel compatible file format.

The switched- algorithm individually monitors the charging and discharging voltages of battery and supercapacitor. In order to initiate the post-landing monitoring, the algorithm checks the voltage level of the supercapacitor to be 4 V and set the switch S2 to '*high*' activate the connection between supercapacitor and LTC 3539. If the supercapacitor does not have a voltage level of 4 V, the algorithm checks for the battery with 4 V and initiate the charging with respective battery by setting up the switch S1 and enable pin of LTC 4425 as 'high'. If

both batteries have 4 V, the B1 was set to prefered choice. If both batteries do not have 4 V, an alert message will be transmitted to the data collector node.

After the post land monitoring for 60 minutes, the algorithm will set the switch S2 as ‘low’ and checks for the battery with 4 V and initiate charging with the respective battery. If the supercapacitor reaches 0.8 V during the post land monitoring, the algorithm initiates charging automatically with battery with 4 V. The servicing time of 30 minutes will be used to charge the supercapacitor from the batteries. After 30 minutes the algorithm will set the enable pin of LTC 4425 as ‘low’ to deactivate charging.

For pre-take, off monitoring the algorithm will set the switch S2 as ‘high’ and the supercapacitor will power the WSN through the LTC 3539. After 60 minutes of pre-takeoff monitoring, the switch S2 will be set as ‘low’ and using the 30 minutes of taxing time the supercapacitor will be charged with the battery with 4 V. The algorithm sets the enable pin of LTC 4425 and S 1 as ‘high’. To initiate charging between the battery B2 and supercapacitor, the algorithm will set LTC 4425 enable pin as ‘high’ and switch S1 as ‘low’. After 30 minutes the algorithm will set enable pin of LTC 4425 as ‘low’ to disconnect the connection between the battery and supercapacitor through LTC 4425.

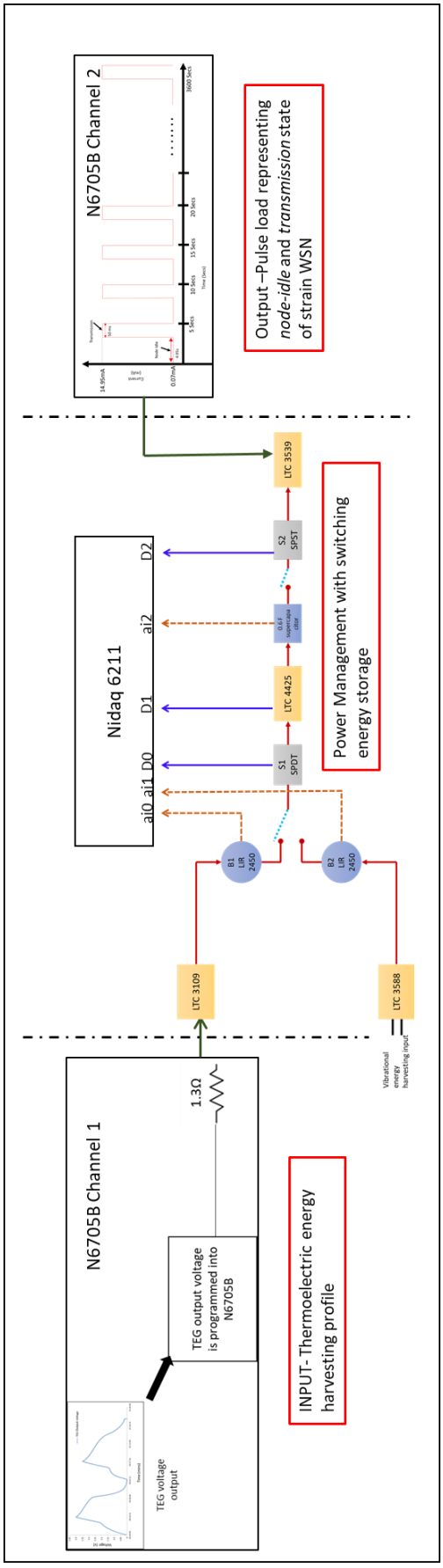

Figure 6.21 Experimental set up to demonstrate power management system with switched energy storage, powered by TEG generated output profile and load condition representing *node-idle* and *transmission* state of strain WSN.

6.7.2 Result Analysis

The aim of the experiment was to show by adopting switched-energy storage, the required efficient energy storage with longer cycle-life, less leakage current , operational temperature of -40°C to +40°C can be achieved. In switched-energy storage proposed in this thesis, all the harvested energy will be stored in the battery; the battery has low leakage current compared with a supercapacitor and no energy loss due to leakage current. The supercapacitor will power the WSN, the longer cycle-life of supercapacitor will be exploited. The supercapacitor is charged with the battery using LTC 4425; this approach preserves the cycle-life of the battery. As the battery is discharged under constant current method to charge the supercapacitor. The battery will only charge the supercapacitor, and it will not directly power the WSN , prevents the voltage drops for pulsed-load and preserves the cycle-life of the battery .The supercapacitor with its high power density property will be able to meet the peak current demand during the transmission state of WSN, and the supercapacitor also does not suffer from high voltage drops like the battery in low temperatures.

The experiment was carried out at room temperature, with a single LIR 2450 standard Li-Ion battery and two series 1.2 F Cap-xx supercapacitors used as storage units. On the basis of assumed scenario in chapter 2.5, the area around the cargo door to be monitored for 60 minutes after landing and 60 minutes before take off. The pulsed-load representing the *node-idle* and *transmission* state was used as the load condition. The total energy consumption of pulsed-load for 60 minutes will be 2.815 J . Both LIR 2450 and 0.60 F supercapacitor were initially charged up to 4 V by the constant voltage charging method. According to the assumed scenario, the area around the cargo door was monitored for a total of 120 mins, where the supercapacitor powers the assumed strain WSN through LTC 3539 step-up converter. The LTC 3539 gives a constant output voltage of 3.3 V, where the operating voltage of the assumed strain WSN is 3.3 V. The total amount of energy stored in the supercapacitor is 4.8 J , 0.6 F 4V.

In order to enable the supercapacitor to power the WSN through the LTC 3539, the switched-algorithm then turns-on the switch S2, to activate the connection between the supercapacitor and the LTC3539 step-up converter. AS shown in the Figure 6.22, the supercapacitor discharges to 0.825 V in approximately 60 minutes, and the total energy consumption of the pulsed-load plus the energy used by LTC 3539 was measured to be almost equal to 4.8 J. The switched-energy storage allows to selecte the supercapacitor based on the energy required

for the WSN, the smaller capacitance superapacitor will have the advantage of less leakage current and low ESR and thisis one of the main advantages of the switched-energy storage unit;In order to recharge the superapacitor from the battery once the post- land monitoring is completed the switched- algorithm turns off switch S2 to deactivate the connection, between supercapacitor and LTC 3539. In worst case scenario, if the supercapacitor reaches 0.8 V before the completion of the monitor, the switched- algorithm initiates charging between the supercapacitor and battery. This is another advantage of switched-energy storage, as the charging and discharging profile of battery and supercapacitor will be in individually monitored.

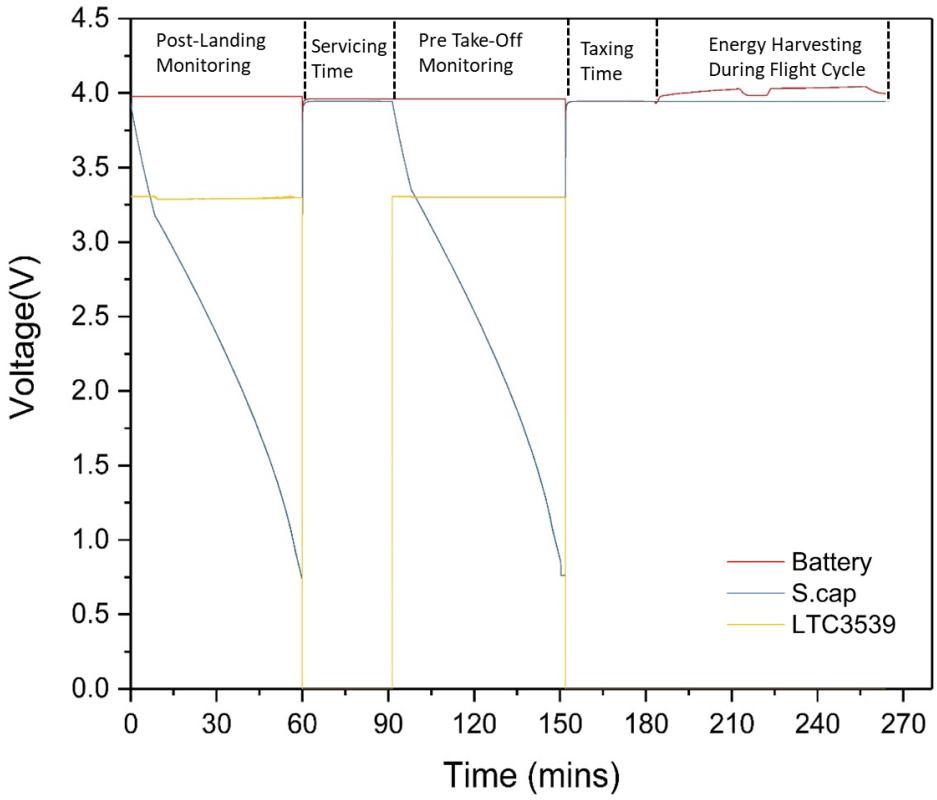

Figure 6.22 Charging and discharging of switched-energy storage with proposed power management for the assumed scenario at room temperature

The scenario includes a servicing time of 30 minutes where the aircraft remains stationary, and during this time, the supercapacitor is charged using the battery. The switched- algorithm initiates the charge by setting up an enable pin in LTC 4425 as '*high*'. The supercapacitor is charged back to 3.956 V from the battery over 30 minutes, and the total amount of energy

stored in the supercapacitor will be 4.71 J. The switched- algorithm will disable the charging after 30 minutes by setting up the enable pin of LTC 4425 as 'low'.

In the scenario assumed, the area around the cargo door would also be monitored for 60 minutes before the takeoff. The switched- algorithm will set as switch S2 as 'high' for 60 minutes, allowing the supercapacitor to power the WSN through the LTC3539 and this time the supercapacitor discharges to 0.812 V. The other advantage in the switched-energy storage system is, by using LTC 3539 all the energy stored in the supercapacitor will be used. After the 60 minutes of monitoring the algorithm will set switch S2 as 'low'.

During the taxing time of 30 minutes before the actual take off, the algorithm will set the enable pin of LTC 4425 '*high*' to initiate the charging process. The supercapacitor was recharged from the battery again up to 3.948 V and the total energy stored will be 4.67 J. By this approach the supercapacitor will be recharged and ready for the monitoring during the next flight cycle.The total amount of energy recharged for the supercapacitor from the battery for 60 minutes including the servicing and taxing time will be around 9.38 J. The switched-algorithm will set the enable pin of LTC 4225 as 'low' to deactivate the charging.

For the second flight cycle, the battery will be recharged for 80 minutes using the thermoelectric energy harvesting profile created in chapter 2.5. The LIR 2450 battery was charged up to 3.9965 V from 3.945 V , which is 0.052 V. So the total energy for 0.052V of 120 mAh battery will be 22.46 J.

The total required energy for 180 minutes of the assumed scenario including 120 of minutes monitoring and 60 minutes of supercapacitor charging will be around 16 J. The total harvested energy stored in the battery during the flight cycle is 22.46 J. This highlights the main advantage of the switched-energy storage unit, all the harvested energy will be stored in the battery and charges the supercapacitor by battery only when needed.

6.8 Chapter Conclusion

In previous chapters, the advantages of the hybrid system were identified. However, disadvantages such as supercapacitor leakage current, the lower cycle-life of the battery, and the fact that all the energy stored in the hybrid system cannot be accessed due to the battery operational cut-off voltages were also identified.

The switched-storage system proposed in this thesis significantly reduces these disadvantages Based on the experimental analysis of the previous chapter a power management circuit is proposed with switched-energy storage. The LIR 2450 standard Li-ion battery and two 1.2 F supercapacitor were used as storage units. LTC 3109, the dual polarity input DC-DC converter was used to convert the raw energy from the thermoelectric energy harvesting. LTC 4425 was used a supercapacitor charging from the battery LIR 2450. LTC 3539 was used an output step-up converter, for a constant voltage output.

The total energy required for the assumed scenario of area around cargo door monitoring will be around 16 J. The total energy stored in the LIR 2450 for 80 minutes of thermoelectric energy harvesting around the cargo door will be 22.46 J. All the harvested energy will be stored in the battery LIR 2450 and the supercapacitor will be charged only when needed. By using such system, the very high cycle-life of the supercapacitor is exploited, and it is utilised as the prime, dynamic energy source powering the WSN. The battery is used as a primary reservoir energy source and will charge the supercapacitor only when needed. Over both discharging periods, the battery voltage does not reach its cut-off voltage, which is another important factor in the runtime extension of the battery. As there is no active connection always between the battery and supercapacitor, the leakage current will no longer be a common factor. All the harvested energy will be stored in the battery, the battery has low leakage current compared with supercapacitors, so the energy loss in the form of leakage current will be considerably reduced.

Unfortunately, the MEC 202 thin-film solid-state battery was discontinued, and so, LIR 2450 standard Li-ion battery was used as a replacement. The total weight of the energy storage system including LIR 2450 and two 1.2 Cap-xx supercapacitors will be around 6.1 g, and by replacing the LIR 2450 battery with thin-film solid-state battery, the total weight of the energy

storage will be around 1.5 g. The same amount of 22 J of harvested energy can be stored in MEC 202 thin-film solid-state battery.

LIR 2450 with a higher power rating of 120mAh weighs 5.5 g, whereas the thin-film with a rating of 2.2mAh weighs only 0.975g. The total possible energy stored from the current state of art thermoelectric energy harvesting system (von Allmen, Bailleul et al. 2017) is 79 J. In the switched-energy storage system with two thin-film batteries as a primary storage unit and supercapacitor as secondary storage unit with weight of approximately 4 g, the 79 J of energy can be stored.

7. Overarching Discussion, Conclusions and Further Work

7.1 Overarching Discussion and Conclusions

In this thesis, efficient energy storage has been identified as an essential part of the ASHM system powered by energy harvesting, as harvested energy is not available for the entire flight cycle.

An application scenario of monitoring aircraft structure around cargo door using a strain WSN powered by locally harvested thermoelectric energy harvesting has been assumed for use throughout the thesis. The temperature around the aircraft section near the cargo door ranges from -20^{o}C to +20^{o}C, but the temperature in other sections of aircraft can range from -40^{o}C to +40^{o}C. The storage units to be considered for this application assume the most extreme case, so must work in the temperature range of -40^{o}C to +40^{o}C, have a longer cycle-life and less leakage current. The other important factor is weight, and one of the main criteria for AASHM is to perform SHM analysis in aircraft without adding significantly to the overall weight of the aircraft. Thin-film Li-ion batteries (MEC202 4 V 2.2mAh), standard Li-ion coin cell batteries (4.2 V 120mAh), and various sizes of supercapacitor are the storage options investigated in this thesis.

Unfortunately, the thin-film Li-ion battery was discontinued during the research phase, and the LIR 2450 standard Li-ion battery was used as a replacement to demonstrate the working principles of switched-energy storage systems. The cycle-life of the standard Li-ion battery used is 1000 cycles, as per the data sheet. However, this cycle-life was estimated based on a constant current discharge method. The WSN is a load that demands peak current in short-burst duration such as *wake-up* and *transmission* modes, and a pulsed-load discharge scenario will considerably reduce the batteries cycle-life. The operating temperature of the standard Li-ion battery is -20^{o}C to +45^{o}C. Although it works in the temperature between -40^{o}C to +40^{o}C continuous exposure to this temperature range will also reduce the cycle-life. Dendrites may also occur when the Li-ion battery is discharged at the faster cycle rate. The thin-film Li-ion battery uses a solid electrolyte – a material referred to as LiPON and this

material has the benefit of allowing the ready flow of lithium ions for high currents that prevent the occurrence of dendrites.

A TEG power output profile was generated using a previous study of thermoelectric energy harvesting near the aircraft cargo door location. This generated profile was used to charge the storage elements in the temperature range between -40^{o}C to +40^{o}C for 80 minutes in a climatic chamber. An LTC 3109 was used as a DC-DC converter for charging of the batteries and supercapacitors. In this device, there is no inbuilt programmable maximum power point tracking (MPPT), but it was chosen for its low power start-up and dual polarity input suitable for thermoelectric harvesting, however, in this thesis only a single polarity TEG output profile was used. The LTC3109 performed well over the -40^{o}C to +40^{o}C temperature range. The open circuit output voltages for *Vout* and *Vstore* pins were measured while being excited by the generated TEG output profile, where it was seen that supercapacitor charging was not affected by the temperature range of -40^{o}C to +40^{o}C. LIR 2450 was also tested over this temperature range, even though the minimum operating temperature range was specified as -20^{o}C, and the LIR 2450 charging rate was seen to considerably reduced as the temperature started decreasing below -20^{o}C. Charging was carried out based on a constant voltage method, and the charging time was established as the same for the -20^{o}C and +20^{o}C scenario. However, as the temperature increases, the ions in the solid state thin-film Li-ion battery could move freely and thus the charging time was decreased. In lower temperature, the ions were not able to move freely, and the charging time considerably increased. In -40^{o}C charging was not initiated at all.

The thin-film Li-ion battery was not charged using this temperature profile as it was discontinued at the time.

In the scenario considered, the area around the cargo door was monitored using a strain WSN with an operating voltage of 3.3 V. A pulsed-load was generated for establishing a *node-idle* state with duration (t_o) of 4.95 s and a current demand of 0.07 mA, followed by a *transmission* state with duration (t_1) of 50 ms and a current demand of 14.95 mA, with the total waveform time (t) of 5 s. This load was programmed in an N6705B DC power analyser and acted as a pulsed-load to discharge the storage elements. The discharge monitoring experiment was carried in the same temperature range of -40^{o}C to +40^{o}C. The charging experiment was

carried on every time immediately after the discharge experiment, to ensure the storage elements were charged and discharged at the same temperature level.

The supercapacitor discharge behaviour was not affected by the temperature. With the thin-film battery, as the temperature increased the performance was enhanced with the mobility of ions, but at lower temperatures, the performance was significantly degraded, and at -40^{o}C the thin-film battery did not function at all. According to the datasheet, the thin-film battery should work well within the temperature range -40^{o}C to +40^{o}C, as the datasheet testing was measured using a constant current discharge method. However, a WSN typically demands a high current for short periods, and the thin-film battery was not able to provide that, which in turn causes problematic voltage drops during times of peak current demand. Moreover, the observed voltage drops increased as the temperature decreased, proving the improper functioning of the thin-film at lower temperatures. In the same way as the thin-film battery, the standard Li-ion battery performed better at higher temperatures, and similarly, as the temperature decreases the voltage drops increases. Moreover, these voltage drops can considerably reduce the cycle-life of the battery as well as reducing the runtime of WSN. The supercapacitor charge and discharge behaviour were not affected by the temperature, and with its higher power density, the supercapacitor was able to meet the high current demands of the WSN. However, to store 41.32 J of energy required, a 5F supercapacitor weighing 12.6 g would be required to store the same amount of energy as a 0.975 g thin-film Li-ion battery, and increasing capacitance in this way will increases ESR and leakage current.

In energy harvesting application where harvesting is not possible during the entire flight cycle, losing stored energy in the form of leakage current will be considered a significant disadvantage. From the experimental analysis up to this point, it is concluded that thin-film Li-ion batteries, standard Li-ion batteries and supercapacitors in standalone mode cannot provide an ideal solution.

An energy storage system should be able to provide energy for both long-term operations as well as being able to meet the peak power demand during the transmission state of the WSN. Adding a supercapacitor parallel to a battery to form a hybrid energy storage element can provide a possible solution. A simple parallel combination of a thin-film, Li-ion battery and 1.5 F supercapacitor can store up to 44.48 J of energy with a total weight of 5.975 g. This hybrid

combination can provide significant runtime extension for a WSN, in comparison here to a single 5 F, supercapacitor weighing 12.6 g and offering just 3 J of more energy.

An *Airbus* designed temperature, and humidity WSN was used for this comparison of a hybrid energy storage element with a supercapacitor. In this comparison, the hybrid energy storage element provided 10 hrs extended runtime for the WSN compared to a supercapacitor, under representative pulsed load conditions. The observed voltage drops in the thin-film Li-ion battery were reduced by adding the supercapacitor in parallel to the battery, and this increases the runtime of the WSN. However, there are several disadvantages identified in this hybrid system with the reduced cycle-life of the thin-film Li-ion battery and the high leakage current of supercapacitor will become factors.

In a simple hybrid approach, all the energy stored in the supercapacitor was not used, due to the low cut off voltage of the thin-film battery. Since the MEC202 thin-film battery was discontinued, it was not possible, unfortunately, to test the hybrid energy storage with a step-up converter for the runtime extension of WSN.

The LTC 3539 is the output step-up converter used in this thesis and can be programmed to give a constant voltage output of 1.2 V, 3.3 V and 5 V. To mitigate the disadvantages identified in simple hybrid energy storage, an efficient switched-energy storage approach is proposed in this thesis. By adopting a switched-energy storage system with a thin-film Li-ion battery as the primary energy storage element, and a supercapacitor as the secondary energy storage element, 40 J of energy can be stored in the thin-film Li-ion battery and 9 J of energy stored in the 1.2 F supercapacitor. This storage system was tested under the usual scenario of monitoring the aircraft structure around the cargo door for 77 minutes post-landing and 77 minutes pre-takeoff periods. The total energy consumption of the strain WSN in *node-idle* and *transmission* mode is around 3.6 J. The supercapacitor will power the strain WSN after aircraft landing for 77 minutes, and during a servicing time of 30 minutes, the thin-film Li-ion battery will charge the supercapacitor. After this time, the supercapacitor will be ready to power the WSN for 77 minutes for pre-takeoff monitoring. The advantage of the switched-energy storage system supercapacitor's very high cycle-life is exploited, and cycle-life of the thin-film Li-ion battery is preserved.

A power management test-board incorporating a switched-energy storage system was also proposed in this thesis. The LTC 3109, dual polarity DC-DC converter is used to convert the raw harvested energy with storage provided by the LIR 2450 standard Li-ion battery. During the ASHM process, the supercapacitor will power the WSN through an LTC 3539 step-up converter. The output voltage of the LTC 3539 can be set to either 3.3 V or 5V, depending upon the operating voltage of the WSN. During the 30 minutes of servicing time, the supercapacitor will be charged from the battery, and the supercapacitor can power the pre-takeoff ASHM process. The supercapacitor will be charged again during the 30 minutes taxing time before take-off, so the supercapacitor will be ready to power the WSN after the second flight cycle. Moreover, the switched-controller is also programmed to automatically enable charging once the supercapacitor reaches 0.8 V. The total required energy for 180 minutes of the assumed scenario including 120 minutes of monitoring and 60 minutes of supercapacitor charging will be around 16 J. The total harvested energy stored in the standard Li-ion battery during the flight cycle is 22.46 J. This highlights the main advantage of the switched-energy storage unit; all the harvested energy will be stored in the battery, and the supercapacitor is charged only when needed. Energy loss in form the leakage current will be also be reduced, as the all the harvested energy will be stored in the battery. The total weight of the energy storage system, including the LIR 2450 battery and two 1.2 Cap-xx supercapacitors is approximately 6.1 g, and by replacing the LIR 2450 battery with thin-film solid-state battery, the total weight of the energy storage will be around 1.5 g. The same amount of 22 J of harvested energy can be stored in MEC 202 thin-film solid-state battery.

The thesis does not present the hybrid energy storage unit as an ideal solution, but it does have significant advantages; in the switched-energy storage unit, the battery will charge the supercapacitor with a constant current charging method, and the battery will not power the WSN directly. Because of this, the battery will not suffer from problematic voltage drops associated with peak current demand, and thus the cycle-life of the battery will be preserved. Therefore, the thin-film battery, if available, with its 10000 cycle-life is a better choice than the LIR 2450 with 1000 cycle-life, even though the energy density is higher for LIR 2450 with its power rating of 120 mAh.

By adopting the proposed switched-energy storage system, a 500000-cycle-life of supercapacitor was exploited, with 0.006 mA maximum leakage current of the thin-film solid-

state battery offering virtual no energy loss in terms of leakage current. The supercapacitor was charged using constant charging method from the battery, so the 10000 cycle-life of thin-film Li-ion battery was preserved. The supercapacitor can be selected based on energy consumption, so a low capacitance value with low ESR can be selected, and an operational temperature range of -40^{o}C to +40^{o}C can be achieved. In addition to this, the existing energy storage in Airbus ASHM system uses two PC 10 Maxwell supercapacitor in series. The total amount of energy can be stored is 41.32 J, and the weight is 12.6 g. By adopting the switched-energy storage to store 44.48 J of energy, the total weight required for switched-energy storage system can be reduced to 7.1 g, that is 56 % of weight per sensor node will be saved compared to the existing energy storage system of Airbus - an important factor in the design of an aircraft SHM system due to its effects on fuel consumption and emissions.

The main conclusions are identified below:

- Energy harvesting is seen as a viable option for powering AASHM sensors. However, further, development is required to match the power consumption levels of an AASHM system with available energy sources.
- Commercially available dc-dc converters cannot provide efficient conversion of this harvested energy as these converters do not meet the general requirements of AASHM, such as dual polarity input conversion low start-up voltage and MPPT. Custom designed dc-dc converters are needed.
- The need for MPPT is left as a design consideration for the design engineer as the power consumed in performing MPPT has to be considered before applying to applications with limited harvestable energy. A detailed study is required to look into the viability of the implementation of MPPT algorithms in AASHM power management systems.
- Efficient energy storage is a crucial part of any AASHM system, as energy harvesting is not possible throughout the entire flight cycle.
- Current technology batteries and supercapacitor are not suitable for use as stand-alone storage units for WSN. A typical WSN requires an energy source with high energy and power density.

- Extension of the runtime of a WSN is possible with a hybrid energy storage unit, but hybrid energy storage cannot be used in the form of the simple parallel combination as they do not have same cycle-life or leakage current properties.
- Energy storage with switched-architecture will enable the advantages of hybrid energy storage to be exploited whilst overcoming some of its disadvantages.
- Compared with an existing storage unit of Airbus ASHM approximately 53 % of weight per sensor can be saved by adopting to the switched-energy storage unit.

7.2 Recommendation for Future work

This thesis has discussed an efficient way of storing energy harvested using a TEG in an aircraft structure, and using that stored energy to power aircraft SHM wireless sensors. Further work is required in order for these systems to be incorporated into an aircraft, and these include:

- The foremost challenge is to develop and demonstrate wireless SHM technologies with embedded sensors that can be used to monitor structural integrity in service conditions with high reliability & durability.
- The power consumption of the wireless systems for SHM application needs to be further reduced with advancement in the microelectronic study to enable it to be matched to the levels of power which can be harvested in an aircraft environment.
- The robustness and reliability of installed sensors need to be ensured. There might be a need to monitor the sensors to detect the failure. In addition to this, sensor networks need to be fail-safe. In the case of a sensor failure, damage identification algorithms must be able to adapt to the new network. In short, the sensor network needs to be redundant.
- The efficiency of thermoelectric energy harvesters including materials used and their implementation to exploit both static and dynamic thermal gradients needs to be improved.

- The commercially available dc-dc converter has individual inbuilt advantages, but for aircraft specific thermoelectric energy harvesting, a dc-dc converter should have a quick start-up time, low start-up voltage and simple MPPT algorithm. Achieving such efficient dc-dc conversion is crucial for power management.
- The design of proposed PWM circuit and experiment on efficiency on energy conversion should be conducted.
- Improvement of power density in batteries or energy density in supercapacitors can lead to a stand-alone storage unit option for AASHM.
- Thin-film solid-state batteries, from Cymbet, ST Microelectronics, Excelleron and Brightvolt should be tested for this application.
- Advanced microcontrollers or field programmable gate array FPGA with low power consumption and efficient control over the energy harvesting and wireless sensor system are needed.
- Sensors and their local processors should be more integrated with microelectronics allowing a more decentralised architecture where local processors perform and record the first level of SHM processing with the transmission of the output to an upper-level processor.
- Development of efficient aircraft SHM algorithms, for preprocessing the raw data from the sensor is needed. This could lead to advanced alert systems and lower power consumption for wireless data transfer.
- Adaptation of future innovative approaches is being developed in microelectronics, MEMS, etc. which will improve effectiveness and costs.

8. References

ACHENBACH, J. D. 2009. Structural health monitoring–What is the prescription? *Mechanics Research Communications*, 36, 137-142.

ALDRIN, J. C., MEDINA, E. A., ALLWINE, D. A., QADEER AHMED, M., FISHER, J., KNOPP, J. S. & LINDGREN, E. A. 2006. Probabilistic Risk Assessment: Impact of Human Factors on Nondestructive Evaluation and Sensor Degradation on Structural Health Monitoring (Preprint). DTIC Document.

BEARD, S. J., KUMAR, A., QING, X., CHAN, H., ZHANG, C. & OOI, T. K. Practical issues in the real-world implementation of structural health monitoring systems. *Smart Structures and Materials*, 2005. *International Society for Optics and Photonics*, 196-203.

BECKER, T., KLUGE, M., SCHALK, J., TIPLADY, K., PAGET, C., HILLERINGMANN, U. & OTTERPOHL, T. 2009. Autonomous sensor nodes for aircraft structural health monitoring. *Sensors Journal*, IEEE, 9, 1589-1595.

BELLEVILLE, M. AND C. CONDEMINE (2012). Energy-autonomous micro and nano systems. London Hoboken, N.J., ISTE ;Wiley.

BLACKSHIRE, J. L. & COONEY, A. Evaluation and improvement in sensor performance and durability for structural health monitoring systems. Nondestructive Evaluation for Health Monitoring and Diagnostics, 2006. *International Society for Optics and Photonics*, 61790K-61790K-10.

BOCCA, M., COSAR, E., SALMINEN, J. & ERIKSSON, L. A reconfigurable wireless sensor network for structural health monitoring. *Proceedings of the 4th international conference on structural health monitoring of intelligent infrastructure*, 2009. 22-24.

Boller, C., et al. (1999). Structural damage monitoring based on an actuator-sensor system. Smart Structures and Materials 1999: Smart Structures and Integrated Systems, International Society for Optics and Photonics

BOLLER, C. 2000. Next generation structural health monitoring and its integration into aircraft design. *International Journal of Systems Science*, 31, 1333-1349.

BURCHELL, T. D. 1999. *Carbon materials for advanced technologies*, Amsterdam; New York, Pergamon.

C. VADSTRUP, E. SCHALTZ, AND M. CHEN, "Individual Module Maximum Power Point Tracking for Thermoelectric Generator Systems," *J. Electron. Mater.,* vol. 42, no. 7, pp. 2203–2208, Apr. 2013.

CHANG, F.-K. 1998. Structural health monitoring: current status and perspectives, CRC Press.

CHANG, F.-K. Design of integrated SHM system for commercial aircraft applications. *5th International Workshop on Structural Health Monitoring*, 2005. Stanford University Press Stanford.

ROWE, D. M. (2012). Thermoelectrics and its energy harvesting. Boca Raton, FL, CRC Press.

DE BRITO, M. A. G., et al. (2013). "Evaluation of the main MPPT techniques for photovoltaic applications." IEEE transactions on industrial electronics 60(3): 1156-1167.

DEARBORN, S., 2005. Charging Li-ion Batteries for Maximum Run Times. *Power Electronics Technology*, Issue 117, pp. 41-49

DERRISO, M. M. & CHANG, F.-K. 2006. Future Roles of Structural Sensing for Aerospace Applications. DTIC Document.

DILHAC, J.-M., MONTHÉARD, R., BAFLEUR, M., BOITIER, V., DURAND-ESTÈBE, P. & TOUNSI, P. 2014. Implementation of Thermoelectric Generators in Airliners for Powering Battery-Free Wireless Sensor Networks. *Journal of Electronic Materials*, 43, 2444-2451.

DOUGAL, R. A., LIU, S. & WHITE, R. E. 2002. Power and life extension of battery-ultracapacitor hybrids. Components and packaging technologies, *IEEE Transactions* on, 25, 120-131.

DU PASQUIER, A., PLITZ, I., GURAL, J., BADWAY, F. & AMATUCCI, G. 2004. Power-on battery: bridging the gap between Li-ion and supercapacitor chemistries. *Journal of Power Sources,* 136, 160-170.

ELEFSINIOTIS, A., BECKER, T. & SCHMID, U. 2014. Thermoelectric energy harvesting using phase-change materials (PCMs) in high-temperature environments in aircraft. *Journal of Electronic Materials*, 43, 1809-1814.

ELEFSINIOTIS, A., KIZIROGLOU, M., WRIGHT, S., TOH, T., MITCHESON, P., BECKER, T., YEATMAN, E. & SCHMID, U. Performance evaluation of a thermoelectric energy harvesting device using various phase change materials. *Journal of Physics: Conference Series*, 2013. IOP Publishing, 012020.

FARRAR, C. R. & WORDEN, K. 2007. An introduction to structural health monitoring. Philosophical Transactions of the Royal Society of London A: Mathematical, Physical and Engineering Sciences, 365, 303-315.

FARRAR, C., CZARNECKI, J., SOHN, H. & HEMEZ, F. 2002. A review of structural health monitoring literature 1996-2001.

FEATHERSTON, C. A., HOLFORD, K. M. & WARING, G. 2009. Thermoelectric Energy Harvesting For Wireless Sensor Systems in Aircraft. In: CHU, F., OUYANG, H., SILBERSCHMIDT, V., GARILADI, L., SURACE, C., OSTACHOWICZ, W. M. & JIANG, D. (eds.) Damage Assessment of Structures Viii.

FEATHERSTON, C. A., HOLFORD, K. M., PULLIN, R., LEES, J., EATON, M. & PEARSON, M. 2013. An Autonomous Structural Health Monitoring Solution. Smart Sensors, Actuators, and Mems Vi, 8763.

FINLAYSON, R. D., FRIESEL, M., CARLOS, M., COLE, P. & LENAIN, J. 2001. Health monitoring of aerospace structures with acoustic emission and acoustic-ultrasonics. Insight-Wigston then Northampton-, 43, 155-158.

FLYNN, E. B. & TODD, M. D. 2010. A Bayesian approach to optimal sensor placement for structural health monitoring with application to active sensing. *Mechanical Systems and Signal Processing*, 24, 891-903.

FU, T., LIU, Y., LI, Q. & LENG, J. 2009. Fiber optic acoustic emission sensor and its applications in the structural health monitoring of CFRP materials. *Optics and Lasers in Engineering*, 47, 1056-1062.

GALEA, S. C. & BAKER, A. A. 2001. Smart structures approach for health monitoring of aircraft structures. In: SOOD, D. K., LAWES, R. A. & VARADAN, V. V. (eds.) *Smart Structures and Devices.*

GAO, L., DOUGAL, R. A. & LIU, S. 2005. Power enhancement of an actively controlled battery/ultracapacitor hybrid. *Power Electronics, IEEE Transactions* on, 20, 236-243.

GIURGIUTIU, V. 2013. Embedded NDT with piezoelectric wafer active sensors. *Nondestructive Testing of Materials and Structures. Springer.*

GUALOUS, H., et al. (2003). "Experimental study of supercapacitor serial resistance and capacitance variations with temperature." *Journal of Power Sources* ***123****(1): 86-93.*

HOLLAND, C. E., WEIDNER, J., DOUGAL, R. & WHITE, R. 2002. Experimental Characterisation of hybrid power systems under pulsed current loads. *Journal of power sources*, 109, 32-37.

JANÁK, L. 2014. MEMS termoelektrický generátor v letecké aplikaci. Vysoké učení technické v Brně. Fakulta strojního inženýrství.

KAZIMIERCZUK, *Pulse-Width Modulated DC-DC Power Converters*. Chichester, West Sussex: John Wiley & Sons, Ltd., 2008.

KIM, H., TADESSE, Y. & PRIYA, S. 2009. Piezoelectric energy harvesting. *Energy Harvesting Technologies. Springer.*

KIREMIDJIAN, A. S., KIREMIDJIAN, G. & SARABANDI, P. 2011. A wireless structural monitoring system with embedded damage algorithms and decision support system. *Structure and Infrastructure Engineering*, 7, 881-894.

KÖTZ, R., HAHN, M. & GALLAY, R. 2006. Temperature behaviour and impedance fundamentals of supercapacitors. *Journal of Power Sources*, 154, 550-555.

KULLAA, J. 2011. Distinguishing between sensor fault, structural damage, and environmental or operational effects in structural health monitoring. *Mechanical Systems and Signal Processing*, 25, 2976-2989.

KUPERMAN, A. & AHARON, I. 2011. Battery–ultracapacitor hybrids for pulsed current loads: A review. *Renewable and Sustainable Energy Reviews*, 15, 981-992.

LAVEUVE, D. M., LEHMANN, M., ERDMANN, K. & BÜTTER, A. SHM–reliability demands on the multidisciplinary challenge of structural health monitoring. NDT in Progress, *5th International Workshop of NDT Experts*, Prague, 2009. 12-14.

LOUTAS, T. H., PANOPOULOU, A., ROULIAS, D. & KOSTOPOULOS, V. 2012. Intelligent health monitoring of aerospace composite structures based on dynamic strain measurements. *Expert Systems with Applications*, 39, 8412-8422.

MAJUMDER, M., GANGOPADHYAY, T. K., CHAKRABORTY, A. K., DASGUPTA, K. & BHATTACHARYA, D. K. 2008. Fibre Bragg gratings in structural health monitoring—Present status and applications. *Sensors and Actuators* A: Physical, 147, 150-164.

MANDACHE, C., GENEST, M., KHAN, M. & MRAD, N. Considerations on structural health monitoring reliability.

MATHUNA, C. O., O'DONNELL, T., MARTINEZ-CATALA, R. V., ROHAN, J. & O'FLYNN, B. 2008. Energy scavenging for long-term deployable wireless sensor networks. Talanta, 75, 613-623.

MCCARTY, R. 2013. Thermoelectric power generator design for maximum power: It's all about ZT. *Journal of electronic materials*, 42, 1504-1508.

MICKENS, T., SCHULZ, M., SUNDARESAN, M., GHOSHAL, A., NASER, A. & REICHMEIDER, R. 2003. Structural health monitoring of an aircraft joint. *Mechanical Systems and Signal Processing*, 17, 285-303.

MONTALVAO, D., MAIA, N. M. M. & RIBEIRO, A. M. R. 2006. A review of vibration-based structural health monitoring with special emphasis on composite materials. Shock and Vibration Digest, 38, 295-326.

Nikolov, H. (2017) Vibration energy harvesting for structural health monitoring applications, Undergraduate dissertation, Cardiff University, Cardiff.

NOOR, A. K., VENNERI, S. L., PAUL, D. B. & HOPKINS, M. A. 2000. Structures technology for future aerospace systems. *Computers & Structures,* 74, 507-519.

ONGARO, F., SAGGINI, S. & MATTAVELLI, P. 2012. Li-ion battery-supercapacitor hybrid storage system for a long lifetime, photovoltaic-based wireless sensor network. *Power Electronics, IEEE Transactions* on, 27, 3944-3952.

PARK, J. AND S. KIM (2012). "Maximum power point tracking controller for thermoelectric generators with peak gain control of boost DC-DC converters." Journal of Electronic Materials **41**(6): 1242-1246

PEARSON, M. R., EATON, M. J., PULLIN, R., FEATHERSTON, C. A., HOLFORD, K. M. & IOP 2012. Energy Harvesting for Aerospace Structural Health Monitoring Systems. MoPractice in Stress and Vibration Analysis 2012 (Mpsva 2012), 382.

PEARSON, M. (2013). Development of lightweight structural health monitoring systems for aerospace applications,PhD thesis, Cardiff University,Cardiff.

PENELLA, M. T. & GASULLA, M. 2010. Runtime extension of low-power wireless sensor nodes using hybrid-storage units. *Instrumentation and measurement, IEEE transactions* on, 59, 857-865.

PENELLA-LÓPEZ, M. T AND M. GASULLA-FORNER, *Powering Autonomous Sensors: An Integral Approach with Focus on Solar and RF Energy Harvesting*. Dordrecht Heidelberg London New York: Springer, 2011, p. 147.

PRIYA AND D. J. INMAN, EDS., *Energy Harvesting Technologies*. New York: Springer Science+Business Media, LLC, 2009.

PREVOROVSKY, Z., KROFTA, J., FAROVA, Z. & CHLADA, M. 6th NDT in Progress 2011.

RAMOHALLI, G. The Honeywell onboard diagnostic and maintenance system for the Boeing 777. *Digital Avionics Systems Conference*, 1992. *Proceedings, IEEE/AIAA 11th*, 1992. IEEE, 485-490.

RASHID, M. H. (2010). Power electronics handbook: devices, circuits and applications, Academic Press.

SABATER, J., et al. (2007). Low power low latency MAC protocol for aeronautical applications. Proc. SPIE.

SAMSON, D., et al. (2010). Energy Harvesting for Autonomous Wireless Sensor Nodes in Aircraft. Eurosensors Xxiv Conference. B. Jakoby and M. J. Vellekoop. **5:** 1160-1163

SAMSON, D., et al. (2010). "Aircraft-Specific Thermoelectric Generator Module." Journal of Electronic Materials **39**(9): 2092-2095

SAMSON, D., ET AL. (2011). "Wireless sensor node powered by aircraft specific thermoelectric energy harvesting." Sensors and Actuators A: Physical **172**(1): 240-244.

SCHALKWIJK, W. A. V. & SCROSATI, B. 2002. Advances in lithium-ion batteries, New York, NY, Kluwer Academic/Plenum Publishers.

SCHINDALL, J. 2007. The charge of the ultracapacitors. Spectrum, *IEEE*, 44, 42-46.

SEAH, W. K., EU, Z. A. & TAN, H.-P. Wireless sensor networks powered by ambient energy harvesting (WSN-HEAP)-Survey and challenges. Wireless Communication, Vehicular Technology, Information Theory and Aerospace & Electronic Systems Technology, 2009. Wireless VITAE 2009. *1st International Conference on, 2009. Ieee, 1-5.*

SIMJEE, F. I. & CHOU, P. H. 2008. Efficient charging of supercapacitors for an extended lifetime of wireless sensor nodes. *Power Electronics, IEEE Transactions* on, 23, 1526-1536.

SMITH, T., MARS, J. & TURNER, G. Using supercapacitors to improve battery performance. *Power electronics specialists conference, 2002. Pesc 02. 2002 IEEE 33rd annual, 2002. Ieee, 124-128.*

STASZEWSKI, W., BOLLER, C. & TOMLINSON, G. R. 2004. *Health monitoring of aerospace structures: smart sensor technologies and signal processing*, John Wiley & Sons.

STASZEWSKI, W. J., et al. (2009). "Health monitoring of aerospace composite structures – Active and passive approach." Composites Science and Technology **69**(11): 1678-1685.

TARASCON, J.-M. AND M. ARMAND (2001). "Issues and challenges facing rechargeable lithium batteries." Nature **414**(6861): 359-367.

THAKUR, H. V., NALAWADE, S. M., SAXENA, Y. & GRATTAN, K. 2011. All-fiber embedded PM-PCF vibration sensor for Structural Health Monitoring of the composite. *Sensors and Actuators A: Physical*, 167, 204-212.

THANGARAJ, K., ELEFSINIOTS, A., ASLAM, S., BECKER, T., SCHMID, U., LEES, J., FEATHERSTON, C. A. & PULLIN, R. 2013. Hybrid energy storage system for wireless sensor node powered by aircraft specific thermoelectric energy harvesting. *Smart Sensors, Actuators, and Mems* Vi, 8763.

THANGARAJ, K., et al. (2014). "Energy storage options for wireless sensors powered by aircraft specific thermoelectric energy harvester." Microsystem Technologies-Micro-and Nanosystems-Information Storage and Processing Systems **20**(4-5): 701-707

UNO, M. AND K. TANAKA (2012). "Accelerated charge–discharge cycling test and cycle-life prediction model for supercapacitors in alternative battery applications." *IEEE transactions on industrial electronics **59**(12): 4704-4712.*

VERIJENKO, B. & VERIJENKO, V. 2005. A new structural health monitoring system for composite laminates. *Composite structures*, 71, 315-319.

VON ALLMEN, L., et al. (2017). "Aircraft Strain WSN powered by Heat Storage Harvesting." IEEE transactions on industrial electronics.

WANG, Y., SHI, Z., HUANG, Y., MA, Y., WANG, C., CHEN, M. & CHEN, Y. 2009. Supercapacitor devices based on graphene materials. *The Journal of Physical Chemistry* C, 113, 13103-13107.

WEI, D. & NG, T. W. 2009. Application of novel room temperature ionic liquids in flexible supercapacitors. *Electrochemistry Communications*, 11, 1996-1999.

WINTER, M. & BRODD, R. J. 2004. What are batteries, fuel cells, and supercapacitors? *Chemical Reviews*, 104, 4245-4270.

YEDAVALLI, R. K. AND R. K. BELAPURKAR (2011). "Application of wireless sensor networks to aircraft control and health management systems." Journal of Control Theory and Applications **9**(1): 28-33.

ZHANG, S. S. (2007). "A review on the separators of liquid electrolyte Li-ion batteries." Journal of Power Sources **164**(1): 351-364.

Datasheet

Linear Technology Corporation, LTC3588

Linear Technology Corporation, LTC3109

Linear Technology Corporation, LTC3539

Linear Technology Corporation, LTC4425

Texas Instruments BQ25504

Maxwell-technical guide for pc-10 supercapacitors, http://www.maxwell.com/products/ultracapacitors/docs/applicationnote_maxwelltestprocedures.pdf

Anthony D'Amore, Ultracapacitor audio amplifier: US patent 20060238258 A1

MEC202, 1.7mAh 4V datasheet
http://www.infinitepowersolutions.com/images/stories/downloads/controlled_documents/DS1015.pdf. (2012)

Maxwell PC-10, 10F 2.75V datasheet
http://www.maxwell.com/products/ultracapacitors/docs/datasheet_pc10_1003996.pdf

Nesscap small supercapacitors2.5F, 5V datasheet
http://www.nesscap.com/product/edlc_small.jsp (2012)

LIR 2450
https://www.powerstream.com/p/Lir2450.pdf

LCC 120

http://www.farnell.com/datasheets/1912613.pdf?_ga=2.245496132.1511190695.1510560034-2067685152.1508674900

LCA 110

HTTP://www.ixysic.com/home/pdfs.nsf/www/LCA110.pdf/$file/LCA110.pdf

Marlow industries TEG

http://www.marlow.com/downloads/dl/file/id/257/product/113/tg12_6.pdf

Technical Guide: Maxwell-Technical guide, for PC-10 supercapacitors

http://www.maxwell.com/products/ultracapacitors/docs/applicationnote_maxwelltestprocedures.pdf